Fall 2016

Uncertainty quantification applied to the analysis and design of a hypersonic inflatable aerodynamic decelerator for spacecraft reentry

Andrew J. Brune

Department: Mechanical and Aerospace Engineering

UNCERTAINTY QUANTIFICATION APPLIED TO THE ANALYSIS AND DESIGN OF A HYPERSONIC INFLATABLE AERODYNAMIC DECELERATOR FOR SPACECRAFT REENTRY

by

ANDREW J. BRUNE

A DISSERTATION

Presented to the Graduate Faculty of the

MISSOURI UNIVERSITY OF SCIENCE AND TECHNOLOGY

In Partial Fulfillment of the Requirements for the Degree

DOCTOR OF PHILOSOPHY

in

AEROSPACE ENGINEERING

2016

Approved by:

Dr. Serhat Hosder, Advisor
Dr. David Riggins
Dr. Kakkattukuzhy Isaac
Dr. Xiaoping Du
Dr. Luca Maddalena

PUBLICATION DISSERTATION OPTION

This dissertation has been prepared in the style utilized by the Missouri University of Science & Technology in the form of three journal papers. The papers will be referred to by their Roman numerals. The papers are printed as per the university format; however, the content is according to their originally published state. The list of journal publications appended to this dissertation is given below:

Paper I on pages 10-53: Brune A. J., West, T. K., Hosder S., and Edquist, K. T., "Uncertainty Analysis of Mars Entry Flows over a Hypersonic Inflatable Aerodynamic Decelerator", *Journal of Spacecraft and Rockets*, Vol. 52, No. 3, pp. 776-788.

Paper II on pages 54-99: Brune A. J., Hosder S., and Edquist, K. T., "Uncertainty Analysis of Fluid-Structure Interaction of a Deformable Hypersonic Inflatable Aerodynamic Decelerator", *Journal of Spacecraft and Rockets*, Vol. 53, No. 4, pp. 654-668.

Paper III on pages 100-146: Brune A. J., Hosder S., Edquist, K. T., and Tobin, S. A., "Thermal Protection System Uncertainty of a Hypersonic Inflatable Aerodynamic Decelerator", accepted for publication in *Journal of Spacecraft and Rockets*, October 2016.

ABSTRACT

The primary objective of this research is to investigate the uncertainty in the multidisciplinary analysis of a Hypersonic Inflatable Aerodynamic Decelerator configuration for Mars entry, subject to uncertainty sources in the high-fidelity computational models and the operating conditions. Efficient uncertainty quantification methods based on stochastic expansions are applied to the analysis of the hypersonic flowfield, fluid-structure interaction, and flexible thermal protection system response of a deformable inflatable decelerator. Uncertainty analysis is first applied to the hypersonic flowfield simulations to quantify the uncertainty in the surface convective and radiative heat flux, pressure, and shear stress of a fixed inflatable decelerator, subject to uncertainties in the binary collision integrals of the transport properties, chemical kinetics, non-Boltzmann radiation modeling, and the freestream conditions. The uncertainty analysis for fluid-structure interaction modeling is conducted to quantify the uncertainty in the deflection and resulting surface heat flux, shear stress, and pressure of a deformable inflatable decelerator, subject to uncertainties in material structural properties, inflation pressure, and important flowfield uncertain variables identified in the initial study. The deflection uncertainty is shown to be primarily driven by the structural modeling uncertain variables and found to be insignificant in contributing to the resulting surface condition uncertainties. Uncertainty analysis is finally applied to the flexible thermal protection system bondline temperature for a ballistic Mars entry trajectory, subject to uncertainties in the material thermal properties and important flowfield variables from the initial study. The uncertainty in the bondline temperature is compared to its allowable temperature limit and shown to be primarily driven by the material thermal properties of the outer fabric and insulator layers, and the freestream density.

ACKNOWLEDGMENTS

This work was supported by a NASA Space Technology Research Fellowship under training grant no. NNX13AL58H with Dr. Serhat Hosder as the principal investigator and Karl Edquist from NASA Langley Research Center as the research collaborator. I would like to thank the fellowship program for granting me this opportunity to perform my research. I would also like to express my appreciation to my advisor, Dr. Serhat Hosder, for providing his assistance with the research experience under my tenure as a PhD candidate. I thank Karl Edquist for his mentorship throughout this fellowship award. He has not only been a mentor, but a true friend and collaborative partner. I would like to recognize Chris Johnston, Mike Lindell, and Steven Tobin from NASA Langley for their technical support, expertise, and contributions to this research.

I would like to also thank my committee members, Dr. David Riggins, Dr. Kakkattukuzhy Isaac, Dr. Xiaoping Du, and Dr. Luca Maddalena, for their time commitment to study this research work. Furthermore, I would also like to thank the Department of Mechanical and Aerospace Engineering for this educational opportunity.

I dedicate this dissertation to my grandparents, Leona and Theodore Mallinckrodt, and in-law grandparents, Mariel and Bob Grubbs, who were supportive in every way until their passing. I will always think back to their supportive conversations during my visits with them; they have helped me understand the true meaning of hard work - to enjoy what you do in life and provide for a family with faith, love, hope, and joy.

Finally, I must thank the true love my life, Dixie, and my family and friends for their love and support over the course of my education. Without them, I would not be where I am today.

TABLE OF CONTENTS

Page

PAPER

LIST OF ILLUSTRATIONS

LIST OF TABLES

SECTION

1. INTRODUCTION

In all aspects of life, uncertainty is upon all who will face new and emerging challenges. Much of the uncertainty is due to the present state of the unknown and sure knowledge of history. Overlooking or mistreating this uncertainty may increase risks and cause potential failures in the future. In the context of aerospace systems, the ability to model uncertainty is increasingly relied upon for simulating the unknown physics. Because there are many assumptions and approximations made in the numerical modeling of the physics (such as computational fluid dynamics, structural/thermal analysis), uncertainty must be introduced and accounted for in the analysis and design of the aerospace systems. Not only is the lack of knowledge of the underlying physics an important source of uncertainty, but also the inherent nature of the conditions or design parameters can be a significant factor in the uncertainty. As a result of these sources of uncertainty, the outcome or performance metrics of the physical system become uncertain. The rigorous quantification of uncertainty in aerospace simulations can be beneficial for reducing the risk and increasing the robustness and reliability of the aerospace system.

The papers included in this dissertation will focus on the uncertainty analysis of a Hypersonic Inflatable Aerodynamic Decelerator (or HIAD), which has been a recently developed spacecraft technology for potential future missions to Mars and other planetary bodies with increased payloads by an order of magnitude or larger (approximately 10-40 metric tons). First, a motivation of this technology and the challenges related to the design and analysis of this system are discussed. The objectives of this study are then presented,

followed by a description of the contributions of the work in multidisciplinary analysis of the HIAD. Lastly, a brief summary of the organization of the dissertation is given.

1.1. MOTIVATION

NASA continues to make strides to eventually send humans to Mars on missions which require increased landed masses beyond the capability of heritage rigid systems from the past. The Entry, Descent, and Landing (EDL) systems analysis studies [1, 2] conducted by the Exploration Feed Forward campaign [3] have provided potential game-changing technologies to invest in future EDL missions with increased payloads, and eventually humans to other planetary bodies, which include supersonic retro-propulsion, mid lift-to-drag vehicles, and inflatable technologies, such as a Hypersonic Inflatable Aerodynamic Decelerator (HIAD) [4] and the Adaptable, Deployable Entry Placement Technology (ADEPT), which can be stowed within the launch vehicle and deployed prior to atmospheric entry. Many advantages are anticipated with the HIAD technology (Figure 1.1) in the place of tradition rigid aeroshells, which include mass and space savings of the stowed configuration, high-altitude deceleration due to increased drag surface area at its deployed state, and longer entry times for pinpoint landing at selected sites on Mars. As the HIAD continues to mature in its design, the analysis tools must continue to improve in accuracy to obtain robustness and reliability standards.

In general, the HIAD is composed of two subsystems to protect the payload onboard during the EDL sequence: the inflatable structure and the flexible thermal protection system (TPS). The inflatable structure consists of a stack of toroids and rigid nose cap, which are held together by a network of straps. The TPS is a layup of materials, which include outer fabrics, insulators, and a gas barrier. The multidisciplinary nature of the analysis subject to influences of the thermal and mechanical loads from the external hypersonic

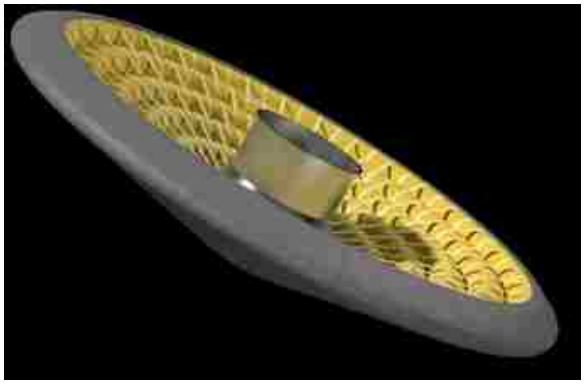

Figure 1.1. General HIAD configuration

flow poses significant challenges. High-fidelity tools, such as computational fluid dynamics, structural response of the inflatable structure, and thermal response of the TPS, are part of the analysis process for the design of the HIAD. Within each of these disciplines, inherent and model uncertainties play an important role and can significantly change the performance metrics evaluated by the physics-based models. The challenges that motivate the studies in this dissertation are addressed by each discipline in the following sections: (1) computational fluid dynamics (CFD), (2) fluid-structure interaction (FSI), and (3) flexible thermal protection system (F-TPS) response.

1.1.1. Computational Fluid Dynamics of the Hypersonic Flowfield. Hypersonic CFD prediction tools continue to be developed at NASA Langley Research Center to support a broad range of high-speed aerospace systems, including the HIAD. Hollis and Prabhu [5] reviewed and addressed simulation approaches and challenges for aerothermodynamic simulation capability of a Mars entry vehicle. A survey was conducted to identify sources of high-enthalpy, CO_2 aerothermodynamic data that could be used to help define computational uncertainties in the state-of-the-art flowfield prediction tools employed at NASA. Johnston et al. [6] presented work on a simulation approach for Mars entry radiative heat-

ing predictions from the shock layer and defined a new chemical kinetic rate model that was developed and provides good agreement with shock tube measurements.

Previous uncertainty quantification (UQ) studies of Mars entry flows have evaluated the uncertainty of the convective or radiative heat flux to the surface. Bose and Wright [7] studied uncertainty and sensitivities of laminar convective heating for Mars entry flows of a heatshield, shaped similar to the HIAD. Johnston et al. [6] performed an uncertainty assessment of the shock layer radiative heating to the surface of a HIAD baseline configuration. West and Hosder [8] applied a multi-step efficient UQ approach to the same problem to identify the top contributing uncertainties to shock-layer radiation subject to physical modeling parameters associated with the flowfield chemistry and the radiative heat transfer model. Further studies by West and Hosder [9] investigated a sparse-collocation NIPC technique to reduce the computational cost for UQ of the same problem. Although there has been much work in the aerothermodynamic uncertainty due to convection and radiation from an independent perspective, a comprehensive approach to understanding the uncertainty of the total heat flux (both convection and radiation), surface pressure, and shear and its respective sensitivities has not been addressed in the literature.

1.1.2. Fluid-Structure Interaction of the HIAD. Inflatable structures and systems are being developed at NASA Langley Research Center for application on HIADs to support future atmospheric entry missions. Ground testing has been shown to be essential to develop and demonstrate the performance of inflatable systems and components for a range of flight-relevant conditions. In addition, ground testing supports the development of physics-based codes to model the structural response of the HIAD for various flight trajectories.

Previous studies, such as Tanner [10], only performed FSI analysis of the static aeroelastic behavior of a potential decelerating technology for EDL, called a supersonic

inflatable aerodynamic decelerator. Similar efforts for a HIAD do not currently exist in the literature, although FSI work has been ongoing with subject matter experts at Langley. NASA's HIAD technology development project recently tested a full-scale 6m stacked torus inflatable article. Multiple aerodynamic wind tunnel and static pressure load tests [11, 12, 13] were conducted to characterize the inflatable structure response under relevant mission loading. FSI has been used to compare the predicted deflections from physics-based modeling to the experimental deflections observed during the tests. Accurate prediction of the structural response of the HIAD inflatable structure under relevant aerothermal and mechanical loads in a Mars entry environment presents a challenge in the presence of uncertainties associated with the complex high-fidelity models used.

1.1.3. Flexible Thermal Protection System of the HIAD. Flexible thermal protections systems are being developed at NASA Langley Research Center for application on HIADs to support future atmospheric entry missions. Ground testing has been shown to be essential in to develop and demonstrate the performance of new F-TPS for a range of flight-relevant conditions. In addition, ground testing supports the development of physics-based codes to model the F-TPS in-depth thermal response for various flight trajectories.

The HIAD technology development project at NASA has undergone extensive aerothermal arc jet testing of candidate flexible TPS materials and layups at stagnation conditions to evaluate thermal performance and provide boundary condition and in-depth measurement data for thermal model correlation and validation [14, 15, 16, 17]. Currently, arc-jet facilities are limited to extent of availability to provide flight-relevant aerothermal loads (e.g., heat flux and pressure, or enthalpy and shear) for flexible systems for durations sufficient to test over the total heat load. Therefore, development of accurate physics-based models is essential to predict the in-depth thermal response of F-TPS for all flight-relevant conditions that cannot be covered by ground testing support. Understanding the uncertainty sources

of the high-fidelity prediction tools for the in-depth thermal response is a key component to improve the physics modeling.

1.2. OBJECTIVES OF THE CURRENT STUDY

As part of the NASA Space Technology Research Fellowship program funding this project, each discipline was investigated under uncertainty on a yearly basis as an objective, shown in Figure 1.2. There are three objectives of this study, which are addressed by each of the journal papers included in this dissertation. A detailed literature review has been presented in each paper for more detailed background information to the reader. The objectives of this study are as follows:

1. Investigate the uncertainty in the high-fidelity CFD modeling of the hypersonic external flow over the HIAD, which includes sources of uncertainty in the freestream conditions, the binary collision transport models, and chemical kinetics models (Paper I).

2. Investigate the uncertainty in the high-fidelity FSI modeling of the structural response (deformations) of the HIAD and the resulting surface conditions, which includes important flowfield modeling uncertainties identified under objective 1 and the uncertainties in the inflation pressure of the toroids and component material properties of the structural model (Paper II).

3. Investigate the uncertainty in the high-fidelity modeling of the F-TPS thermal response of the HIAD, which includes important flowfield modeling uncertainties identified under objective 1 and the uncertainties in the insulator decomposition and material thermal properties (Paper III).

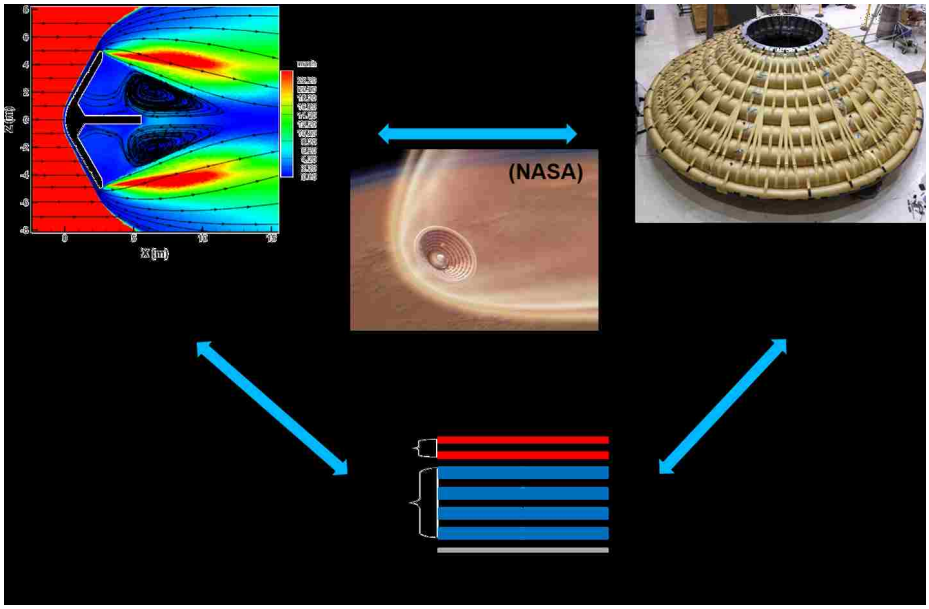

Figure 1.2. Multidisciplinary analysis of the HIAD under uncertainty

1.3. CONTRIBUTIONS OF THE CURRENT STUDY

Under each objective focusing on a discipline, the uncertainty in the performance metrics were analyzed, and the important contributors to the performance uncertainty were identified with sensitivity analysis. This study provides three primary contributions toward the design and analysis of the HIAD, which are addressed in each of the journal papers included in this dissertation.

1.3.1. Uncertainty Analysis of the Mars Entry Flow Modeling. Uncertainty analysis of the convective and radiative heating, surface pressure, and shear stress was performed for the high-fidelity flowfield modeling of the HIAD forebody at peak stagnation-point heating conditions of a ballistic Mars entry trajectory for both fully laminar and fully turbulent flows. A total of 65 uncertain variables, which included freestream conditions (i.e., velocity, density, and temperature) and physical modeling parameters associated with

flowfield chemistry, binary collision interactions, and radiative heat transfer, were considered for this analysis. This study used a stochastic expansion approach with sparse approximation [9] for efficient quantification of uncertainty in various output quantities of interest. This comprehensive overview of uncertainty analysis identified the important flowfield uncertainty sources that contribute to the uncertainty in the total heat flux, pressure, and shear stress, which were utilized in the uncertainty analysis of the fluid-structure interaction of a deformable HIAD and the F-TPS thermal response.

1.3.2. Uncertainty Analysis of the Fluid-Structure Interaction. Uncertainty analysis was performed for the high-fidelity, static FSI modeling of a deformable HIAD at peak heating conditions (assuming turbulent flow) of a ballistic and lifting Mars entry trajectory. This study used a stochastic expansion approach with sparse approximation [9] for efficient quantification of uncertainty in various output quantities of interest. A high-fidelity CFD solver was used to model thermochemical non-equilibrium flow and obtain the surface conditions and was loosely-coupled to a structural solver to obtain the static deflections of the HIAD. The uncertainty in the deflection and surface conditions of the HIAD was obtained subject to a number of epistemic and aleatory uncertainties in physical modeling parameters associated with the flowfield and inflatable structure. This study introduced the uncertainty sources in the structural modeling parameters of the HIAD and included the important flowfield uncertainty sources that were shown to significantly contribute to the wall pressure, shear stress, and heat flux uncertainties. This study identified the sensitivity of the deflection to the wall pressure, shear stress, and heat flux uncertainty.

1.3.3. Uncertainty Analysis of the Thermal Protection System. Uncertainty analysis was performed to investigate the uncertainty in the high-fidelity F-TPS thermal response predictions of the bondline temperature (near the gas barrier innermost layer) for a ballistic Mars entry trajectory. Efficient uncertainty quantification for various output quan-

tities of interest was obtained with the stochastic response methods by West et al. [9]. A high-fidelity CFD solver was used to model thermochemical non-equilibrium flow. The surface pressure and aerodynamic heating information were applied as boundary condition input for the F-TPS in-depth thermal response solver. Flowfield uncertainty sources that were shown to significantly contribute to the surface pressure and aerodynamic heating uncertainties were retained in this study. In addition, a number of uncertainty sources in the TPS thermal model were introduced which included material properties, thicknesses, and decomposition phenomena. A global non-linear sensitivity analysis was first performed to identify the important uncertain variables. Uncertainty quantification of the bondline temperature was then obtained in the reduced dimensions.

1.4. ORGANIZATION OF THE DISSERTATION

This dissertation is organized in the form of three journal publications. Uncertainty analysis of the hypersonic flowfield modeled with nonequilibrium thermochemistry for a HIAD using an efficient stochastic expansion approach (pages 11-51) has been published in the Journal of Spacecraft and Rockets in May 2015. Uncertainty analysis of the fluid-structure interaction of a HIAD using the same efficient uncertainty approach for obtaining deflection uncertainty and its effect on the surface condition uncertainty (i.e., heat flux, pressure, and shear stress) has been published in the Journal of Spacecraft and Rockets and is presented on pages 52-97. The uncertainty in the thermal protection system response for the HIAD is presented with an accepted paper for publication with Journal of Spacecraft and Rockets on pages 98-141. A detailed literature review relevant to the scope of this work is provided in each of the publications. The reader is advised to go through this information in the introduction section of each paper. In Section 2, general conclusions and possible future work for this research are presented.

PAPER

I. UNCERTAINTY ANALYSIS OF MARS ENTRY FLOWS OVER A HYPERSONIC INFLATABLE AERODYNAMIC DECELERATOR

Andrew J. Brune **Thomas K. West IV** **Serhat Hosder**

Missouri University of Science and Technology, Rolla, MO, 65409

Karl T. Edquist

NASA Langley Research Center, Hampton, Virginia 23681

ABSTRACT

A detailed uncertainty analysis for high-fidelity flowfield simulations over a fixed aeroshell of Hypersonic Inflatable Aerodynamic Decelerator (HIAD) scale for Mars entry is presented for fully laminar and turbulent flows at peak stagnation-point heating conditions. This study implements a sparse-collocation approach based on stochastic expansions for efficient and accurate uncertainty quantification under a large number of uncertainty sources in the computational model. The convective and radiative heating and shear stress uncertainties are computed over the HIAD surface and shown to vary due to a small fraction of 65 flowfield and radiation modeling parameters considered in the uncertainty analysis. The main contributors to the convective heating uncertainty near the stagnation point are the CO_2-CO_2, CO_2-O, and CO-O binary collision interactions, freestream density, and freestream velocity for both boundary layer flows. In laminar flow, exothermic recombination reactions are more important at the shoulder. The main contributors to radiative heating at the nose and flank were the CO_2 dissociation rate and CO heavy-particle excitation

rates while the freestream density showed importance towards the shoulder. The CO_2-CO_2 interaction and freestream velocity and density control the wall shear stress uncertainty.

NOMENCLATURE

CoV	Coefficient of Variation	T_e	Test Point Error
D	Statistical Variance	Ψ	Random Basis Function
n	Number of Random Dimensions	$\Omega^{1,1}$	Diffusion Collision Integral
N_s	Number of Samples	$\Omega^{2,2}$	Viscosity Collision Integral
N_t	Number of Terms in a Total-Order Polynomial Chaos Expansion	α	Deterministic Coefficient in the Polynomial Chaos Expansion
N_{TP}	Number of Test Points	α^*	Generic Uncertain Function
p	Order of Polynomial Expansion	δ	Truncation Error
S_e	Percent Absolute Error	ξ	Standard Input Random Variable
S_T	Total Sobol Index	μ_e	Mean Error

1. INTRODUCTION

Advanced robotic and human exploration missions to Mars require enhanced design capabilities for increased landed masses ($\sim$10 t) than current missions ($\sim$1 t). Architecture-level assessments from Entry, Descent, and Landing Systems Analysis [1, 2] (EDL-SA) and Exploration Feed-Forward [3] (EFF) studies have established that a Hypersonic Inflatable Aerodynamic Decelerator (HIAD), coupled with supersonic retropropulsion (SRP) and subsonic propulsive descent technologies, are enabling for safe and reliable landing at Mars. The inflatable technology has the capability to provide more options for planetary missions by allowing heavier and larger payloads and offering flexibility in landing site selection at higher altitudes. As HIAD technology continues to mature, engineers will need accurate toolsets in order to obtain robust and reliable designs.

One of the most dangerous segments of a mission to Mars is the hypersonic entry phase of the EDL sequence. During entry, the influence of a combination of convective and radiative heating on the aerothermal environment of future missions to Mars is potentially significant. Suggested HIAD concepts consist of a geometry shape resembling a 70-deg sphere cone with diameters as large as 20 m [4]. With HIAD geometries this large, radiative heating can potentially be a significant fraction of the convective heating. Proposed insulated thermal protection system (TPS) materials [2, 3] to protect the inflatable structure have relatively low heating limits ($\sim$60 W/cm^2), while flexible ablative TPS materials have higher heat flux limits (up to 115 W/cm^2 for SIRCA-flex and up to 450 W/cm^2 for PICA-flex). Accurate prediction of the radiative and convective heating of the HIAD surface with low-level heating requirements presents numerical simulation challenges.

With recent advancements in computational resources and development of efficient and accurate methodologies, computational fluid dynamics (CFD) has become the preferred approach in the analysis and design of planetary entry vehicles. One of the key issues with CFD of hypersonic reentry is the uncertainties in the complex physical models for non-equilibrium thermo-chemistry, turbulence, and radiative and convective heat transfer. Accurately quantifying these uncertainties is vital to design a robust and reliable HIAD configuration. Uncertainty analysis of such large-scale problems with a significant number of uncertain variables can also be challenging due to the computational demand of advanced deterministic models. Therefore, efficient uncertainty quantification (UQ) methods are more desirable over traditional sampling techniques, such as Monte Carlo, as they can provide accurate results with fewer deterministic model evaluations.

Previous work by Bettis and Hosder [5, 6] and Hosder et al. [7, 8] in the practical use of stochastic expansions based on nonintrusive polynomial chaos (NIPC) as a means of efficient UQ has been extensively investigated, which included studies involving the propagation of both aleatory (inherent) and model-form (epistemic) uncertainties. In general, the NIPC methods are based on a spectral representation of the uncertainty and can be significantly more efficient than traditional Monte Carlo simulations. Another advantage of the NIPC methods is that the deterministic model, such as a CFD code, is treated as a âĂIJblack-boxâĂİ as no intrusive changes to the model are needed to perform the UQ analysis. The theory behind the NIPC methodologies are both well-defined and well-understood [9, 10] making it a reliable method for UQ in complex aerospace simulations, which will be the basis of the UQ approach in the current study.

Previous UQ studies of Mars entry flows have addressed the challenges of present aerothermodynamic simulation capability. Hollis and Prabhu [11] reviewed simulation approaches for convective heating of a Mars entry vehicle. Bose and Wright [12] studied

uncertainty and sensitivities of laminar convective heating for Mars entry flows. Johnston et al. [4] presented work on a simulation approach for Mars entry radiative heating predictions and uncertainty assessment with a HIAD baseline model. West and Hosder [13] applied a multi-step UQ approach to the same problem for quantifying the top contributing uncertainties to shock-layer radiation. Further studies by West and Hosder [14] investigated a sparse-collocation NIPC technique to reduce the computational cost for UQ of the same problem, which focused only on the quantification of radiative heating uncertainty subject to physical modeling parameters associated with the flowfield chemistry and the radiative heat transfer model.

The objective of this paper is to perform a detailed uncertainty analysis for high-fidelity flowfield modeling over a baseline fixed aeroshell configuration of HIAD scale at peak stagnation-point heating conditions, obtained from a ballistic (axisymmetric) reentry dynamics model [15], for both fully laminar and fully turbulent flows. This study will utilize a sparse-collocation stochastic expansion approach, which was introduced by the authors in their previous work [14], for efficient quantification of uncertainty in various outputs. Specifically, this work will present uncertainty results for convective heating, radiative heating, and shear stress distributions on the HIAD surface which are subject to a large number of epistemic and aleatory uncertainties in freestream conditions (i.e., velocity, density, and temperature) and physical modeling parameters associated with flowfield chemistry, binary collision interactions, and radiative heat transfer. It is also important to note that the detailed uncertainty analysis presented in this work for the fixed HIAD aeroshell geometry will identify the important flowfield uncertainty sources that contribute to the output uncertainty, which will be utilized in future uncertainty analysis of a flexible (deformable) HIAD.

The following section describes the UQ methodology used in the current study. The high-fidelity deterministic CFD model, baseline geometry and freestream conditions, stochastic problem, and uncertainty assessments for fully laminar and fully turbulent flows for the HIAD reentry flow problem are presented in Section 3. Concluding remarks are given in Section 4.

2. UNCERTAINTY QUANTIFICATION METHODOLOGY

In recent studies [5, 6, 8, 16, 17], the polynomial chaos method has been used as a means of UQ over traditional methods, such as Monte Carlo, for computational efficiency. Polynomial chaos is a surrogate modeling technique based on the spectral representation of the uncertainty. An important aspect of spectral representation of uncertainty is that a response value or random function α^* (such as surface heat flux or shear stress at a particular surface location) can be approximated as a series with each term decomposed into separable deterministic and stochastic components, as shown in Eq. (2.1).

$$\alpha^*(\mathbf{x},\xi) \approx \sum_{i=0}^{P} \alpha_i(\mathbf{x})\Psi_i(\xi) \tag{2.1}$$

Here, α_i is the deterministic component and Ψ_i are the random variable basis functions corresponding to the ith mode. α^* is assumed to be a function of the deterministic variable vector $\mathbf{x}$ and the n-dimensional standard random variable vector ξ. By definition, this series is infinite; however, it can be truncated with a discrete sum over a number of output modes [10]. To form a complete basis or a total order expansion, the truncated series can be represented with N_t number of terms, which will depend on the polynomial chaos expansion (PCE) of order p and the number of random dimensions or variables, n:

$$N_t = P + 1 = \frac{(n+p)!}{n!p!} \tag{2.2}$$

Further details on polynomial chaos theory are given by Walters and Huyse [9] as well as Eldred [10].

To determine the expansion coefficients, α_i, without any modifications to the deterministic code (i.e., CFD code), several non-intrusive polynomial chaos (NIPC) methods have been developed. Of these, the point-collocation NIPC method has been used extensively in many aerospace simulations and CFD problems [6, 8, 17, 13]. The point-collocation method starts with replacing a stochastic response or random function with its PCE using Eq. (2.1). Then, N_t vectors are chosen in random space, and the deterministic code is then evaluated at these points to represent the left hand side of Eq. (2.1). Following this, a linear system of N_t equations can be formulated and solved for the spectral modes of the random variables, shown in Eq. (2.3).

$$\begin{pmatrix} \Psi_0(\xi_0) & \Psi_1(\xi_0) & \cdots & \Psi_P(\xi_0) \\ \Psi_0(\xi_1) & \Psi_1(\xi_1) & \cdots & \Psi_P(\xi_1) \\ \vdots & \vdots & \ddots & \vdots \\ \Psi_0(\xi_P) & \Psi_1(\xi_P) & \cdots & \Psi_P(\xi_P) \end{pmatrix} \begin{pmatrix} \alpha_0 \\ \alpha_1 \\ \vdots \\ \alpha_P \end{pmatrix} = \begin{pmatrix} \alpha^*(\mathbf{x}, \xi_0) \\ \alpha^*(\mathbf{x}, \xi_1) \\ \vdots \\ \alpha^*(\mathbf{x}, \xi_P) \end{pmatrix} \tag{2.3}$$

Note that for this linear system, N_t is the minimum number of deterministic samples (N_s) required to obtain a solution of the determined system (i.e., the coefficient vector). If more samples are available (N_s>N_t) and linearly independent, the system is considered overdetermined and can be solved using a least squares approach. Polynomial chaos techniques, however, suffer from a "curse of dimensionality" in the sense that the number of deterministic model evaluations required to create an accurate surrogate model grows exponentially with the number of random dimensions. For many large-scale, complex problems, such as those found in modeling hypersonic reentry flows, it may be impractical to obtain the minimum required number of deterministic model samples. The most desirable approach is to obtain an accurate surrogate model with as few deterministic samples as possible to limit the computational cost.

If a case which has the number of deterministic model samples less than the minimum required for the solution to the determined system (N_s<N_t) is considered, then a system of linear equations is obtained that has fewer linearly independent equations than unknowns and possesses an infinite number of solutions. In a recent study by West and Hosder [14], it was shown that a small fraction of the PCE coefficients carry significant weight in the surrogate model. With the assumption that the expansion coefficient vector is sparse, the linear system can be regularized allowing for a well-posed solution. West and Hosder [14] presented a solution technique used by Asif [18] with the L_1-minimization problem using convex relaxation, where the objective is to seek a solution to the linear system with the fewest number of non-zero coefficients.

$$\min \left\| \alpha \right\|_1 \text{ subject to } \left\| \Psi\alpha - \alpha^* \right\|_2 \leq \delta \tag{2.4}$$

Here, δ is the error associated with the truncation of the series in Eq. (2.1). For the problems considered in this study, δ is assumed to be equal to zero, as it can be shown that the solution to Eq. (2.4) is unique with this assumption. In the above formulation, the dimensions of Ψ are N_s x N_t and the vector α^* is of length N_s. The vector α is of length N_t. Doostan and Owhadi [19] discuss, in great detail, the theory and formulation of the above method.

The optimization problem in Eq. (2.4) is commonly referred to as Basis Pursuit Denoising (BPDN) [19, 20, 18]. In the current study, the least absolute shrinkage and selection operator (LASSO) homotopy optimization routine [18] was selected to find the optimal solution of Eq. (2.4) and is shown to be efficient due to its convergence being weakly dependent on the dimension of the problem [20].

With this optimization and sparse-collocation approach, a procedure is followed for determining an acceptable sample size to achieve convergence and accuracy of the poly-

nomial chaos expansion. The first step in this process is to generate an initial sample set of the uncertain variables. The size of this initial sample set, generated using Latin Hypercube sampling, is taken as the size, N_t, given by Eq. (2.2) as this would be the minimum number of samples required to obtain a total order expansion. Note that generating large sample sets of the uncertain parameters is not computationally expensive compared to the cost of evaluating the deterministic model. A small subset of the initial sample structure is selected, and the deterministic model is evaluated at these points. Then, a first set of PCE coefficients can be obtained using the minimization routine in Eq. (2.4). This process is then repeated by iteratively adding more samples to the solution procedure (i.e., addition of new subsets of the full sample structure) until the convergence of the expansion coefficients is achieved. Each subset of the full sample structure added at each iteration is restricted to not contain any repeated sample vectors from the previous iterations so that new information is provided in recovering a new solution at each iteration.

Convergence of the expansion coefficients is checked at each iteration. West and Hosder [14] presents two methods used to track the convergence of the expansion coefficients and the resulting polynomial expansion. The first method uses variance-based global sensitivity analysis measures, Sobol indices [21, 22], to measure the convergence of the expansion coefficient vector as the Sobol indices highly depend on the coefficients of the PCE. Further detail on this dependence and the derivation of total Sobol indices is given by West and Hosder [14] The total Sobol index for each uncertain variable j ($S_{T,j}$) provides a sensitivity measure in terms of its total contribution to the total variance of the output quantity of interest. To monitor the convergence of the total Sobol indices with the addition of more samples at each iteration, an absolute error, $S_{e_{i,j}}$ can be defined for the j^{th} total Sobol index at iteration i using Eq. (2.5).

$$S_{e_{i,j}} = \left\| S_{T,i,j} - S_{T,i-1,j} \right\| \tag{2.5}$$

Note that measuring the convergence based on this absolute error puts emphasis on the variables that contribute to the output uncertainty more significantly. The errors of each total Sobol index, at each iteration, can then be averaged giving a single value for monitoring, which is shown in Eq. (2.6).

$$\mu_{e,i} = \frac{1}{n} \sum_{j=1}^{n} S_{e_{i,j}} \tag{2.6}$$

Plotting this average error at each iteration would then illustrate the convergence of the PCE coefficients. The objective is to seek out nearly asymptotic convergence, as zero error would likely not be achievable simply due to the randomness of the samples added at each iteration and any numerical noise that may occur during the analysis of complex models.

The second approach to measure the convergence of the PCE coefficients is to compare response values from the PCE to a set of sample points obtained from the design space, separate from the surrogate model training samples. Errors are measured between response values from the polynomial approximation and the actual response at the test sample locations distributed throughout the design space using a Latin Hypercube sample structure. This has the advantage of improving the coverage of the design space when a small sample set is used. The magnitude of improvement of this error will depend on the convergence (i.e., the accuracy of the model at the current iteration) and the number of test points used. The error between the points, $T_{e,i}$, is estimated by the empirical error defined by Eq. (2.7) [23]:

$$T_{e,i} = \frac{1}{N_{TP}} \sum_{j=1}^{N_{TP}} (F_{surr.}(\mathbf{x_j}) - F_{actual}(\mathbf{x_j}))^2 \tag{2.7}$$

Here, N_{TP} is the number of test points, $F_{surr.}$ is the response value from the PCE surrogate model, and F_{actual} is the actual test point value from the design space. The error between the surrogate and the deterministic model, at each test point, is an indication of the local accuracy of the surrogate model. Maximizing the number of test points will provide better coverage in the design space and would provide the best indication of the accuracy of the surrogate. This comes at the cost of additional evaluations of the deterministic model.

In this work, the stochastic problem contains both aleatory and epistemic types of uncertainty. For mixed uncertainty for which contributions of both types of uncertainty are considered, a procedure known as second-order probability [10] is used to propagate the mixed uncertainty through the stochastic model. Details on the uncertainty classification and second-order probability approach can be found in previous work which have been used to validate the UQ approaches and methodologies presented in this section [15, 13, 14].

3. UNCERTAINTY ANALYSIS OF HIGH-FIDELITY REENTRY FLOWFIELD MODELING OVER A HIAD

This section presents a detailed uncertainty assessment of the aerothermodynamic heating and shear stresses due to uncertainty in flowfield and radiation modeling parameters. An overview of the computational fluid dynamics (CFD) model is presented in Section 3.1. The HIAD configuration (similar to Figure 3.1) and baseline conditions used in this problem are described in Section 3.2. The stochastic model for implementing the sparse-collocation UQ approach is given in Section 3.3. Aerotherodynamic heating and shear stress uncertainties are assessed for fully laminar and turbulent boundary layer flows in Sections 3.4 and 3.5, respectively. Convergence and accuracy measures, using the methodology in Section 2, are also provided in Section 3.4 to evaluate the number of required samples for an accurate surrogate model used in the uncertainty analysis.

3.1. DESCRIPTION OF THE DETERMINISTIC MODEL

For this problem, the Langley Aerothermodynamic Upwind Relaxation Algorithm (LAURA) Navier-Stokes solver [24] from NASA Langley Research Center is used for the high-fidelity numerical solution of the hypersonic flowfield over a HIAD. LAURA is a three-dimensional, structured code, which uses a finite-volume, shock-capturing approach to solve high-speed flows with frozen, equilibrium, or nonequilibrium thermochemistry. The algorithm incorporates point-implicit or line-implicit relaxation schemes to efficiently obtain solutions on advanced computers and perform expensive computations for problems on a complex scale. An important feature of the code is the ability to perform one-dimensional grid adaptation to resolve high gradients in the boundary layer and

Figure 3.1. Representative depiction of a HIAD

across a shock wave. The flowfield at steady-state conditions were modeled using a two-temperature, thermochemical nonequilibrium model for a Mars 16-species composition: CO_2, CO, N_2, O_2, NO, C, N, O, CN, C_2, C^+, O^+, CO^+, O_2^+, NO^+, and e^-. The two-temperature thermochemical nonequilibrium model, applied in this work, is presented by Park et al. [25], with chemical rate modifications based on recent comparisons with shock tube radiation measurements. The chemical rates, with inclusion of these modifications, are presented in Table A.1 of the Appendix. This analysis focuses on two boundary layer conditions: fully laminar and fully turbulent flows. The Cebeci-Smith algebraic turbulence model [26] was used to model the turbulent boundary layer.

For this study, the HARA nonequilibirum radiation code is also implemented with a tangent-slab radiation transport approach and coupled with the LAURA Navier-Stokes solver. The details regarding the radiation modeling approach and parameters used in this study are given by Johnston et al. [4]. In particular, a complete list of the molecular band systems treated and parameters used for their modeling are provided in Table A.2 of the Appendix for convenience.

3.2. BASELINE GEOMETRY AND FREE-STREAM CONDITIONS

To model a fixed aeroshell of HIAD scale at the stagnation-point heating condition [15], a 70-deg sphere cone with a nose radius of 4 m, shoulder radius of 0.4 m, and a maximum diameter of 16 m is considered for this analysis. The geometry is representative of a Viking heritage shape, similar to Mars Science Laboratory (MSL) and other rigid aeroshell geometries, and the size of the selected configuration has been studied by NASA personnel in the EFF study [3]. Figure 3.2 presents the grid-independent baseline computational mesh for this HIAD geometry with size of 128x48 normal-by-streamwise grid cells, which has also been used in previous work by West and Hosder [14] and Johnston et al. [4] with slightly different geometry scale. Grid clustering near the shock is essential to fully capture significant radiation emitted from the strong nonequilibrium region [4].

The baseline freestream conditions were set at the peak stagnation-point heating (convective and radiative heating) location of the reentry trajectory corresponding to a freestream velocity of 6.25 km/s, density of 1.0e-4 kg/m^3, and temperature of 150 K [15]. For all cases, the angle of attack was set to zero to simplify the flowfield modeling to axisymmetric and simulate the ballistic entry condition [15] of the baseline trajectory. The freestream composition for all cases is assumed to be 96% CO_2 and 4% N_2 by mole. The wall of the HIAD was modeled as super-catalytic (species composition set to freestream values) with a constant wall temperature of 1500 K to simulate worst-case heating conditions, strongly emphasizing that little information is available on the wall material for modeling wall catalysis. The choice of wall catalytic model and wall temperature conditions can, however, have a strong effect on the CFD parameters that influence convective heating rate. The results presented in this subsection are referred to as the baseline (best-estimate) case and will be referenced for the remaining uncertainty discussions in Sections 3.4 and 3.5.

The radiative flux spectrum at the wall is presented in Figure 3.3 for the baseline peak stagnation-point heating condition, which includes the contributions of the molecular bands. At this condition, significant contribution from the CO 4th Positive band in the spectrum region between 120 and 220 nm is seen. Previous published work [4, 27] has shown that the CO 4th Positive band is the strongest emitter at peak radiative heating with slightly higher velocities. Emission of the CO 4th Positive band originates in the thin nonequilibrium region of the shock layer. This is shown in Figure 3.4, which presents the volumetric radiance along the stagnation line resulting from the strongest molecular band emitters, along with the radiative flux profile. Clearly, the CO 4th Positive molecular band is the strongest emitter by a significant margin with CN Violet band as the second largest contributor to the radiative flux. This is in agreement with a study by Johnston et al. [4], which showed that the CO 4th Positive and CN Violet molecular bands were the largest contributors to the radiative flux to the vehicle surface. Notice the increased differences in the cumulative radiative flux in Figure 3.3 due to the CO 4th Positive band system for the spectral range of 120 and 230 nm. The sharp increase in the radiative flux can also be observed due to the spike in CO 4th Positive emission in Figure 3.4 at the shock standoff distance of 18 cm. Capturing the spike in the nonequilibrium region and the smoothness of the shock standoff distance is therefore important in accurate modeling of the radiative flux. Figures 3.5-3.6 illustrate the representation of these aspects for the baseline case.

Baseline fully laminar and fully turbulent aeroheating and pressure solutions are presented in Figure 3.7. A result of note is that the radiative heating is a significant fraction ($\sim$20%) of the convective heating, especially in the flank region. The radiative heating for both laminar and turbulent flows are remarkably similar. As mentioned before, the increase in radiative flux is due to the strong emission in the nonequilibrium region. Furthermore, it has been shown by Johnston et al. [28] that turbulence typically has negligible effect on the

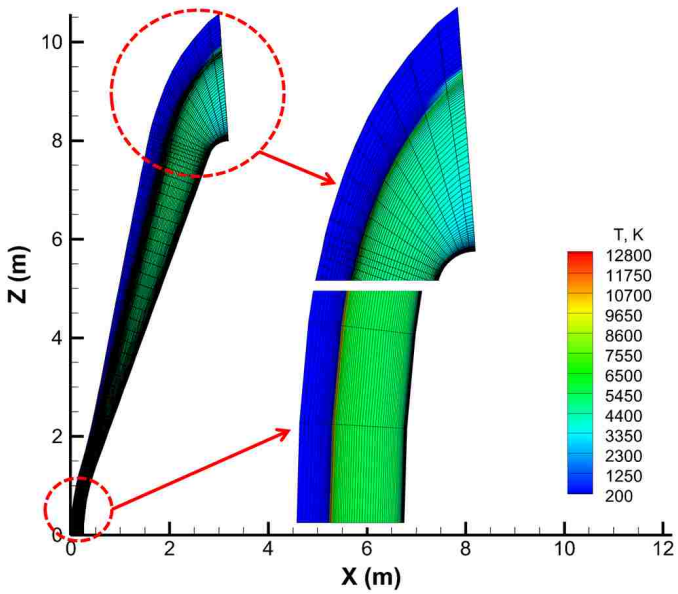

Figure 3.2. Baseline computational grid with shock layer temperature contours

radiative heating for cases with little or no ablation. It is also worth mentioning that there is a strong similarity in the pressures for both boundary layer flows as shown in Brune et al. [15]. As a result, laminar and turbulent boundary layers only display significant differences in the convective heat flux and shear stress, as expected. For fully turbulent flows, the Cebeci-Smith (CS) model predicts augmented heating values by a factor of two. To verify these results, Figure 3.8 compares the heating predictions for Cebeci-Smith [26] and Spallart-Almaras (SA) turbulence models. The augmented heating levels for both turbulence models agree well in the flank region of the HIAD, with Cebeci-Smith slightly over-predicting the higher-fidelity Spallart-Almaras model in the nose region. Further agreement is seen between the Cebeci-Smith and Spallart-Almaras shear stress solutions.

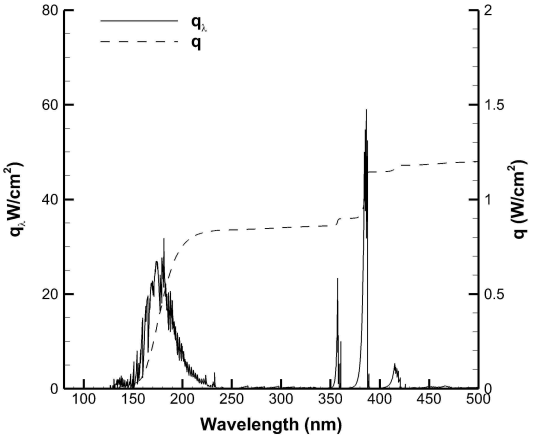

Figure 3.3. Radiative flux spectrum (monochromatic and cumulative) for the peak stag. point heating (baseline) case

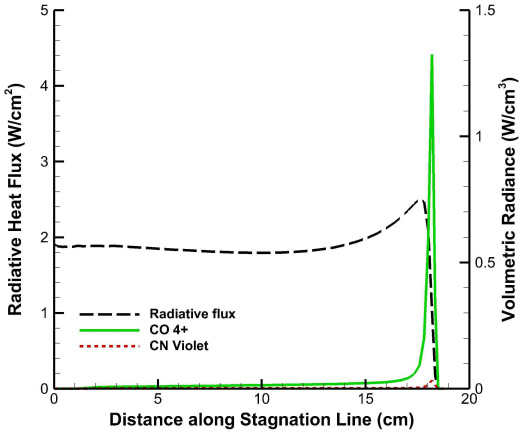

Figure 3.4. Volumetric radiance and radiative Flux along the stagnation line for the baseline case

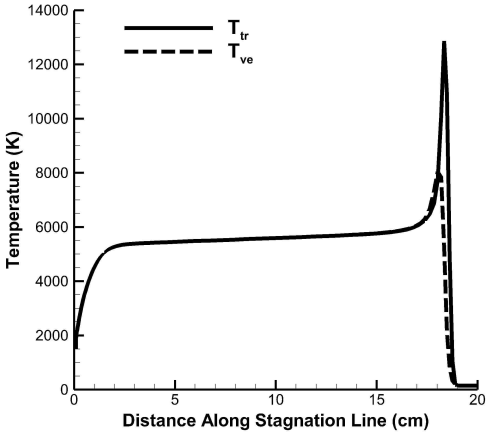

Figure 3.5. Stagnation line temperatures for the baseline case

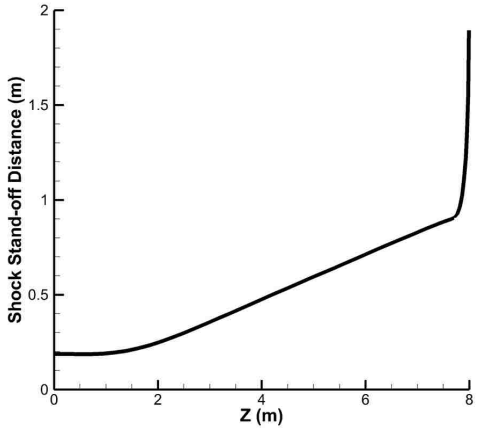

Figure 3.6. Shock standoff distance for the baseline case

3.3. DESCRIPTION OF THE STOCHASTIC PROBLEM

For this study, 65 uncertain input parameters related to numerical modeling of a HIAD, described in Section 3.1, were considered in the UQ analysis. Table 3.1 summarizes the various uncertainty source categories, number of uncertain parameters included in each

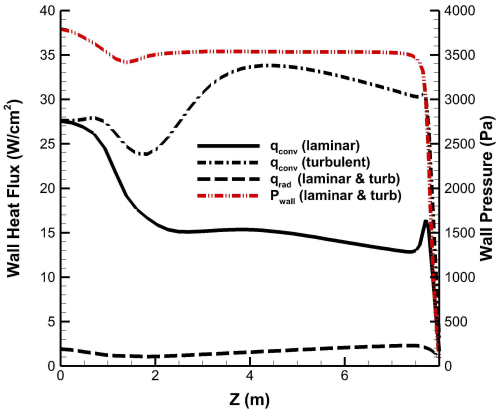

Figure 3.7. Baseline convective and radiative heating and wall pressure

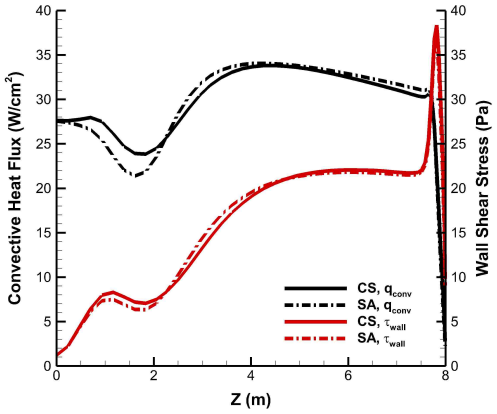

Figure 3.8. Comparison of the Cebeci-Smith and Spallart-Almaras convective heating and wall shear stress

category, and assigned uncertainty ranges with indicated references. Uncertainties were considered in the flowfield and radiation modeling parameters and freestream conditions. Uncertainty in the flowfield modeling parameters for combined convective and radiative heat fluxes are primarily due the uncertainty in the chemical kinetic rates and binary collision integrals. Chemical kinetic rates can be difficult to accurately measure and model, making them potentially significant sources of uncertainty. Likewise, binary collision integrals have also been shown to be important modeling parameters in high temperature flows to accurately model the transport quantities that govern convective heat transfer to the HIAD surface. A study by Wright et al. [29] indicates that there can be as much as 30% uncertainty associated with binary collision integrals. Published work by Bose and Wright [12], Palmer et al. [30], and Bose et al. [31] have treated binary collision integrals as uncertain. The catalytic wall recombination efficiency is another source of uncertainty that strongly affects the convective heat transfer. However, this physical modeling parameter is not considered in this study due to insufficient information on the wall materials

Table 3.1. Summary of uncertain parameters for the HIAD CFD simulations

Category	No. of Uncertain Parameters	Classification	Uncertainty	Ref.
Chemical Kinetic Reaction Rates	20	Epistemic	Table A.1	[4]
Binary Collision Integrals	36	Epistemic	±30%	[12]
Heavy-Particle Impact Excitation Rates	4	Epistemic	Table A.3	[4]
Electron Impact Excitation Rates	1	Epistemic	Table A.3	[4]
Molecular Band Oscillator Strengths	1	Epistemic	Table A.3	[4]
Freestream Velocity (m/s)	1	Normal	6254, 0.5% CoV	[15]
Freestream Density (kg/m^3)	1	Uniform	[8.64e-5, 1.48e-4]	[15]
Freestream Temperature (K)	1	Uniform	[146, 154]	[15]
TOTAL	**65**			

to expertly assign uncertainty. Instead, this study will focus on the worst-case condition with a super-catalytic wall assumption. The choice of wall catalytic model can, however, have a strong effect on the CFD parameters that influence convective heating rate. Towards the non-catalytic end of the spectrum, the convective heating rate would be significantly reduced. In addition to these uncertainties, wall temperature can also have an effect on the heating. For this problem, a constant wall temperature is considered.

The uncertainty in the binary collision integrals and chemical kinetic rates were modeled as epistemic uncertainties due to lack of knowledge in the CFD physical model. A total of 20 chemical reaction rates for 20 reactions were treated as uncertain. A complete list of the chemical reactions, baseline Arrhenius rate parameters, and input uncertainties of the Arrhenius coefficients are provided in Table A.1 of the Appendix. Furthermore, the collision integrals for only the neutral species interactions were taken to be uncertain. With eight neutral species, there are 36 binary collision integrals that must be treated as uncertain. A complete list of the neutral species interactions, considered for this analysis, are given in Table A.4 in the Appendix. The uncertainty in the binary collision integrals were implemented through the use of a single parameter, A, similar to the studies by Bettis et al. [32] and Bose et al. [12]:

$$\Omega^{1,1} = A f_1(T) \tag{3.1}$$

$$\Omega^{2,2} = A f_2(T) \tag{3.2}$$

The functions f_1 and f_2 are expressions with temperature dependence, and the form of the curve fits are presented by Gupta et al. [33] The A parameter (multiplier) in Eq. 3.1-3.2 were treated as the uncertain parameter with lower bound of 0.7 and upper bound of 1.3, which corresponds to a $\pm 30\%$ uncertainty [12]. In Eq. 3.1, $\Omega^{1,1}$ is used to calculate the diffusion coefficients. Likewise, in Eq. 3.2, $\Omega^{2,2}$ is used to calculate the viscosity coefficients. Furthermore, as noted by Wright et al. [29], both of these collision integrals are used to compute the thermal conductivity.

The second category of uncertainty, which particularly affects the radiative heating, is the radiation modeling parameters. West et al. [13] presents the top contributing radiation modeling parameters that contribute 95% uncertainty in the shock-layer radiation emitted to the HIAD surface at Mars. The uncertainty in the molecular band processes (i.e., oscillator strengths) represent the spectrum modeling uncertainty. The uncertainty in the non-Boltzmann modeling can also be a significant source of uncertainty, which consists of excitation rates for both heavy-particle and electron impacts. Table A3 in the Appendix provides the reactions, baseline Arrhenius rate parameters, and input uncertainties for the top contributing spectrum and non-Boltzmann modeling parameters, respectively. Details regarding uncertainties in radiation modeling parameters, and specifics thereof, are left to the discussion in the published works of West et al. [13] and Johnston et al. [4, 27] Since there is a lack of knowledge and sufficient information regarding these quantities, the uncertainty due to the radiation modeling parameters in Table A3 of the Appendix were treated as epistemic uncertainties.

The final source of uncertainty is the inherent variations of the freestream conditions that potentially affect the heat transfer to the surface of the HIAD vehicle. The total enthalpy of the flow has a strong effect on the heat transfer to the surface. The mechanical loadings (pressures) behind the shock wave, and hence the wall, are also strongly dependent on the freestream dynamic pressure condition for which the HIAD passes along its trajectory. For this analysis, the freestream velocity, density, temperature can be described through probabilistic measures due to its inherent nature. Note that the freestream temperature will have little effect on convective and radiative heating rates compared to the freestream velocity and density. The freestream velocity input to the CFD simulation is treated as an aleatory uncertain variable with a normal distribution with a mean of 6254 m/s and a coefficient of variance (CoV) of 0.5%. The CoV assignment was based on the uncertainty information in the velocity, corresponding to maximum stagnation-point heating condition [15]. Note that the uncertainty range for the freestream velocity is conservative to insure that the uncertainties are included for both the reentry dynamics model and the inherent nature of the freestream velocity. The freestream density and temperature were also treated as aleatory uncertain variables with uniform distributions and were allowed to vary based on the uncertainty information in the altitude for peak stagnation-point heating obtained in the reentry dynamics problem [15]. The freestream density and temperature intervals of [8.64e-5,1.48e-4] kg/m^3 and [146,154] K, respectively, were used in this analysis.

3.4. UNCERTAINTY ASSESSMENT FOR THE FULLY LAMINAR FLOW CASE

An overview of the model problem and the baseline results, obtained from the deterministic CFD model, were examined in the previous two subsections. The uncertainties of the aerodynamic heating and shear stress distributions for the fully laminar flow cases

at peak stagnation-point heating are studied in this subsection, which were obtained with the sparse-collocation approach outlined in Section 2. Only one of 65 uncertain parameters (freestream density) contributed to the wall pressure uncertainty for both boundary layer flows and is not presented here. The wall pressure uncertainty results can be found in Brune et al. [15] Convergence and accuracy measures of the surrogate model are presented for the aerodynamic heating results since the convergence and accuracy levels reflect those observed for all output responses in both boundary flow cases.

The uncertainty analysis was conducted with the procedures outlined in Section 2. The polynomial chaos expansions require a minimum of 2211 CFD evaluations for a second order expansion with 65 uncertain parameters (Eq. 2.2). As a result, an initial sample set was generated with 2211 samples using Latin hypercube sampling. A subset of 10 samples were randomly selected at the first iteration, and 10 samples were added to the analysis at each iteration until convergence. Figure 3.9(a) presents the convergence of the mean total Sobol error, normalized by the maximum, for the convective and radiative heat fluxes at selected surface locations on the HIAD. Significant variation of the error is shown for small sample sizes. As the sample size increases, the error drops rapidly to errors approximately or less than 0.05 with 300 samples. Comparing to the 2211 samples required for a second order expansion, the sparse-collocation approach is able to recover convergence and accuracy of polynomial chaos expansion coefficients using at most 400 CFD evaluations (80% reduction).

Accuracy and convergence can be checked by comparing test point values of the CFD model with the response values obtained with the surrogate model at the same sample locations. Figure 3.9(b) shows the convergence and accuracy with 100 test point values using Eq. 2.7. Similar convergence trends were observed for the test point error compared to Sobol error with a value of at most 0.1 error. The accuracy level shown for this method

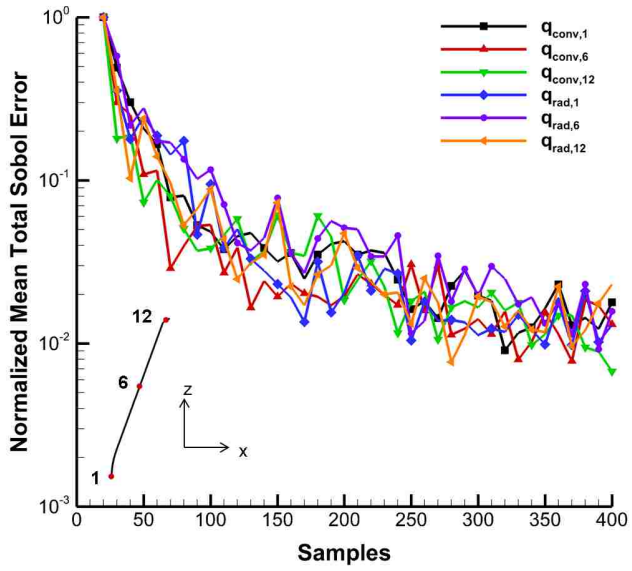

(a) Sobol Error

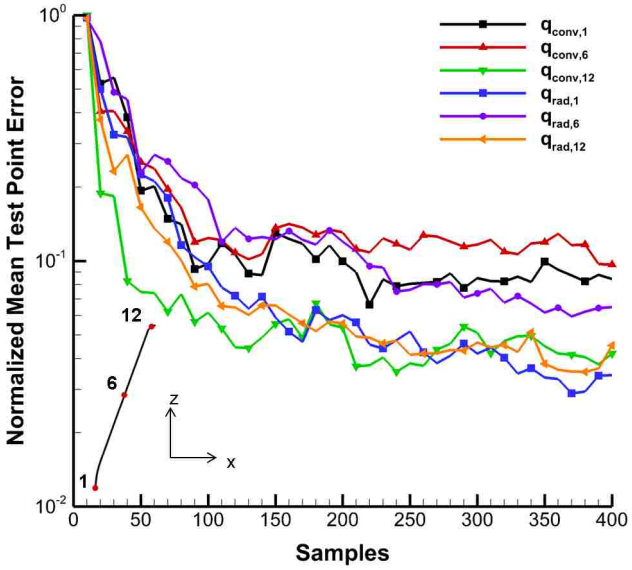

(b) Test Point Error

Figure 3.9. Surrogate model convergence for convective and radiative Heating at selected HIAD surface locations (laminar flow case)

is generally higher than that for the Sobol error approach. Numerical noise in the CFD may influence the errors observed in the test point comparison.

Further investigation of the p-boxes are shown in Figure 3.10 at selected sample sizes. For the HIAD locations chosen to cover the entire surface range, convergence of the upper and lower cumulative density function (CDF) distributions is achieved at approximately 300-400 samples, similar to the convergence trends for the Sobol and test point error approaches. Convergence and accuracy of the Sobol and test point errors and the CDF p-box plots were shown to be remarkably similar for radiative heating and shear stresses for both boundary layer flows.

Figure 3.11 presents the 95% confidence interval and baseline distributions for convective, radiative, and total heating along the HIAD surface at 13 selected locations between the stagnation point and the shoulder region. The upper and lower heating limits were obtained by using the lower and upper CDF bounds from the constructed p-boxes (Figure 3.10). As can be seen from Figure 3.11(a), radiative heating uncertainty is a significant fraction of the total heating uncertainty. Radiative heating significance is especially noticeable if the upper limit (97.5% probability distribution line) of the radiative heating values are considered, which are approximately 20-40% of the total heating for this peak stagnation-point heating trajectory point. If non-catalytic wall conditions were considered, radiative heating values may likely be comparable to the non-catalytic convective heating. Radiative heating also shows a slightly skewed behavior in the limits with respect to the baseline case. One would suspect that this behavior may originate from strongly contributing radiation modeling parameters.

Tables 3.2-3.3 present the fractional contributions of the uncertain parameters to the overall uncertainty of the convective and radiative heating based on the converged Sobol index values. Table 3.2 includes several uncertain parameters which contribute 1% or more to the overall uncertainty of the convective heat flux, and as suggested, the contributions depend on HIAD surface location. The CO_2-CO_2, CO_2-O, and CO-O interactions have

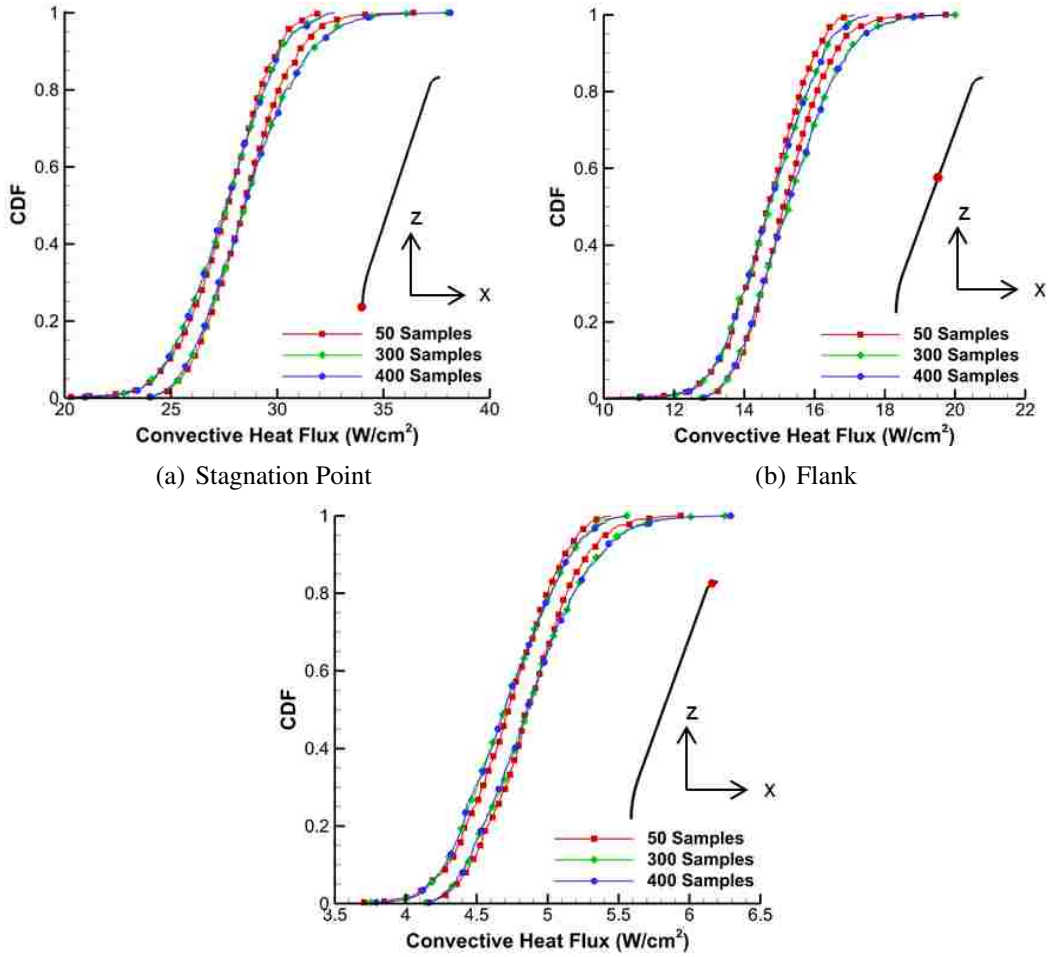

(a) Stagnation Point

(b) Flank

(c) Shoulder

Figure 3.10. P-Box convergence for convective heat flux at selected locations along the HIAD surface (laminar flow case)

significant contribution throughout the entire HIAD surface. Bose et al. [12] shows that convective heat flux in a laminar environment is very sensitive to the CO_2-CO_2, CO_2-O, and CO-O collision partners and agree with the conclusions of this study. At the stagnation point and flank region, the freestream density and velocity appear to be important factors in the overall uncertainty of convective heating, consistent with the engineering correlation presented in Brune et al. [15] Downstream, towards the shoulder, an interesting result is ob-

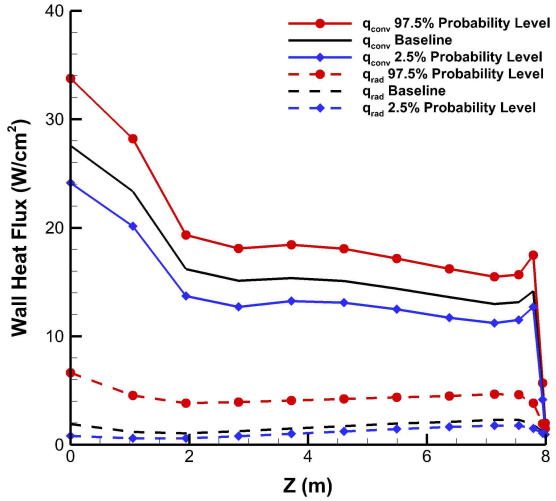

(a) Convective and Radiative Heating

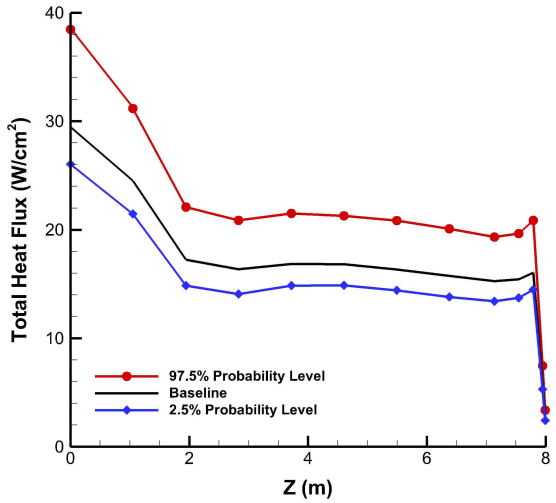

(b) Combined (total) Heating

Figure 3.11. Uncertainty (95% confidence intervals) in the heat flux distributions along the HIAD surface (laminar flow case)

served. The significance of the freestream quantities diminishes, and the reactions of CO_2 + M $\leftrightarrow$ CO + O + M and CO_2 + O $\leftrightarrow$ O_2 + CO become important in the convective heat

Table 3.2. Uncertainty contributions to convective heating at selected HIAD surface locations (laminar flow case)

Uncertainty Sources	Stagnation Point	Flank	Shoulder
$CO_2 + M \leftrightarrow CO + O + M$	<0.1%	0.4%	6.1%
$CO_2 + O \leftrightarrow O_2 + CO$	1.5%	3.3%	8.1%
CO_2-CO_2	7.7%	10.8%	9.9%
CO_2-O	49.3%	61.7%	63.1%
CO-O	5.3%	5.2%	6.6%
ρ_{inf}	16.5%	0.2%	0.3%
V_{inf}	19.4%	16.2%	1.4%

Table 3.3. Uncertainty contributions to radiative heating at selected HIAD surface locations (laminar flow case)

Uncertainty Sources	Stagnation Point	Flank	Shoulder
$CO_2 + M \leftrightarrow CO + O + M$	20.9%	29.3%	16.9%
$O2 + M \leftrightarrow 2O + M$	1.7%	0.7%	0.6%
$CO_2 + O \leftrightarrow O_2 + CO$	0.7%	1.9%	2.0%
$CN(A^2\Pi^+) + M \leftrightarrow CN(B^2\Sigma^+) + M$	0.8%	2.6%	4.9%
$CO(X^1\Sigma^+) + M \leftrightarrow CO(A^1\Pi) + M$	53.8%	31.0%	7.3%
$CO(a'^3\Sigma^+) + M \leftrightarrow CO(d^3\Delta) + M$	3.6%	2.0%	0.2%
$CO(e^3\Sigma^-) + M \leftrightarrow CO(A^1\Pi) + M$	6.7%	3.9%	0.5%
ρ_{inf}	3.6%	15.2%	59.8%
V_{inf}	5.2%	9.9%	5.6%

transfer to the wall. For super-catalytic wall conditions, the two reactions in the boundary layer act as a reverse, exothermic recombination process. The chemical kinetic rates dramatically affect how the boundary layer is heated, and therefore, results in changes in the thermal conduction to the wall. As mentioned before, these results for convective heating are dependent on the super-catalytic wall assumption.

As shown in Table 3.3, nine uncertainty sources contribute 1% or more to the overall uncertainty in the radiative heating. Similar to convective heating, the contributions are dependent on the HIAD surface location. As discussed in Section III.B, the CO 4th Positive molecular band was shown to be the strongest emitting band in the thin nonequilibrium region. As expected, the reactions indicated in Table 3.3 involve the process of CO production. As a result, reaction rates can have a significant effect on the existence of

CO within the shock layer. Since there is presence of the CO molecule in the nonequilibrium region, the non-Boltzmann rate involving the radiating states of the CO 4th Positive band system (lower and upper state) shows the largest significance compared to the remaining non-Boltzmann rates for the considered heavy-particle and electron impact excitations, which is consistent with the findings of the sensitivity analysis by Johnston et al. [4]. Significant variations in the freestream density explain the dominating effect of this uncertain parameter towards the shoulder as the effect of CO 4th Positive radiating states diminishes. Finally, the freestream velocity has a small effect on the uncertainty of the radiative flux due to a small uncertainty range, and hence, small changes to the temperature spike in the strong nonequilibrium region.

For the same 13 points on the HIAD, response surfaces were constructed for the shear stress at the wall. The 97.5% and 2.5% probability shear stress limits are presented with the baseline shear stress distributions in Figure 3.12. Uncertainty in the wall shear stress is due to primarily the CO_2-CO_2 interaction and the freestream velocity near the stagnation point. The CO_2-CO_2 interaction affects the viscosity coefficient component of the shear stress dependence, and the freestream velocity contributes to the velocity gradient at the wall. Towards the shoulder, significant change in the density explains the increased effect of this uncertain parameter while the effect of the freestream velocity diminishes and a slight reduction in the importance of CO_2-CO_2 interaction is observed.

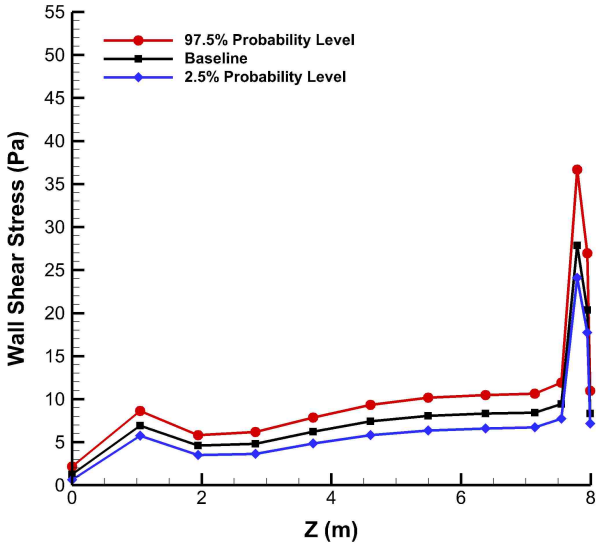

Figure 3.12. Uncertainty (95% confidence intervals) in the shear stress along the HIAD surface (laminar flow case)

Table 3.4. Uncertainty contributions to shear stress at selected HIAD surface locations (laminar flow case)

Uncertainty Sources	Stag. Pt.	Flank	Shoulder
CO_2-CO_2	76.6%	72.3%	62.7%
ρ_{inf}	6.2%	14.3%	35.7%
V_{inf}	14.5%	11.5%	0.1%

3.5. UNCERTAINTY ASSESSMENT FOR THE FULLY TURBULENT FLOW CASE

For the fully turbulent flow case, the aerodynamic heating and shear stress uncertainty results show remarkable differences compared to the laminar case and are, therefore, presented here. Figure 3.13(a) shows that for the turbulent flow case, the convective heating can be significantly larger than the laminar flow case especially in the flank region, where

the heating rate is increased by a factor of two. The radiative heating upper and lower limits in Figure 3.13(a) show remarkable similarity to those observed in the laminar case. This can be explained by the suggested note by Johnston [28] that radiative heating levels are similar between laminar and turbulent boundary layer flows without ablation. The radiation still contributes to the total heating, especially between the stagnation point and the start of the flank region. The total heating limits and baseline values in Figure 3.13(b) show a resembling behavior to that of the convective heating, primarily due to the superposition of the radiative and convective heating rates.

Table 3.5 provides the top contributing uncertain parameters that affect the uncertainty in the convective heating and radiative heating for the turbulent flow case. For convective heating, the CO_2-CO_2, CO_2-O, and CO-O collision partners show similar relative significance compared to the laminar case. However, the freestream quantities (density and velocity) become more prominent in turbulent flow as they affect the Reynolds number based on momentum thickness. Similar to the laminar case, the velocity contribution diminishes downstream of the nose region while the freestream density becomes more important. For the radiative heating in Table 3.6, the fractional contributions of the top contributing uncertain parameters are remarkably similar to those observed in the laminar case with subtle differences in the fractional values.

Figure 3.14 presents the 95% confidence upper and lower limits, compared with the baseline level, for the turbulent shear stress along the HIAD surface. Nearly double the values and magnified uncertainty bounds with respect to the laminar case are observed in the flank and shoulder region. This magnified uncertainty in these regions are primarily due to the freestream density and CO_2-CO_2 interaction, shown in Table 3.7. The contributions to the turbulent shear stress uncertainty are similar to the laminar case with the freestream density carrying more weight due the its dependence on the Reynolds number.

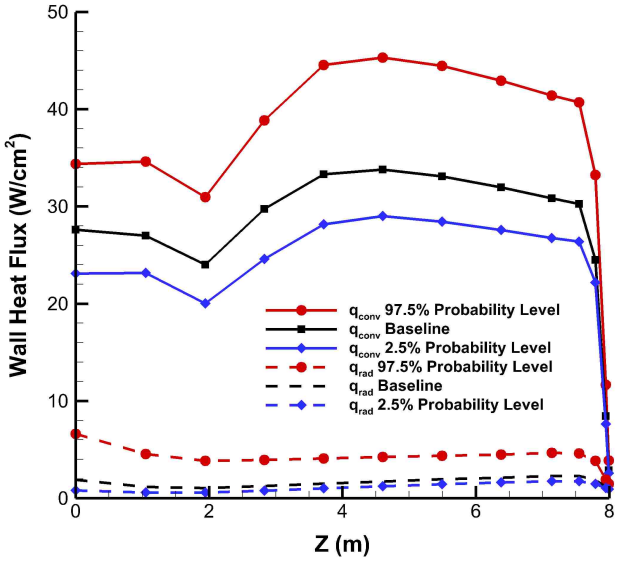

(a) Convective and Radiative Heating

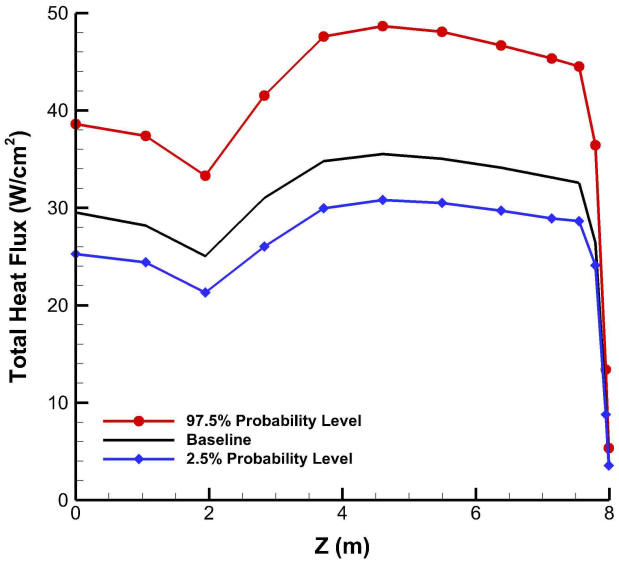

(b) Combined (total) Heating

Figure 3.13. Uncertainty (95% confidence intervals) in the heat flux distributions along the HIAD surface (turbulent flow case)

Table 3.5. Uncertainty contributions to convective heating at selected HIAD surface locations (turbulent flow case)

Uncertainty Sources	Stagnation Point	Flank	Shoulder
CO_2-CO_2	6.1%	2.0%	4.2%
CO_2-O	41.9%	15.1%	10.0%
CO-O	4.2%	0.1%	0.1%
ρ_{inf}	20.0%	79.2%	84.8%
V_{inf}	27.2%	3.5%	0.7%

Table 3.6. Uncertainty contributions to radiative heating at selected HIAD surface locations (turbulent flow case)

Uncertainty Sources	Stagnation Point	Flank	Shoulder
$CO_2 + M \leftrightarrow CO + O + M$	20.9%	29.8%	16.7%
$O2 + M \leftrightarrow 2O + M$	1.6%	0.8%	0.4%
$CO_2 + O \leftrightarrow O_2 + CO$	0.7%	1.9%	2.1%
$CN(A^2\Pi^+) + M \leftrightarrow CN(B^2\Sigma^+) + M$	0.8%	2.6%	4.8%
$CO(X^1\Sigma^+) + M \leftrightarrow CO(A^1\Pi) + M$	53.4%	30.6%	7.4%
$CO(a'^3\Sigma^+) + M \leftrightarrow CO(d^3\Delta) + M$	3.6%	2.0%	0.2%
$CO(e^3\Sigma^-) + M \leftrightarrow CO(A^1\Pi) + M$	6.5%	3.4%	0.7%
ρ_{inf}	3.5%	15.4%	59.9%
V_{inf}	5.5%	9.8%	5.4%

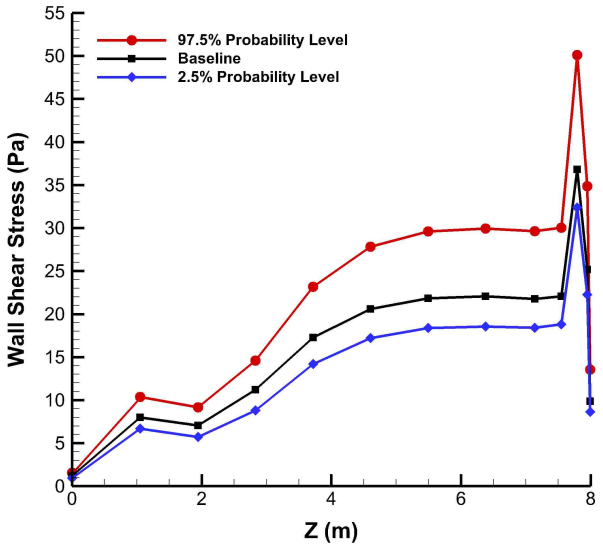

Figure 3.14. Uncertainty (95% confidence intervals) in the shear stress along the HIAD surface (turbulent flow case)

Table 3.7. Uncertainty contributions to shear stress at selected HIAD surface locations (turbulent flow case)

Uncertainty Sources	Stag. Pt.	Flank	Shoulder
CO_2-CO_2	76.6%	72.3%	62.7%
ρ_{inf}	6.2%	14.3%	35.7%
V_{inf}	14.5%	11.5%	0.1%

4. CONCLUDING REMARKS

A detailed uncertainty analysis with an efficient sparse-collocation stochastic expansion approach was presented for the high-fidelity numerical modeling of hypersonic flow over a HIAD during Mars entry for both fully laminar and fully turbulent flows. In particular, a fixed aeroshell of HIAD scale is considered for quantification of uncertainty in the shock-layer flowfield at peak stagnation-point heating conditions. Uncertainty results were presented for convective heating, radiative heating, and shear stress distributions on the HIAD surface which were subject to a large number of epistemic and aleatory uncertainties in freestream conditions (i.e., velocity density, and temperature) and physical modeling parameters associated with flowfield chemistry, binary collision interactions, and radiative heat transfer.

Only a small fraction of the 65 uncertain parameters revealed significant contribution to the uncertainty in the aerodynamic heating and shear stresses at the wall. Boundary layer type (laminar and turbulent) affected only the convective heating and shear stresses, as the radiative heating and wall pressures showed remarkable similarities for both boundary layer flows. The CO_2-CO_2, CO_2-O, and CO-O interactions strongly affected the convective heating uncertainty for both laminar and turbulent flows. The freestream quantities (velocity and velocity) were also significant, particularly in the stagnation point and flank regions for laminar flow. However, near the shoulder, the exothermic recombination reactions showed importance over the freestream quantities. For turbulent flows, this behavior was not observed. The Reynolds number variation affected the turbulent heating augmentation in the flank region, which explains the high dependence of convective heating on the freestream density and velocity. The non-Boltzmann rate involving the radiating states

of the CO 4th Positive band was the main contributor to the radiative flux at the nose and flank regions. The reactions that involved production of the CO also consistently showed significant contributions to the uncertainty of the radiative flux for both boundary layer flows. These observations are primarily due to the strong emission of the CO 4th Positive molecular band system in the nonequilibrium region of the shock layer. The emergence of freestream density as the main contributor was seen towards the shoulder, which is likely due to the uncertainty range considered and the diminishing effect of CO heavy-particle excitation rates. For the shear stress uncertainties, the CO_2-CO_2, freestream density, and freestream velocity were shown to be important for both boundary layer flows with significant increase in effect by the freestream density for turbulent boundary layers.

Overall, the detailed and efficient uncertainty analysis presented in this work over a fixed HIAD aeroshell identified the important flowfield uncertainty sources that contribute to the uncertainty in aerodynamic heating and wall shear and will form the basis for future uncertainty analysis of a flexible (deformable) HIAD.

ACKNOWLEDGMENTS

This work was supported by a NASA Space Technology Research Fellowship under training project grant no. NNX13AL58H (Serhat Hosder, principal investigator and Karl Edquist, research collaborator). The authors would like to thank Christopher O. Johnston for his expert opinion and discussions of the shock-layer radiation modeling for the current project.

BIBLIOGRAPHY

[1] Zang, T. A., Dwyer-Ciancolo, A. M., Kinney, D. J., R.Howard, A., Chen, G. T., Ivanov, M. C., Sostaric, R. R., and Westhelle, M. C., "Overview of the NASA Entry, Descent, and Landing Systems Analysis Studies for Large Robotic-class Missions, AIAA 2010-8649," *AIAA SPACE 2010 Conference and Exhibition*, Anaheim, CA, Aug. 2010.

[2] Dwyer-Ciancolo, A. M., Davis, J. L., Shidner, J. D., and Powell, R. W., "Entry, Descent, and Landing Systems Analysis: Exploration Class Simulation Overview and Results," *AIAA/AAS Astrodynamics Specialist Conference*, Toronto, Ontario Canada, Aug. 2010.

[3] Dwyer-Ciancolo, A. M., Davis, J. L., Engelund, W. C., Komar, D. R., Queen, E. M., Samareh, J. A., Way, D. W., and Zang, T. A., "Entry, Descent, and Landing Systems Analysis Study: Phase 2 Report on Exploration Feed-Forward Systems," Tech. rep., NASA/TM-217055, Feb. 2011.

[4] Johnson, C. O., Hollis, B. R., and Sutton, K., "Shock Layer Radiation Modeling and Uncertainty for Mars Entry," *43rd AIAA Thermophysics Conference*, New Orleans, LA, 2012.

[5] Hosder, S. and Bettis, B., "Uncertainty and Sensitivity Analysis for Reentry Flows with Inherent and Model-Form Uncertainties," *Journal of Spacecraft and Rockets*, Vol. 49, No. 2, 2012, pp. 193–206.

[6] Bettis, B., Hosder, S., and Winter, T., "Efficient Uncertainty Quantification in Multidisciplinary Analysis of a Reusable Launch Vehicle, AIAA 2011-2393," *17th AIAA International Space Planes and Hypersonic Systems and Technologies Conference*, San Francisco, CA, 2011.

[7] Hosder, S., Walters, R. W., and Balch, M., "Efficient Sampling for Non-Intrusive Polynomial Chaos Applications with Multiple Uncertain Input Variables, AIAA 2007-1939," *48th AIAA/ASME/ASCE/AHS/ASC Structures, Structural Dynamics, and Materials Conference*, Honolulu, HI, April 2007.

[8] Hosder, S., Walters, R. W., and Balch, M., "Point-Collocation Nonintrusive Polynomial Chaos Method for Stochastic Computational Fluid Dynamics," *AIAA Journal*, Vol. 48, No. 12, 2010, pp. 2721–2730.

[9] Walters, R. W. and Huyse, L., "Uncertainty Analysis for Fluid Mechanics with Applications," Tech. rep., ICASE 2002-1, NASA/CR-2002-211449, NASA Langley Research Center, Hampton, VA, 2002.

[10] Eldred, M. S., "Recent Advances in Non-Intrusive Polynomial Chaos and Stochastic Collocation Methods for Uncertainty Analysis and Design, AIAA 2009-2274," 50^{th} *AIAA/ASME/ASCE/AHS/ASC Structures*, Palm Springs, CA, May 2009.

[11] Hollis, B. R. and Prabhu, D. K., "Assessment of Laminar, Convective Aeroheating Prediction Uncertainties for Mars Entry Vehicles," *AIAA Journal of Spacecraft and Rockets*, Vol. 50, No. 1, 2013, pp. 56–68.

[12] Bose, D. and Wright, M., "Uncertainty Analysis of Laminar Aeroheating Predictions for Mars Entries," *AIAA/AAS Astrodynamics Specialist Conference*, Toronto, Ontario Canada, Aug. 2010.

[13] West IV, T. K., Hosder, S., and Johnston, C. O., "A Multi-Step Uncertainty Quantification Approach Applied to Hypersonic Reentry Flows, AIAA 2011-2524," 51^{st} *AIAA Aerospace Sciences Meeting*, Grapevine, TX, Jan. 2013.

[14] West IV, T. K., Hosder, S., and Johnston, C. O., "Uncertainty Quantification of Hypersonic Reentry Flows using Sparse Sample and Stochastic Expansions," *16th AIAA Non-Deterministic Approaches Conference*, National Harbor, MD, Jan. 2014.

[15] Brune, A. J., West, T., Hosder, S., and Edquist, K. T., "Uncertainty Analysis of Mars Entry Flows over Hypersonic Inflatable Aerodynamic Decelerators, AIAA 2014-2672," *11th AIAA/ASME Joint Thermophysics and Heat Transfer Conference*, Atlanta, GA, 2014.

[16] Witteveen, J. A. S. and Bijl, H., "Efficient Quantification of the Effect of Uncertainties in AdvectionâĂŞDiffusion Problems Using Polynomial Chaos," *Numerical Heat Transfer*, Vol. 53, No. 5, 2008, pp. 437–465.

[17] Han, D. and Hosder, S., "Inherent and Model-Form Uncertainty Analysis for CFD Simulation of Synthetic Jet Actuators, AIAA 2012-0082," 48^{th} *AIAA Aerospace Sciences Meeting*, Nashville, TN, Jan. 2012.

[18] Asif, M. S. and Romberg, J., "Fast and Accurate Algorithms for Re-Weighted l1-Norm Minimization," *IEEE Transactions on Signal Processing*, Vol. 61, No. 23, 2013, pp. 4905–4916.

[19] Doostan, A. and Owhadi, H., "A non-adapted sparse approximation of PDEs with stochastic inputs," *Journal of Computational Physics*, Vol. 230, No. 8, 2011, pp. 3015–3034.

[20] Yang, A., Ganesh, A., Sastry, S., and Ma, Y., "Fast L1-Minimization Algorithms and An Application in Robust Face Recognition: A Review," Tech. rep., Tech. Rep. UCB/EECS-2010-13, Feb. 2010.

[21] Sudret, B., "Global sensitivity analysis using polynomial chaos expansion," *Reliability Engineering and System Safety*, Vol. 93, No. 7, 2008, pp. 964–979.

[22] Crestaux, T., Maitre, O. L., and Martinez, J.-M., "Polynomial chaos expansion for sensitivity analysis," *Reliability Engineering and System Safety*, 2009.

[23] Blatman, G. and Sudret, B., "Adaptive sparse polynomial chaos expansion based on least angle regression," *Journal of Computational Physics*, Vol. 230, No. 6, 2011, pp. 2345–2367.

[24] Mazaheri, A., Gnoffo, P. A., Johnston, C. O., and Kleb, B., "LAURA Users Manual: 5.5-65135," Tech. rep., NASA/TM-2011-217800, Feb. 2012.

[25] Park, C., Howe, J. T., Jaffe, R. L., and Candler, G. V., "Review of Chemical-Kinetic Problems for Future NASA Missions, II: Mars Entries," *Thermophysics and Heat Transfer*, Vol. 8, No. 1, 1994, pp. 9–23.

[26] Smith, A. M. and Cebeci, T., "Numerical solution of the turbulent boundary layer equations," Tech. rep., Tech. Rep. Douglas Aircraft Division DAC-33735, 1967.

[27] Johnson, C. O., Gnoffo, P. A., and Sutton, K., "Influence of Ablation on Radiative Heating for Earth Entry," *Journal of Spacecraft and Rockets*, Vol. 46, No. 3, 2009, pp. 481–491.

[28] Johnston, C. O., Mazaheri, A., Gnoffo, P., Kleb, B., and Bose, D., "Radiative Heating Uncertainty for Hyperbolic Earth Entry, Part 1: Flight Simulation Modeling and Uncertainty," *Journal of Spacecraft and Rockets*, Vol. 50, No. 1, 2013, pp. 19–38.

[29] Wright, M. J., Hwang, H. H., and Schwenke, D. W., "Recommended Collision Integrals for Transport Property Computations Part II: Mars and Venus Entries," *AIAA Journal*, Vol. 45, No. 1, 2007, pp. 281–288.

[30] Palmer, G., "Uncertainty Analysis of CEV LEO and Lunar Return Entries, AIAA 2007-4253," *39th AIAA Thermophysics Conference*, Miami, FL, June 2007.

[31] Bose, D., Wright, M., and Gökçen, T., "Uncertainty and Sensitivity Analysis of Thermochemical Modeling for Titan Atmospheric Entry, AIAA 2004-2455," *37th AIAA Thermophysics Conference*, Portland, OR, April 2004.

[32] Bettis, B. and Hosder, S., "Uncertainty Quantification in Hypersonic Reentry Flows Due to Aleatory and Epistemic Uncertainties, AIAA 2011-252," *49th AIAA Aerospace Sciences Meeting including New Horizons Forum and Aerospace Exposition*, Orlando, FL, Jan. 2011.

[33] Gupta, R. N., Yos, J. M., Thompson, R. A., and Lee, K. P., "A Review of Reaction Rates and Thermodynamic and Transport Properties for an 11-Species Air Model for Chemical and Thermal Nonequilibrium Calculations to 30000 K," Tech. rep., NASA/RP-1232, Aug. 1990.

APPENDIX

The following appendix gives tables of the uncertain flowfield and radiation modeling parameters for the HIAD reentry flow model problem. The uncertain parameters are ordered and indicated by number for the purposes of uncertainty assessment of aerodynamic heating, wall pressure and shear stress distributions in Section IV. Note that the parameters of Tables A.1 and A.3 are those of an Arrhenius form. The equations for each of these three tables are provided in Eq. (A.1), (A.2), and (A.3). Additional molecular band spectrum information is given in Table A.2 for reference to the discussion on the total heat flux spectrum in Section 3.2. For further description of these uncertain parameters, the justification of their uncertainty ranges, and detailed discussion of the radiation modeling parameters, see Johnston et al. [4]. Detailed description on the modeling of the binary collision integrals for the partners listed in Table A.4 is given by Wright et al. [29].

Table A.1. Uncertain flowfield chemical kinetics

#	Reaction	$A_{f,i}$	$n_{f,i}$	$D_{f,i}$	$T_{f,i}$	Ref.	Uncertainty
1	$CO_2 + M \leftrightarrow CO + O + M$	6.9e+21	-1.50	6.328e+4	T_a	N, C, O	-1, +0 om
		1.4e+22	-1.50	6.328e+4	T_a	others	-1, +0 om
2	$CO + M \leftrightarrow C + O + M$	1.2e+21	-1.00	1.29e+5	T_a	All	-75%, +50%
3	$C_2 + M \leftrightarrow 2C + M$	4.5e+18	-1.00	7.15e+4	T_a	All	-1, +1 om
4	$CN + M \leftrightarrow C + N + M$	6.0e+15	-0.4	7.10e+4	T_a	All	-1, +1 om
5	$N_2 + M \leftrightarrow 2N + M$	3.0e+22	-1.60	1.132e+5	T_a	N, C, O	-1, +1 om
		6.0e+3	2.6	1.132e+5	T_{ve}	e^-	-1, +1 om
		7.0e+21	-1.60	1.132e+5	T_a	others	-1, +1 om
6	$NO + M \leftrightarrow N + O + M$	1.1e+17	0.00	7.55e+4	T_a	N, C, O, NO, CO_2	-1, +1 om
		2.0e+15	0.00	7.55e+4	T_a	others	-1, +1 om
7	$O2 + M \leftrightarrow 2O + M$	1.0e+22	-1.50	5.936e+04	T_a	N, C, O	-50%, +50%
		2.0e+21	-1.50	5.936e+04	T_a	others	-50%, +50%
8	$CO_2 + O \leftrightarrow O_2 + CO$	2.71e+14	0.0	3.38e+4	T_{tr}		-1, +1 om
9	$CO + C \leftrightarrow C_2 + O$	2.4e+17	-1.00	5.80e+4	T_{tr}		-1, +1 om
10	$CO + N \leftrightarrow CN + O$	1.0e+15	0.00	3.86e+4	T_{tr}		-1, +1 om
11	$CO + NO \leftrightarrow CO_2 + N$	3.0e+6	0.88	1.33e+4	T_{tr}		-1, +1 om
12	$CO + O \leftrightarrow O_2 + C$	3.9e+13	-0.18	6.92e+4	T_{tr}		-0, +1 om
13	$C_2 + N_2 \leftrightarrow CN + CN$	1.5e+13	0.0	2.1e+4	T_{tr}		-1, +1 om
14	$CN + C \leftrightarrow C_2 + N$	3.0e+14	0.00	1.81e+4	T_{tr}		-1, +1 om
15	$CN + O \leftrightarrow NO + C$	1.6e+12	0.10	1.46e+4	T_{tr}		-1, +1 om
16	$N + CO \leftrightarrow NO + C$	1.1e+14	0.07	5.35e+4	T_{tr}		-1, +1 om
17	$N_2 + C \leftrightarrow CN + N$	1.1e+14	-0.11	2.32e+4	T_{tr}		-50%, +50%
18	$N_2 + CO \leftrightarrow CN + NO$	1.2e+16	-1.23	7.70e+4	T_{tr}		-1, +1 om
19	$N_2 + O \leftrightarrow NO + N$	6.0e+13	0.1	3.80e+4	T_{tr}		-50%, +50%
20	$O_2 + N \leftrightarrow NO + O$	2.49e+9	1.18	4.01e+3	T_{tr}		-1, +1 om

$$k_{f,i} = A_{f,i} T_{f,i}^{n_{f,i}} exp(-D_{f,i}/T_{f,i}) \tag{A.1}$$

Table A.2. Molecular band processes

Molecule	Upper State – Lower State	Band Name	λ Range (nm)
CO	$A^1\Pi - X^1\Sigma^+$	4th Positive	120 – 280
CO	$b^3\Sigma^+ - a^3\Pi_r$	3rd Positive	250 – 450
CO	$d^3\Delta_i - a^3\Pi_r$	Triplet	320 – 2500
CO	$a'^3\Sigma^+ - a^3\Pi_r$	Asundi	370 – 2500
CO	$B^1\Sigma^+ - A^1\Pi$	Angstrom	400 – 700
CO	$X^1\Sigma^+ - X^1\Sigma^+$	Infrared	1200 – 7000
CN	$A^2\Pi_i - X^2\Sigma^+$	Red	400 – 2800
CN	$B^2\Sigma^+ - X^2\Sigma^+$	Violet	300 – 550
C_2	$d^3\Pi_g - a^3\Pi_u$	Swan	390 – 1000
C_2	$b^3\Sigma_g^- - a^3\Pi_u$	Ballik-Ramsay	500 – 3000
C_2	$A^1\Pi_u - X^1\Sigma_g^+$	Phillips	350 – 1200
C_2	$D^1\Sigma_u^+ - X^1\Sigma_g^+$	Mulliken	200 – 250
C_2	$C^1\Pi_g - A^1\Pi_u$	Des.-D'Azam.	280 – 700
C_2	$e^3\Pi_g - a^3\Pi_u$	Fox-Herzberg	200 – 500
CO_2	$X^1\Sigma_g^+ - X^1\Sigma_g^+$	Infrared	1700 – 25000
CO_2	$A^1B_2 - X^1\Sigma_g^+$	UV	190 – 320

Table A.3. Uncertain heavy-particle and electron impact excitation rates (cm^3/s) for non-Boltzmann modeling and uncertain molecular band processes for spectrum modeling

#	Reaction/Process	$A_{hp}\|A_{el}$	$n_{hp}\|n_{el}$	$E_{hp}\|E_{el}$	Uncertainty
57	CO 4th Positive Band Oscillator Strength	–	–	–	±40%
58	$CO(a^3\Pi) + e^- \leftrightarrow CO(A^1\Pi) + e^-$	1.49e-05	-0.74	27860	+/- 2 om
59	$CN(A^2\Pi^+) + M \leftrightarrow CN(B^2\Sigma^+) + M$	M dependent			+/- 1 om
60	$CO(X^1\Sigma^+) + M \leftrightarrow CO(A^1\Pi) + M$	2.52E-09	0.344	93669	+/- 1 om
61	$CO(a'^3\Sigma^+) + M \leftrightarrow CO(d^3\Delta) + M$	M dependent			+/- 2 om
62	$CO(e^3\Sigma^-) + M \leftrightarrow CO(A^1\Pi) + M$	8.78e-11	0.498	971	+/- 2 om

$$K_{f,ij}^{hp} = A_{hp} {T_{ve}}^{n_{hp}} exp(-E_{hp}/T_{ve}) \tag{A.2}$$

$$K_{f,ij}^{el} = A_{el} {T_{ve}}^{n_{el}} exp(-E_{el}/T_{ve}) \tag{A.3}$$

Table A.4. Uncertain binary collision interactions for transport property modeling with ±30% uncertainty

#	Interaction	$\Omega^{1,1}$ A Parameter	$\Omega^{2,2}$ A Parameter
21	O_2-N	7.72e+01	8.46e+01
22	NO-N	9.95e+01	1.09e+02
23	NO-O	7.55e+01	8.26e+01
24	C-C	5.52e+04	1.22e+04
25	C-N	2.51e+05	2.89e+04
26	N_2-N	4.05e+03	1.93e+03
27	O_2-O	6.16e+02	3.40e+02
28	N_2-N_2	8.10e+00	2.14e+03
29	O-O	2.09e+00	8.33e+02
30	N-N	3.36e+00	2.13e+03
31	N-O	1.66e+03	4.45e+02
32	N_2-O_2	8.94e+02	5.22e+03
33	N_2-O	4.07e+02	4.08e+03
34	CO-N	3.01e+02	1.33e+03
35	CO_2-CO_2	3.83e+04	9.39e+04
36	CO_2-C	8.81e+01	9.62e+01
37	CO_2-N	1.02e+02	1.12e+02
38	CO_2-O	7.64e+01	8.33e+01
39	NO-C	8.94e+01	9.80e+01
40	CO-C	8.62e+01	9.42e+01
41	CO-O	6.91e+01	7.56e+01
42	O_2-C	7.70e+01	8.43e+01
43	C-O	1.08e+04	9.88e+03
44	N_2-C	4.26e+03	1.65e+03
45	N_2-NO	1.29e+02	1.24e+03
46	O_2-O_2	1.41e+02	1.81e+03
47	O_2-NO	1.14e+02	2.00e+03
48	NO-NO	7.25e+01	2.31e+03
49	CO-CO	2.13e+02	7.16e+02
50	N_2-CO	2.13e+02	7.16e+02
51	O_2-CO	1.39e+02	1.09e+03
52	CO-NO	1.29e+02	1.24e+03
53	CO_2-CO	1.59e+03	1.38e+04
54	CO_2-NO	1.67e+03	2.40e+04
55	CO_2-N_2	1.59e+03	1.37e+04
56	CO_2-O_2	1.85e+03	1.74e+04

II. UNCERTAINTY ANALYSIS OF FLUID-STRUCTURE INTERACTION OF A DEFORMABLE HYPERSONIC INFLATABLE AERODYNAMIC DECELERATOR

Andrew J. Brune **Serhat Hosder**

Missouri University of Science and Technology, Rolla, MO, 65409

Karl T. Edquist

NASA Langley Research Center, Hampton, Virginia 23681

ABSTRACT

The objective of this paper is to present the results of a detailed uncertainty analysis for high-fidelity fluid-structure interaction modeling of a deformable Hypersonic Inflatable Aerodynamic Decelerator at peak heating conditions for lifting Mars entry with turbulent flow assumption. Uncertainty results are presented for the structural deformation response and surface conditions (pressure, shear stress, and convective heat transfer) of the inflatable decelerator with an efficient polynomial chaos expansion approach. The uncertainty results are compared to results obtained in a previous study for ballistic Mars entry. Approximately half of the flowfield and structural modeling uncertainties show at least 90% contribution, combined, to the inflatable decelerator deflection and resulting surface condition uncertainties. For lifting Mars entry, global nonlinear sensitivity analysis shows that the tensile stiffness of the inflatable structure's axial cords and radial straps, and torus torsional and tensile stiffnesses are the main contributors to the inflatable decelerator deflection uncertainty. As a result of these structural uncertainty contributions, the shape deformation contributes up to 10% of the uncertainty in the surface conditions. However, the

freestream density dominates the uncertainty in the surface conditions experienced by the inflatable decelerator. In addition, the CO_2-CO_2 binary collision interaction is a significant contributor to aerodynamic heating and shear stress uncertainty.

NOMENCLATURE

C_D	Drag Coefficient	T	Static Temperature (K)
C_f	Skin Friction	V	Velocity (m/s)
C_L	Lift Coefficient	x	Deterministic Variable
f_1, f_2	Temperature-Dependent Curve Fits	α	Deterministic Coefficient in the Polynomial
h	Altitude (km)		Chaos Expansion
L/D	Lift-to-drag Ratio	α^*	Generic Uncertain Response Function
n	Number of Random Dimensions	β	Ballistic Coefficient (kg/m^2)
N_s	Number of Samples	$\gamma_{FPA,i}$	Initial Entry Flight Path Angle (deg)
N_t	Number of Terms in a Total-Order	δ	Truncation Error or Deflection Angle (deg)
	Polynomial Chaos Expansion	ρ	Static density (kg/m^3)
p	Order of Polynomial Expansion	Ψ	Random Basis Function
P	Surface Pressure (Pa)	$\Omega^{1,1}$	Diffusion Collision Integral
Re	Reynolds number (/m)	$\Omega^{2,2}$	Viscosity Collision Integral
q	Dynamic Pressure (Pa)	ξ	Standard Input Random Variable
S_e	Percent Absolute Error	μ_e	Mean Error
S_T	Total Sobol Index	∞	Freestream Condition

1. INTRODUCTION

NASA recently evaluated vehicle concepts and technology investments required to enable human and large robotic payload missions to Mars of ∼20-50 metric tons (t). In an effort to identify the most viable investment path, the Entry, Descent, and Landing System Analysis team [1, 2, 3] was tasked to conduct studies in continuation of work that resulted in the Mars Design Reference Architecture [4] study of 40-t class systems. Architecture-level assessments of these studies have shown that it is impossible to safely land systems of this size with heritage EDL systems that have been used to date. Multiple deceleration concepts were identified to meet enhanced payload capability, including a Hypersonic Inflatable Aerodynamic Decelerator (HIAD). Advantages anticipated with the use of HIADs over traditional rigid aeroshells include mass and volume savings of the stowed configuration, lower ballistic coefficients compared to rigid aeroshells, and reduced thermal environment of the deployed shape due to increased drag area. As the HIAD technology continues to mature, engineers will need accurate predictive models to obtain robust and reliable designs.

With recent advancements in computational resources and development of efficient and accurate methodologies, fluid-structure interaction simulations that couple computational fluid dynamics (CFD) and finite element analysis (FEA) have become an attractive approach for prediction of the structural response of a HIAD system. Tanner [5] performed fluid-structure interaction (FSI) analysis of the static aeroelastic behavior for a supersonic inflatable aerodynamic decelerator test article. However, similar efforts for a HIAD do not currently exist in the literature, although FSI investigation has been ongoing with subject matter experts through NASA's Space Technology Mission Directorate. NASA's HIAD

technology development project recently tested a 6m stacked torus inflatable article. Multiple aerodynamic wind tunnel and static pressure load tests [6, 7, 8] were conducted to characterize the inflatable structure response under relevant mission loading. Accurate prediction of the structural response of the HIAD inflatable structure under aerothermal and mechanical loads presents a challenge in the presence of uncertainties associated with the complex high-fidelity models. Deflections associated with the flexible inflatable structure can also impact the surface conditions of the HIAD, such as aerodynamic heating, pressure, and shear stress. Accurate quantification of these uncertainties is vital to design a robust and reliable HIAD configuration.

Efficient uncertainty quantification (UQ) methods have become the preferred approach over traditional sampling techniques, such as Monte Carlo, because they can provide accurate results while addressing the issue of increased computational demand of high-fidelity deterministic models for large-scale problems. Previous works, such as Bettis and Hosder [9, 10] and Hosder et al. [11, 12], have extensively investigated the practical use of stochastic expansions based on non-intrusive polynomial chaos (NIPC) as a means of efficient UQ, which include propagation of both aleatory and epistemic uncertainties. The theory behind the NIPC methodologies is well-defined in the literature [13, 14] and serves as a reliable method for UQ in complex aerospace simulations. West and Hosder [15] extended this work by demonstrating a multi-step NIPC UQ approach for quantifying the top contributing uncertainties to shock-layer radiation. Furthermore, West and Hosder [16] developed a sparse approximation NIPC technique to reduce the computational cost for UQ by utilizing a reduced set of samples to achieve accurate uncertainty results compared to the original NIPC technique, which will be the basis of the UQ approach in the current study.

In previous work by the authors [17], uncertainty analysis was performed over a rigid HIAD-like shape subject to a large number of mixed uncertainties, which included aleatory (inherent) uncertainties in the operating (freestream) conditions and epistemic uncertainties in the binary collision interaction and chemical reaction rate modeling of the chemically-reacting flowfield. The uncertainties in the surface conditions (heat flux, pressure, and shear stress) were quantified, and the most significant uncertain parameters were identified based on global nonlinear sensitivity analysis to relatively rank the uncertainty sources. The information obtained from this previous study is used in the current work.

The objective of this paper is to present the results of a detailed uncertainty analysis for high-fidelity, static fluid-structure interaction (FSI) modeling of a deformable HIAD configuration at peak heating conditions (assuming turbulent flow) for a lifting entry mission profile, which is defined by the EFF4 architecture in the EDL-SA study [3]. Brune et al. [18] conducted similar work for FSI uncertainty analysis of the same HIAD at peaking heating of a ballistic entry profile with turbulent flow assumption to simulate conservative heating and shear stresses on the HIAD surface, which is referenced in later discussions for comparison to the findings in this work. This study uses a stochastic expansion approach with sparse approximation [16] for efficient quantification of uncertainty in various output quantities of interest. Uncertainty results are presented for the deflection and surface conditions of the flexible HIAD subject to a number of epistemic and aleatory uncertainties in physical modeling parameters associated with the flowfield and inflatable structure. This study introduces the uncertainty sources in the structural modeling parameters of the HIAD and will include the important flowfield uncertainty sources (binary collision interactions and freestream conditions) that were shown to significantly contribute to the wall pressure and shear stress uncertainties in a previous study by the authors [17].

The following section describes the UQ methodology used in the current study. The high-fidelity deterministic model for coupled FSI, HIAD configuration and baseline conditions, baseline reference case results, and stochastic problem are presented in Section 3. Uncertainty assessments of the structural response (deformation) and the resulting surface conditions of the HIAD in the presence of structural model and flowfield uncertainties at peak heating of the lifting trajectory are discussed in this section. Concluding remarks are given in Section 4.

2. UNCERTAINTY QUANTIFICATION METHODOLOGY

In recent studies [9, 10, 12, 19, 20], the polynomial chaos method has been used as a means of UQ over traditional methods, such as Monte Carlo, for computational efficiency. Polynomial chaos is a surrogate modeling technique based on a spectral representation of the uncertainty. An important aspect of spectral representation of uncertainty is that a response value or random function α^* (such as surface heat flux or deflection at a particular surface location) can be approximated as a series with each term decomposed into separable deterministic and stochastic components, as shown in Eq. (2.1).

$$\alpha^*(\mathbf{x},\xi) \approx \sum_{i=0}^{P} \alpha_i(\mathbf{x})\Psi_i(\xi) \tag{2.1}$$

Here, α_i is the deterministic component and Ψ_i are the random variable basis functions corresponding to the ith mode. α^* is assumed to be a function of the deterministic variable vector $\mathbf{x}$ and the n-dimensional standard random variable vector ξ. By definition, this series is infinite; however, it can be truncated with a discrete sum over a number of output modes [14]. To form a complete basis or a total order expansion, the truncated series can be represented with N_t number of terms, which will depend on the polynomial chaos expansion (PCE) of order p and the number of random variables, n:

$$N_t = P + 1 = \frac{(n+p)!}{n!p!} \tag{2.2}$$

Further details on polynomial chaos theory are given by Walters and Huyse [13] as well as Eldred [14].

To determine the expansion coefficients, α_i, without any modifications to the deterministic code (i.e., CFD code), several non-intrusive polynomial chaos (NIPC) methods have been developed. Of these, the point-collocation NIPC method has been used extensively in many aerospace simulations and CFD problems [10, 12, 20, 15]. The point-collocation method starts with replacing a stochastic response or random function with its PCE using Eq. (2.1). Then, N_t vectors are chosen in random space, and the deterministic code is then evaluated at these points to represent the left hand side of Eq. (2.1). Following this, a linear system of N_t equations can be formulated and solved for the spectral modes of the random variables, shown in Eq. (2.3).

$$\begin{pmatrix} \alpha^*(\mathbf{x},\xi_0) \\ \alpha^*(\mathbf{x},\xi_1) \\ \vdots \\ \alpha^*(\mathbf{x},\xi_P) \end{pmatrix} = \begin{pmatrix} \Psi_0(\xi_0) & \Psi_1(\xi_0) & \cdots & \Psi_P(\xi_0) \\ \Psi_0(\xi_1) & \Psi_1(\xi_1) & \cdots & \Psi_P(\xi_1) \\ \vdots & \vdots & \ddots & \vdots \\ \Psi_0(\xi_P) & \Psi_1(\xi_P) & \cdots & \Psi_P(\xi_P) \end{pmatrix} \begin{pmatrix} \alpha_0 \\ \alpha_1 \\ \vdots \\ \alpha_P \end{pmatrix} \tag{2.3}$$

Note that for this linear system, N_t is the minimum number of deterministic samples (N_s) required to obtain a solution of the determined system (i.e., the coefficient vector). If more samples are available (N_s>N_t) and linearly independent, the system is considered overdetermined and can be solved using a least squares approach. Polynomial chaos techniques, however, suffer from a "curse of dimensionality" in the sense that the number of deterministic model evaluations required to create an accurate surrogate model grows exponentially with the number of random dimensions. For many large-scale, complex problems, such as those found in modeling hypersonic reentry flows, it may be impractical to obtain the minimum required number of deterministic model samples. The most desirable approach is to obtain an accurate surrogate model with as few deterministic samples as possible to limit the computational cost.

If a case which has the number of deterministic model samples less than the minimum required for the solution to the determined system (N_s<N_t) is considered, then a system of linear equations is obtained that has fewer linearly independent equations than unknowns and possesses an infinite number of solutions. In a recent study by West and Hosder [16], it was shown that a small fraction of the PCE coefficients carry significant weight in the surrogate model. With the assumption that the expansion coefficient vector is sparse, the linear system can be regularized allowing for a well-posed solution. West and Hosder [16] presented a solution technique used by Asif [21] with the L_1-minimization problem using convex relaxation, where the objective is to seek a solution to the linear system with the fewest number of non-zero coefficients.

$$\min \left\| \alpha \right\|_1 \text{ subject to } \left\| \Psi\alpha - \alpha^* \right\|_2 \leq \delta \tag{2.4}$$

Here, δ is the error associated with the truncation of the series in Eq. (2.1). For the problems considered in this study, δ is assumed to be equal to zero, as it can be shown that the solution to Eq. (2.4) is unique with this assumption [22]. In the above formulation, the dimensions of Ψ are N_s x N_t and the vector α^* is of length N_s. The vector α is of length N_t. Doostan and Owhadi [22] discuss, in great detail, the theory and formulation of the above method.

The optimization problem in Eq. (2.4) is commonly referred to as Basis Pursuit Denoising (BPDN) [22, 23, 21]. In the current study, the least absolute shrinkage and selection operator (LASSO) homotopy optimization routine [21] was selected to find the optimal solution of Eq. (2.4) and is shown to be efficient due to its convergence being weakly dependent on the dimension of the problem [23].

With this optimization and sparse-collocation approach, a procedure is followed for determining an acceptable sample size to achieve convergence and accuracy of the poly-

nomial chaos expansion. The first step in this process is to generate an initial sample set of the uncertain variables. The size of this initial sample set, generated using Latin Hypercube sampling, is taken as the size, N_t, given by Eq. (2.2) as this would be the minimum number of samples required to obtain a total order expansion. Note that generating large sample sets of the uncertain parameters is not computationally expensive compared to the cost of evaluating the deterministic model. A small subset of the initial sample structure is selected, and the deterministic model is evaluated at these points. Then, a first set of PCE coefficients can be obtained using the minimization routine in Eq. (2.4). This process is then repeated by iteratively adding more samples to the solution procedure (i.e., addition of new subsets of the full sample structure) until the convergence of the expansion coefficients is achieved. Each subset of the full sample structure added at each iteration is restricted to not contain any repeated sample vectors from the previous iterations so that new information is provided in recovering a new solution at each iteration. West et al. [16] and Brune et al. [17] discuss this approach in detail with example problems related to this work.

Convergence of the expansion coefficients is checked at each iteration. West and Hosder [16] presents methods used to track the convergence of the expansion coefficients and the resulting polynomial expansion. In this work, a method for variance-based global sensitivity analysis measures, Sobol indices [24, 25], is used to measure the convergence of the expansion coefficient vector as the Sobol indices highly depend on the coefficients of the PCE. Further detail on this dependence and the derivation of total Sobol indices is given by West and Hosder [16]. The total Sobol index for each uncertain variable j ($S_{T,j}$) provides a sensitivity measure in terms of its total contribution to the total variance of the output quantity of interest. To monitor the convergence of the total Sobol indices with the addition of more samples at each iteration, an absolute error, $S_{e_{i,j}}$ can be defined for the j^{th} total Sobol index at iteration i using Eq. (2.5).

$$S_{e_{i,j}} = \left\| S_{T,i,j} - S_{T,i-1,j} \right\| \tag{2.5}$$

Note that measuring the convergence based on this absolute error puts emphasis on the variables that contribute to the output uncertainty more significantly. The errors of each total Sobol index, at each iteration, can then be averaged giving a single value for monitoring, which is shown in Eq. (2.6).

$$\mu_{e,i} = \frac{1}{n} \sum_{j=1}^{n} S_{e_{i,j}} \tag{2.6}$$

Plotting this average error at each iteration would then illustrate the convergence of the PCE coefficients. The objective is to seek out nearly asymptotic convergence, as zero error would likely not be achievable simply due to the randomness of the samples added at each iteration and any numerical noise that may occur during the analysis of complex models.

In this work, the stochastic problem contains both aleatory and epistemic types of uncertainty. For mixed uncertainty for which contributions of both types of uncertainty are considered, a procedure known as second-order probability [14] is used to propagate the mixed uncertainty through the stochastic model. Details on the uncertainty classification and second-order probability approach can be found in previous work which have been used to validate the UQ approaches and methodologies presented in this section [17, 15, 16].

3. UNCERTAINTY ANALYSIS OF HIGH-FIDELITY FLUID-STRUCTURE MODELING OF A HIAD

This section presents an overview of the coupled fluid-structure interaction deterministic model (Section 3.1), the HIAD configuration and baseline reference conditions used in this problem (Section 3.2), baseline reference case results (Section 3.3), and the stochastic model for implementing the polynomial expansion UQ approach with sparse approximation (Section 3.4). A detailed uncertainty assessment of the HIAD shape deformation and surface conditions is presented in Section 3.5 in the presence of uncertainty in the flowfield and structural model. Discussion will primarily cover the lifting entry uncertainty results at peak heating, while comparing these results to those found for ballistic entry at peak heating by Brune et al. [18]

3.1. DESCRIPTION OF THE DETERMINISTIC MODEL

In this work, the Fully Unstructured Navier-Stokes 3D (FUN3D) flow solver [26] from NASA Langley Research Center is used for the high-fidelity numerical solution of the flowfield over a HIAD. FUN3D uses a three-dimensional node-based, finite-volume discretization approach which includes a suite of capabilities and features for simulation and design. Primary capabilities of FUN3D include algorithms for unstructured-grid fluid dynamic simulations of compressible flows with frozen, equilibrium, or nonequilibrium thermo-chemistry. Parallel domain decomposition with message passing interface is available for distributed computing and adjoint/feature-based adaptation to resolve shock gradients of high-speed flows. FUN3D also incorporates point-implicit or line-implicit relaxation schemes to perform expensive computations for problems on a complex scale and grid

motion algorithms for problems which require rotation, transformation, and deformation. The flowfield for the current study is modeled using the multi-species, two-temperature, thermochemical nonequilibrium capability for a Mars 8-species composition: CO_2, CO, N_2, O_2, NO, C, N, and O. This analysis focuses on modeling the flowfield with a turbulent boundary layer using the Spalart-Catris turbulence model to simulate conservative heating and shear stresses on the surface of the HIAD [27, 28]. For all results presented in this work, Yee's symmetric total variation diminishing inviscid flux scheme [29] is used with second order spatial accuracy construction of the inviscid flux terms. In addition, all viscous fluxes were obtained with second order spatial accuracy. An Euler implicit backwards differencing time integration scheme [26] was implemented for pseudo (local) time stepping to accelerate convergence of the flow to steady state. The NASTRAN structural solver [30] of MacNeal-Swendler Coporation (MSC) is loosely-coupled with the FUN3D flow solver to obtain the structural response (deformation) of the HIAD in the presense of external pressure and shear loads.

The coupled fluid-structure interaction approach, shown in Figure 3.1, uses a multi-step scheme for loosely coupling the CFD and FEA analyses. Initially, surface pressure and shear stress distributions on the undeformed (or as-designed) HIAD shape are obtained with the FUN3D flow solver. Surface force distributions from the flow solver are then converted to nodal force values and mapped to the finite element model (FEM). Data are transferred between two dissimilar grids since the flow and structural solvers require different grid formulation and construction. A discrete data transfer (DDT) routine developed by Samareh [31] is used to transfer discrete data between dissimilar grids for loosely-coupled FSI analyses. The DDT routine uses the inverse isoparametric mapping (IIM) method to interpolate data. This formulation interpolates data from source nodes to target elements (and vice versa) using the element's shape (or basis) function, and it is formulated to con-

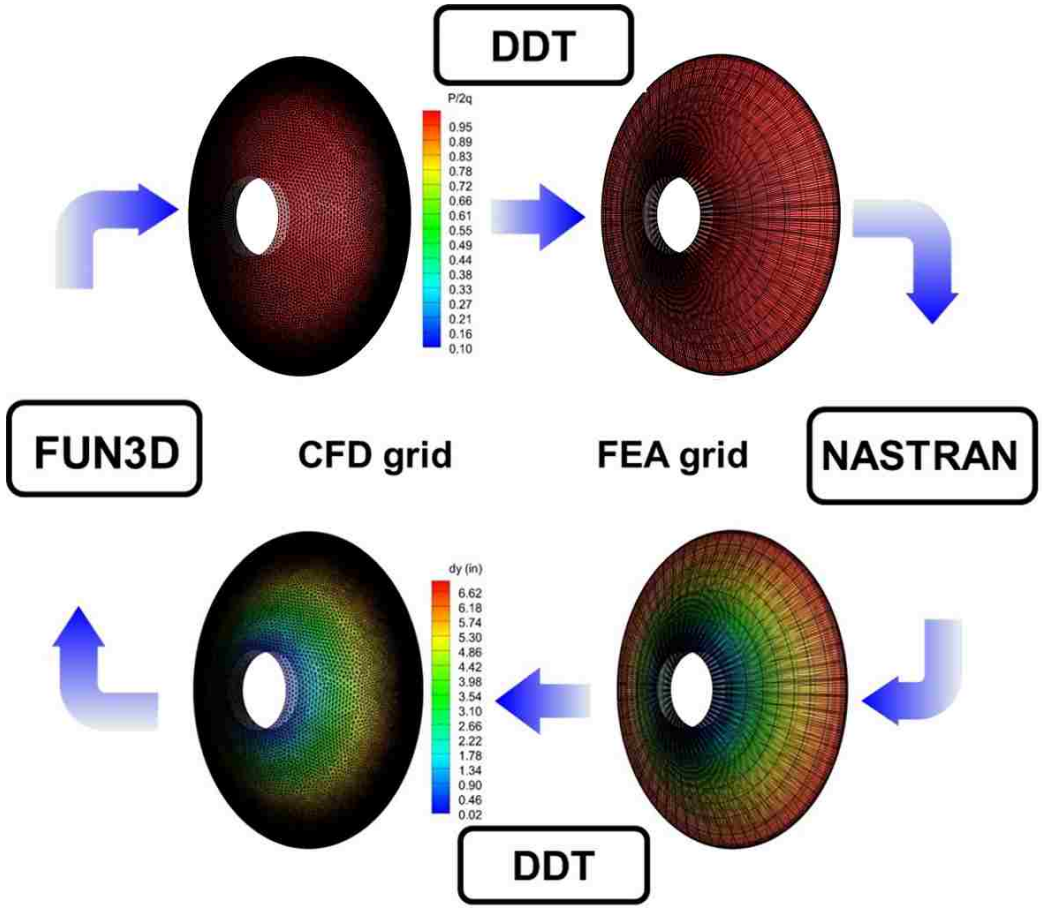

Figure 3.1. Loosely-coupled FSI approach for prediction of the HIAD shape deformation

serve force and virtual work between dissimilar grids. Deflections are calculated by the NASTRAN structural solver with the supplied aerodynamic nodal forces. These deformations are mapped back to the surface grid of the fluid dynamics model and are used to deform the CFD volume mesh to accommodate the new surface geometry. Up to this point, a single FSI cycle is completed. This cycle process is repeated iteratively until both fluid and structure solutions converge such that no significant change in the aerodynamic forces and the structural deformations are observed.

3.2. BASELINE REFERENCE GEOMETRY AND FREESTREAM CONDITIONS

A 10m stacked torus configuration is used for all FSI calculations. The dimensions were scaled from the 6m article that was tested in the 40 x 80 foot test section of the NASA Ames National Full-Scale Aerodynamics Complex (NFAC) facility. The 6m HIAD (shown in Figure 3.2) has a 60-deg sphere cone stacked torus design that consists of seven major tori (T1-T7) 14 inches in diameter and an eighth torus at the shoulder 8 inches in diameter (T8). The toroids are modeled as an orthotropic laminate smear in combination of the Technora bias braid, Kevlar webbing, Urethane membrane, and structural adhesive material properties [6]. In addition, Technora cords are also incorporated as a separate entity to improve the stiffness of the structure and sustain the shape. The inflatable structure described is bonded and attached to a 1.7m diameter rigid centerbody with a series of Kevlar webbing straps. The Kevlar webbing straps distribute flight loads from torus to torus and to the centerbody. The network of straps include 4000-lb (4-K) load radial and centerbody attachment straps attached to T5 and 3000-lb (3-K) load pairing and chevron straps attached to T6 and T7 [6, 7]. Figure 3.3 depicts the strap and Technora axial cord components. It should be emphasized that the properties of the cords and straps were modeled in NASTRAN with non-linear elasticity and assumed as isotropic. The torus structure properties were modeled with orthotropic behavior and linear elasticity. The inflation pressure is set to 15 psi based on previous experimental work at NFAC [32, 33].

An Exploration Feed Forward (EFF) study investigated an EFF4 architecture with a 5.8 km/sec direct entry [3]. The baseline freestream condition is taken to be at peak stagnation point heating for the 10m HIAD, derived from a six degree-of-freedom dynamics simulation. Figure 3.4 presents the ballistic and lifting entry profiles corresponding to the EFF4 reference mission. The reentry dynamics model is shown to have excellent agreement with a model presented by Cruz and Munk [34] (Figure 3.5).

Figure 3.2. 6m test article at NFAC test facility

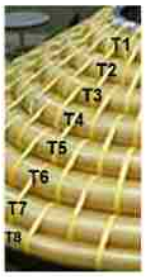

(a) Pairing 3000-lb (3-K) straps [6]

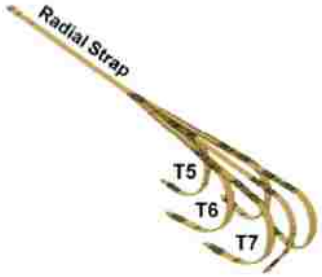

(b) Radial 4000-lb (4-K) and Chevron 3-K straps [6]

(c) Technora axial cord embedded in the torus [33]

Figure 3.3. HIAD Kevlar strap and Technora cord configuration

Uncertainty analysis is performed at peak heating for the ballistic and lifting entry profiles, corresponding to freestream conditions listed in Table 3.1. The results of the uncertainty analysis at peak heating for lifting entry will be discussed and compared with ballistic entry uncertainty results in Section 3.5. The freestream gas composition is assumed to be 96% CO_2 and 4% N_2 by mole. The wall of the HIAD is modeled with a constant temperature of 1500 K and super-catalytic conditions (species composition set to freestream mass fraction values of CO_2/N_2) to simulate worst-case heating conditions,

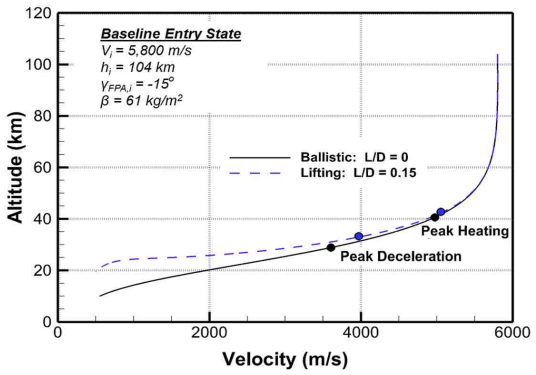

Figure 3.4. Ballistic and Lifting Entry Profiles for EFF4 Reference Mission

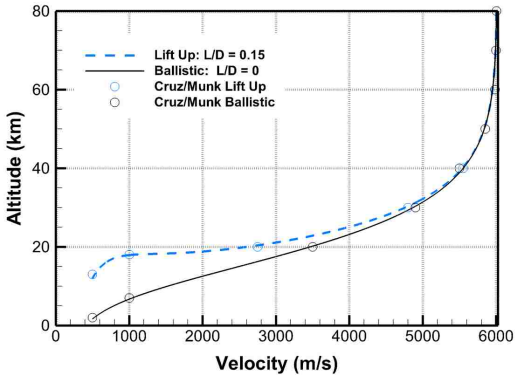

Figure 3.5. Lifting and ballistic entry comparisons with Cruz and Munk 3-DOF and current study 6-DOF reentry models

Table 3.1. Summary of baseline reference peak heating conditions

Case Description	AoA, α (deg)	V_∞ (m/s)	ρ_∞ (10^4 kg/m^3)	T_∞ (K)	Re_∞ (10^5 /m)
Ballistic Entry (L/D=0)	0	5273	2.18	160	2.26
Lifting Entry (L/D=0.15)	15	5353	1.98	158	1.35

strongly emphasizing that little information is available on the wall material for modeling wall catalysis [17].

3.3. BASELINE REFERENCE CASE RESULTS FOR THE LIFTING ENTRY TRAJECTORY

The baseline reference solution for lifting entry at peak heating was first computed using FUN3D with an adapted grid of the ballistic entry case at peak heating, shown in Figure 3.6 [18]. The adapted grid is derived from an initial grid that was used for NFAC wind tunnel test cases [6, 7]. The HIAD in this grid has a cylindrical centerbody, which represents the sting attachment. The length of the centerbody is equivalent to the length

of the sting attachment from NFAC wind tunnel testing [6, 7]. A flight HIAD would have a rigid centerbody that might be similar in diameter to the sting. Grid convergence effects were determined by recomputing the flowfield using feature-based adaptation. With an initial ballistic entry adapted grid (11.4 million nodes), two complexity levels to target the grid size were constructed using adaptation based on pressure gradients and Mach anisotropy in the shock layer. Note that the adaptation procedure was implemented by freezing the boundary layer grid cells from the surface to a distance of approximately 0.001 meters since the initial grid had a well-defined boundary layer resolution with y^+ values between 0.4-0.5. This resolution was determined to be sufficient for turbulent boundary layer calculations because the converged y^+ values are proved to be less than 1.0 over the HIAD surface. Table 3.2 presents the aerodynamic coefficients and Tables 3.3-3.4 show the non-dimensional wall pressure and skin friction for five locations on the HIAD surface in Figure 3.8 at two grid levels after adaptation. The grids were adapted in sequence, resulting in a nominal grid (11.4 million nodes) and a fine grid (13.1 million). As expected, the final skin friction and wall pressures are significantly different from the initial ballistic entry adapted grid values. Furthermore, the nominal and fine grid levels for lifting entry show remarkably similar results with variations less than 1%. This difference was acceptable, considering the much higher differences between initial ballistic entry adapted and nominal adapted grids. Therefore, the nominal grid level (11.4 million nodes) was considered to be reasonable to capture the shock layer and boundary layer features of the flowfield.

Table 3.2. Aerodynamic coefficients for a range of adapted grid sizes

Grid Size (10^6 nodes)	C_L	C_D
11.4 (ballistic)	0.2189	1.382
11.4	0.2109	1.394
13.1	0.2109	1.394

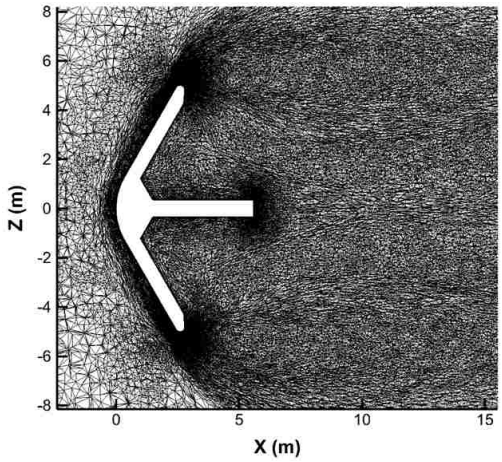

Figure 3.6. Centerline slice of adapted grid for ballistic entry at peak heating (11.4 million nodes)

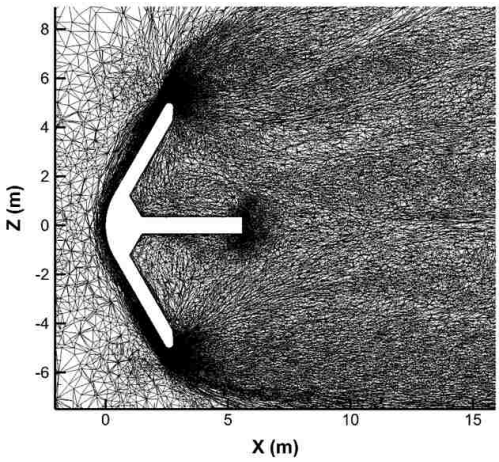

Figure 3.7. Centerline slice of adapted grid for lifting entry at peak heating (11.4 million nodes)

Table 3.3. Surface pressure at selected HIAD locations for a range of adapted grid sizes

Grid Size (10^6 nodes)	$P_1/2q_\infty$	$P_2/2q_\infty$	$P_3/2q_\infty$	$P_4/2q_\infty$	$P_5/2q_\infty$
11.4 (ballistic)	0.900	0.648	0.272	0.0028	0.0019
11.4	0.913	0.652	0.277	0.0028	0.0020
13.1	0.912	0.652	0.277	0.0029	0.0020

Table 3.4. Surface skin friction at selected HIAD locations for a range of adapted grid sizes

Grid Size (10^6 nodes)	$C_{f,1}$	$C_{f,2}$	$C_{f,3}$	$C_{f,4}$	$C_{f,5}$
11.4 (ballistic)	0.0101	0.0328	0.0249	0.0028	0.000039
11.4	0.0103	0.0332	0.0245	0.0029	0.000034
13.1	0.0103	0.0333	0.0246	0.0029	0.000032

After each cycle in FUN3D, pressure and skin friction data are mapped with DDT [31] to the FEA surface grid in terms of nodal forces. The FEA surface grid (see Figure 3.1 in the previous subsection) is implemented as a nodal force boundary condition in NAS-

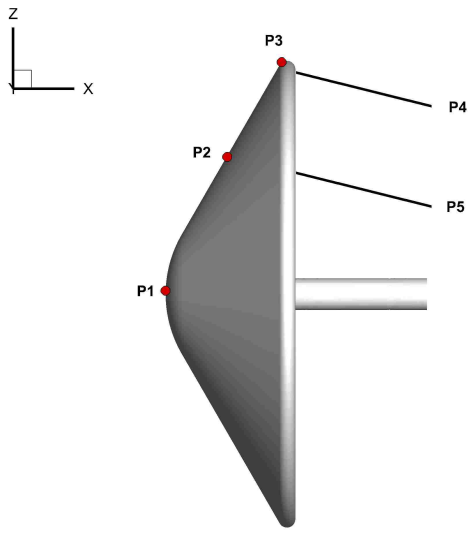

Figure 3.8. Selected HIAD surface locations for convergence monitoring

TRAN using a full 360-deg model that resembles the configuration shown in Figure 3.2 with 10m major diameter. The resulting nodal displacements are mapped back to the CFD surface grid for subsequent FSI cycles.

In Figures 3.13 and 3.14, the deflected HIAD surfaces along the centerline pitch plane are presented for each FSI cycle and compared with the initial (as-designed) surface. Figure 3.15 provides a three-dimensional view of the deflected and undeflected HIAD surfaces. Little disparity is observed between the deflected surfaces of cycle 1 and 2. Further numerical checks of the deflection magnitude and components indicate differences between both cycles of less than 1-2%. Therefore, only two FSI cycles are needed to converge the surface conditions and the deflections of the HIAD. Figure 3.15 also provides a top view of the HIAD with indicated radial slices at 45 degree increments. The radial deflections of the HIAD are presented at these incremental slices in Figure 3.16. The maximum and

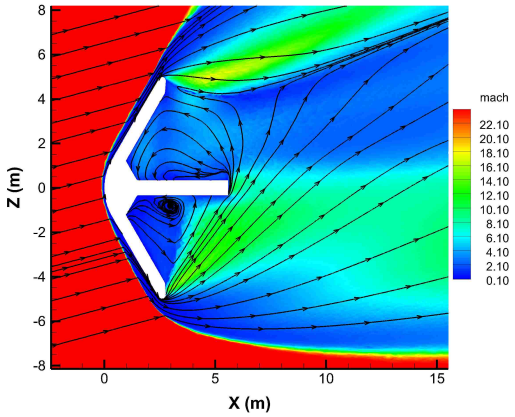

Figure 3.9. Mach number for the adapted grid (11.4 million nodes) with shock layer and wake afterbody visualization

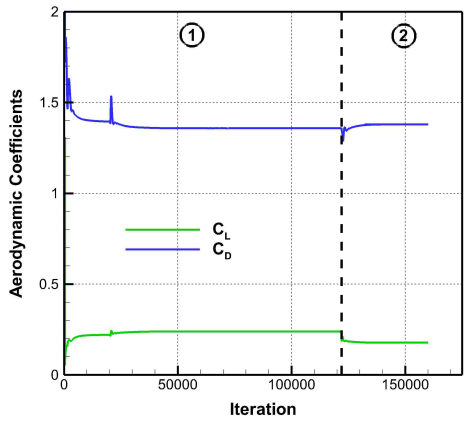

Figure 3.10. Drag coefficient history for the baseline reference case

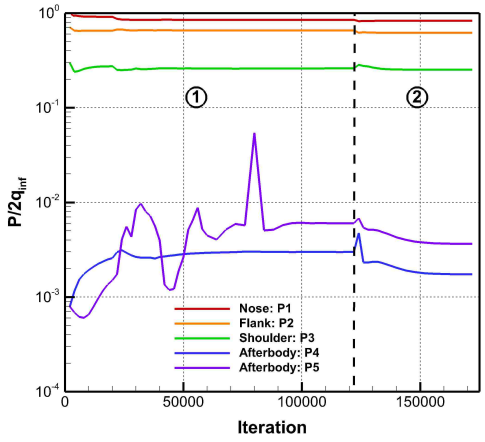

Figure 3.11. Pressure history at selected surface points for the baseline reference case

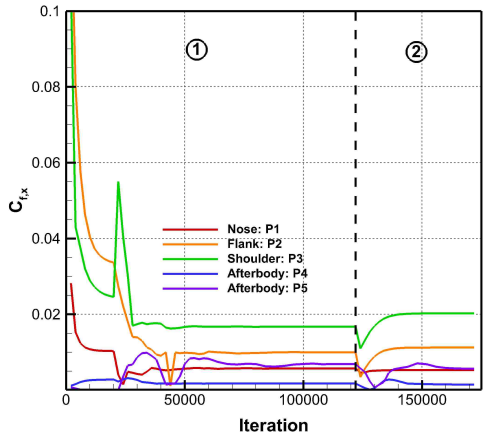

Figure 3.12. Skin friction history at selected surface points for the baseline reference case

minimum deflection of the HIAD are located in the pitch plane, where the 0-deg. and 180-deg. radial slices reside. Figures 3.17 and 3.18 present the surface pressure and convective heating of the HIAD after performing two FSI cycles. The critical pressure and heating

distributions with maximum values are clearly shown to exist in the same plane on both the leeward and windward side. Therefore, this work will focus on uncertainty analysis of the deflections and surface conditions within the pitch plane.

The computational cost of a single FSI case (with two FSI cycles) is substantial with approximately 125 hours of computing time. 260 processors (Dual socket 8-core GHz Intel E5-2670 Sandybridge) with two gigabytes access memory each were used for CFD analysis. Two processors of the same architecture were used to complete the FEA analysis. Note that this provides an accurate measure of the cost of restarting a case with a baseline reference converged flowfield for the cases used in uncertainty analysis. For the baseline reference case, with flowfield initialization at the freestream values, the cost requirement for CFD analysis is approximately 168 hours. Table 3.5 presents the breakdown of the computing time for the CFD and FEA analysis segments. Considering the high computational demand for CFD analysis, this information justifies crucial support for using an efficient NIPC UQ approach with sparse approximation over traditional point-collocation NIPC or Monte Carlo approaches.

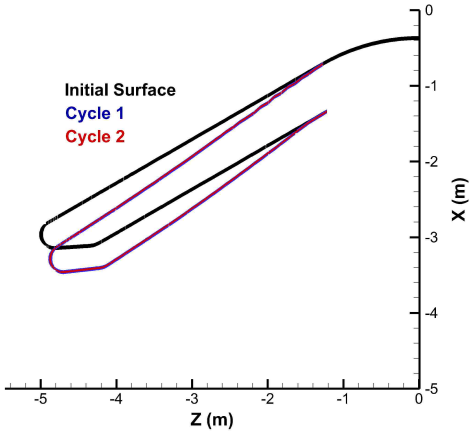

Figure 3.13. HIAD undeflected (initial) and deflected surfaces for each FSI cycle for the baseline reference case (windward)

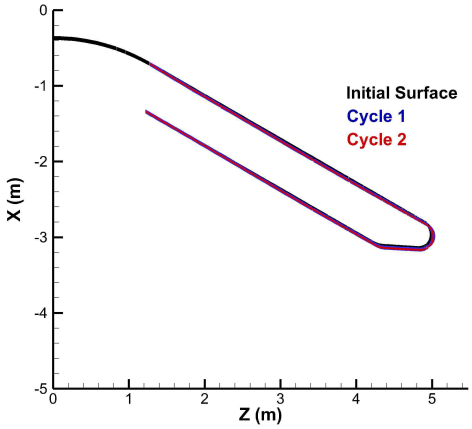

Figure 3.14. HIAD undeflected (initial) and deflected surfaces for each FSI cycle for the baseline reference case (leeward)

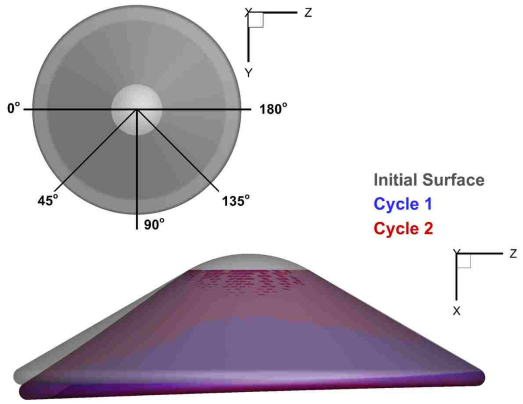

Figure 3.15. 3-D visualization of the undeflected (initial) and deflected HIAD surfaces for the baseline reference case

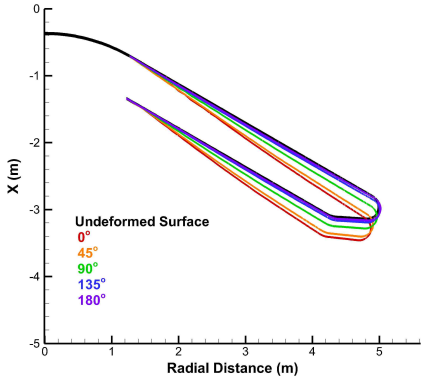

Figure 3.16. HIAD deflections at 45-deg. slice increments for the baseline reference case

3.4. DESCRIPTION OF THE STOCHASTIC PROBLEM

For this study, 16 uncertain input parameters related to flowfield and structural modeling of the HIAD, described in Section 3.1, are considered in the UQ analysis. Table 3.6

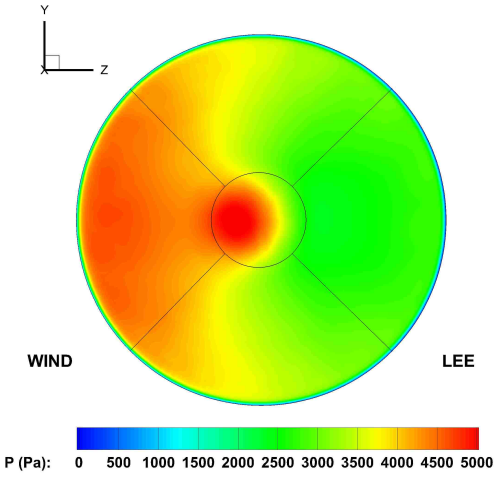

Figure 3.17. Forebody pressure at baseline reference peak heating conditions (lifting entry)

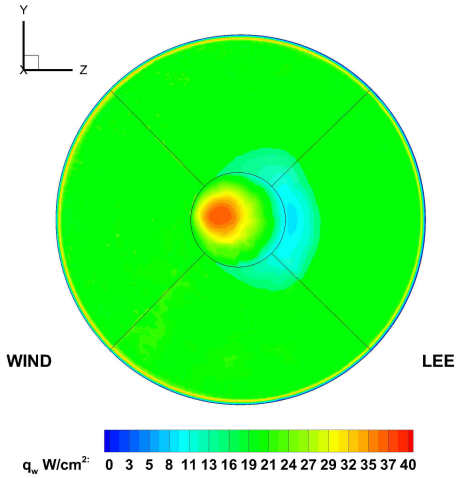

Figure 3.18. Forebody convective heating at baseline Reference peak heating conditions (lifting entry)

Table 3.5. Computing time (hours) for the baseline reference and dispersed cases (two FSI cycles)

Analysis Segment	Baseline Reference	Dispersions
FUN3D (CFD)	168	120
NASTRAN (FEA)	5	5

presents the various uncertainty source categories and assigned uncertainty ranges for the coupled FSI model, which are used in the UQ analysis for prediction of the deformation and surface conditions of the HIAD in Section 3.5. The first three uncertainties in Table 3.6 were identified from a detailed uncertainty analysis of the flowfield modeling parameters and freestream conditions in a previous work [17]. These three uncertainties were shown to contribute approximately 99% of the total uncertainty in the pressure and shear stress at the surface of a fixed aeroshell of HIAD scale, which can strongly affect the shape deformation of the HIAD. In particular, Table 3.7 presents the top contributing uncertain parameters

Table 3.6. Summary of uncertain parameters for the HIAD FSI simulations

Uncertain Parameter	Description	Classification	Uncertainty	Ref.
Wall Pressure/Shear Stress				
V_∞	Freestream Velocity	Normal	0.5% CoV	
ρ_∞	Freestream Density	Uniform	±30%	[17]
A	CO_2-CO_2 Collision Integral	Epistemic	±30%	
Structural Boundary Condition				
P_0	Inflation Pressure	Normal	2% CoV	
Tensile Stiffness (Elastic Modulus)				
E_c	Technora Cords	Epistemic	[-50%,+20%]	HIAD
E_{3K}	3-K Kevlar Straps	Epistemic	±20%	Inflatable
E_{4K}	4-K Kevlar Straps	Epistemic	±25%	Structures
E_L	Torus (Longitudinal)	Epistemic	±20%	test data
E_T	Torus (Transverse)	Epistemic	±20%	archive
Possion's Ratio				
ν_c	Technora Cords	Epistemic	±20%	
ν_{3K}	3-K Kevlar Straps	Epistemic	±20%	
ν_{4K}	4-K Kevlar Straps	Epistemic	±20%	
ν_{LT}	Torus (Uniaxial)	Epistemic	±15%	
Torsional Stiffness (Shear Modulus)				
G_{LT}	Torus (In-plane)	Epistemic	±25%	
G_{LN}	Torus (Out-plane)	Epistemic	±25%	
G_{TN}	Torus (Out-plane)	Epistemic	±25%	
TOTAL	**16**			

to the uncertainty in the shear stress for a turbulent boundary layer. Only the freestream density was shown to contribute the uncertainty in the wall pressure [17].

For this analysis, the freestream velocity and density are described through probabilistic measures due to its inherent nature. The freestream velocity input to the CFD simulation is treated as an aleatory uncertain variable with a normal distribution with a mean value (Table 3.1) and a coefficient of variance (CoV) of 0.5%. The freestream density was also treated as aleatory uncertain variable with uniform distribution and interval of ±30% from the baseline reference values in Table 3.1. The uncertainty ranges (CoV and uncertainty range assignments) were based on the uncertainty information obtained from a previous study [17].

Binary collision integrals have been shown to be important modeling parameters in high temperature flows to accurately model the transport quantities that govern the shear stress and heat flux at the HIAD surface. A study by Wright et al. [35] indicates that

Table 3.7. Uncertainty contributions to shear stress at selected HIAD surface locations for a turbulent boundary layer

Uncertainty Sources	Stagnation Point	Flank	Shoulder
CO_2-CO_2	57.7%	39.9%	37.9%
ρ_∞	24.0%	52.5%	62.0%
V_∞	16.5%	7.1%	0.1%

there can be as much as 30% uncertainty associated with binary collision integrals. The uncertainty in the CO_2-CO_2 interaction was modeled as epistemic due to lack of knowledge in the CFD physical model. The uncertainty in the binary collision integrals were implemented through the use of a single parameter, A, similar to the studies by Bettis et al. [36] and Bose et al. [37]:

$$\Omega^{1,1} = A f_1(T) \tag{3.1}$$

$$\Omega^{2,2} = A f_2(T) \tag{3.2}$$

The functions f_1 and f_2 are expressions with temperature dependence, and the form of the curve fits are presented by Gupta et al. [38] The A parameter (multiplier) in Eq. 3.1-3.2 is treated as the uncertain parameter with lower bound of 0.7 and upper bound of 1.3, which corresponds to a $\pm 30\%$ uncertainty [37]. In Eq. 3.1, $\Omega^{1,1}$ is used to calculate the diffusion coefficients. Likewise, in Eq. 3.2, $\Omega^{2,2}$ is used to calculate the viscosity coefficients. Furthermore, as noted by Wright et al. [39], both of these collision integrals are used to compute the thermal conductivity.

The remaining uncertainty sources listed in Table 3.6 represent the final category of uncertainty in the structural modeling and boundary condition parameters. The uncertain-

ties due to these parameters were determined by examination of material property data from experimental load testing and expert opinion from subject matter experts involved with structural modeling of the HIAD. Most of the uncertainties involve tensile/torsional stiffnesses and Poisson's ratio that capture the overall stiffness of the HIAD structural cords, straps, and tori components. Due to the lack of sufficient data to assign a probabilistic distribution, these stiffness parameters are modeled as epistemic uncertain variables with intervals. Finally, available statistical inflation pressure data from NFAC testing was used to determine that the observed inflation pressure follows a normal distribution with a true mean value of 15 psi and CoV of 2%.

3.5. UNCERTAINTY ASSESSMENT OF THE DEFORMABLE HIAD

3.5.1. Uncertainty Analysis of HIAD Surface Deformation. In this subsection, the efficient UQ approach presented in Section 2 is applied to assess deflection and surface condition uncertainties of the deformable HIAD. As shown in the previous subsection, 16 uncertainty sources associated with the flowfield and structural parameters are considered in this work. Using Eq. 2.2, a total of 153 samples are required to construct the response surface for a second order expansion with a given output response of interest (for example, deflection or surface pressure at a given surface location). This set of samples would ideally be used for point-collocation NIPC; however, the goal is reduce the number of required FSI simulations to limit the cost of function evaluations at a high-fidelity level with a sparse approximation approach.

Using the sparse approximation NIPC approach outlined in Section 2, the initial Latin-hypercube sample set is generated with 153 samples. An initial subset of two samples are used to create the response surface using the L_1 minimization homotopy routine (i.e., solve for the sparse coefficient vector of the surrogate model). Additional subsets of two

samples are iteratively added, without repeating samples, to train the surrogate model until convergence of the Sobol indices (or in theory, the expansion coefficients) is achieved. For each sample, two FSI cycles were run to assure convergence of the deflection and surface conditions of the HIAD, as illustrated in Section 3.3.

Figure 3.19 presents the normalized mean Sobol index error for each sample subset using Eq. 2.5 at sixteen HIAD surface locations along the pitch plane (eight points on both the windward and leeward side). With less than 20 samples, there is significant variation in the error because the response surface is not well trained with little information from the uncertain sample space. An improvement trend in the Sobol error is observed with larger sample sizes towards an asymptotic error of about 0.01-0.02 errors, depending on the surface location for monitoring deflection. Note that T1-T8 correspond to locations of the eight toroids tangentially aligned with the nose cap juncture and the shoulder. Convergence of the surrogate models were achieved at 60 samples, which represents a 60% reduction in the number of FSI evaluations, compared to point-collocation NIPC.

After the response surfaces are constructed for the deflection, probability box plots with lower and upper bounds of the cumulative distribution functions (CDF) are generated for the deflections with second-order probability using 400,000 samples. The probability box plots are shown in Figures 3.20-3.21 for three selected surface toroid locations (T1, T4, and T8). All probability box plots illustrate convergence of the response surfaces with the CDF bounds overlapping by 60 samples. The 95% confidence intervals are extracted from the probability box plots, which are measured as distance between the lower CDF bound the 2.5% probability level and the upper CDF bound of the 97.5% probability level. Figures 3.22 and 3.23 present the 95% confidence interval deflections of the HIAD, compared to the undeflected (initial) surface. For the baseline reference case, the deflection angle for the deflected surface corresponds to 5.34 deg. for the windward side and 0.44 deg. for the

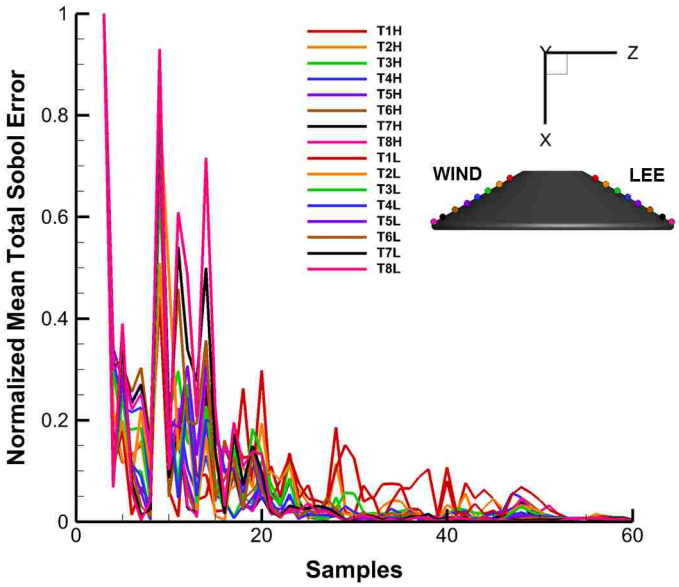

Figure 3.19. Normalized mean Sobol index error for a range of sample sizes

leeward side. The uncertainty of the deflection angle was determined to be much larger on the windward side with a 95% confidence interval of [4.74, 6.94] deg. compared to the leeward side with a 95% confidence interval of [0.34, 1.25] deg.

Compared to the ballistic entry uncertainty results [18], the asymmetric behavior of the deflections for lifting entry covers a much broader range. However, for both entry cases, the uncertainty behavior with respect to the baseline reference deflections are very similar. For example, notice the skewness of the uncertainty bounds of the deflections angles (e.g. 95% confidence interval bounds shown above) compared to the baseline reference deflection angle. The probability box plots for the deflections in Figure 3.21 (specifically, Figures 3.21(b) and 3.21(c)) further show this skewness behavior, as the lower 2.5% probability level at the lower bound is skewed towards the 50% (mean) level. A result of note is that the skewness uncertainty behavior of the deflection angle is caused by one of the uncertain input parameters because of the asymmetric uncertainty range of E_c.

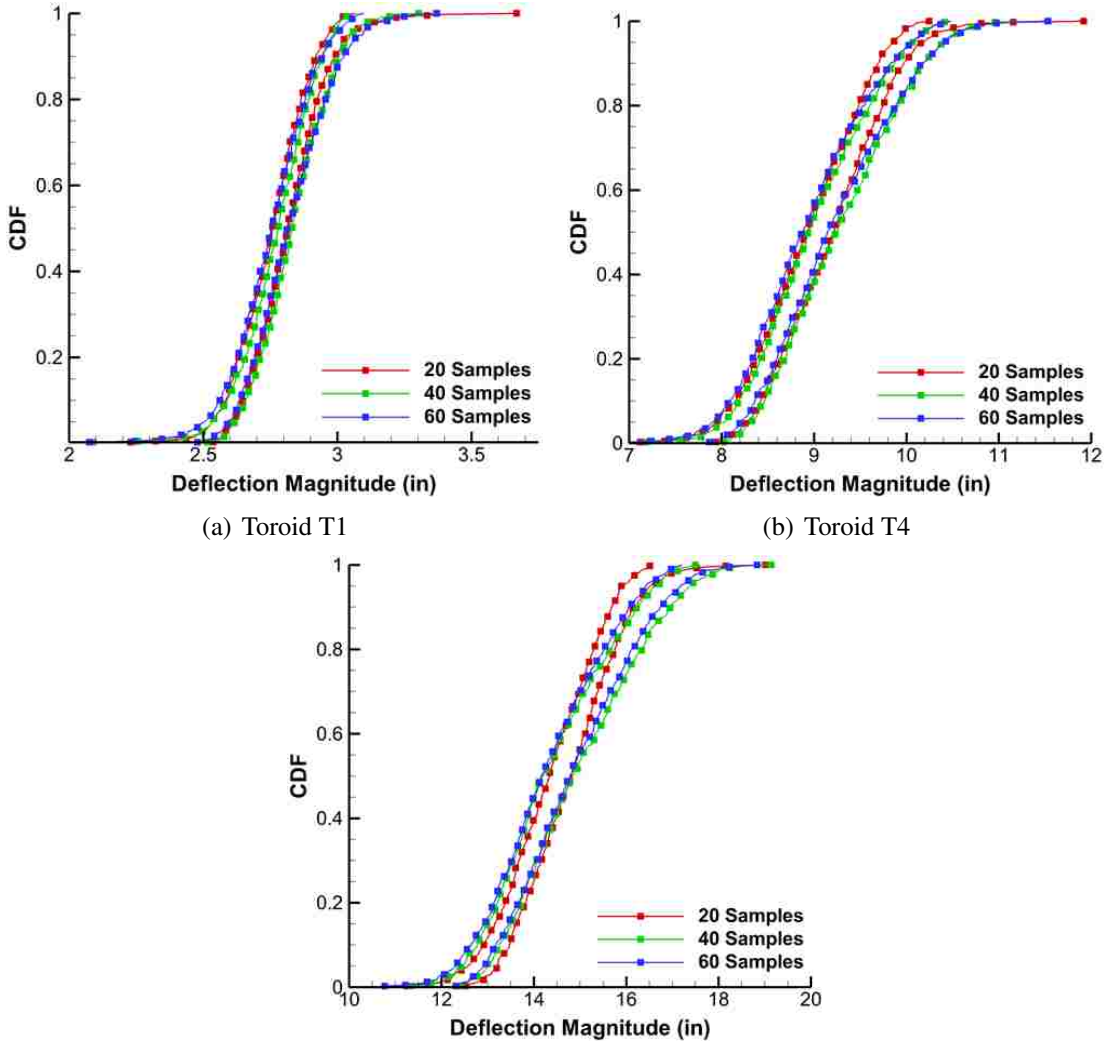

(a) Toroid T1

(b) Toroid T4

(c) Toroid T8

Figure 3.20. P-Box convergence for deflection at selected HIAD surface locations (windward)

Li [32] reports photogrammetry results for the 6m NFAC test article and presents deflection angles for a range of dynamic pressure (20-70 psf) and yaw angles (-10 to 25 deg.) at subsonic test conditions. The maximum deflection angle of all test runs was reported as 4.91 deg. The maximum deflection angles obtained in this study are significantly larger (approximately 7 deg.) compared to those reported at subsonic test conditions by Li

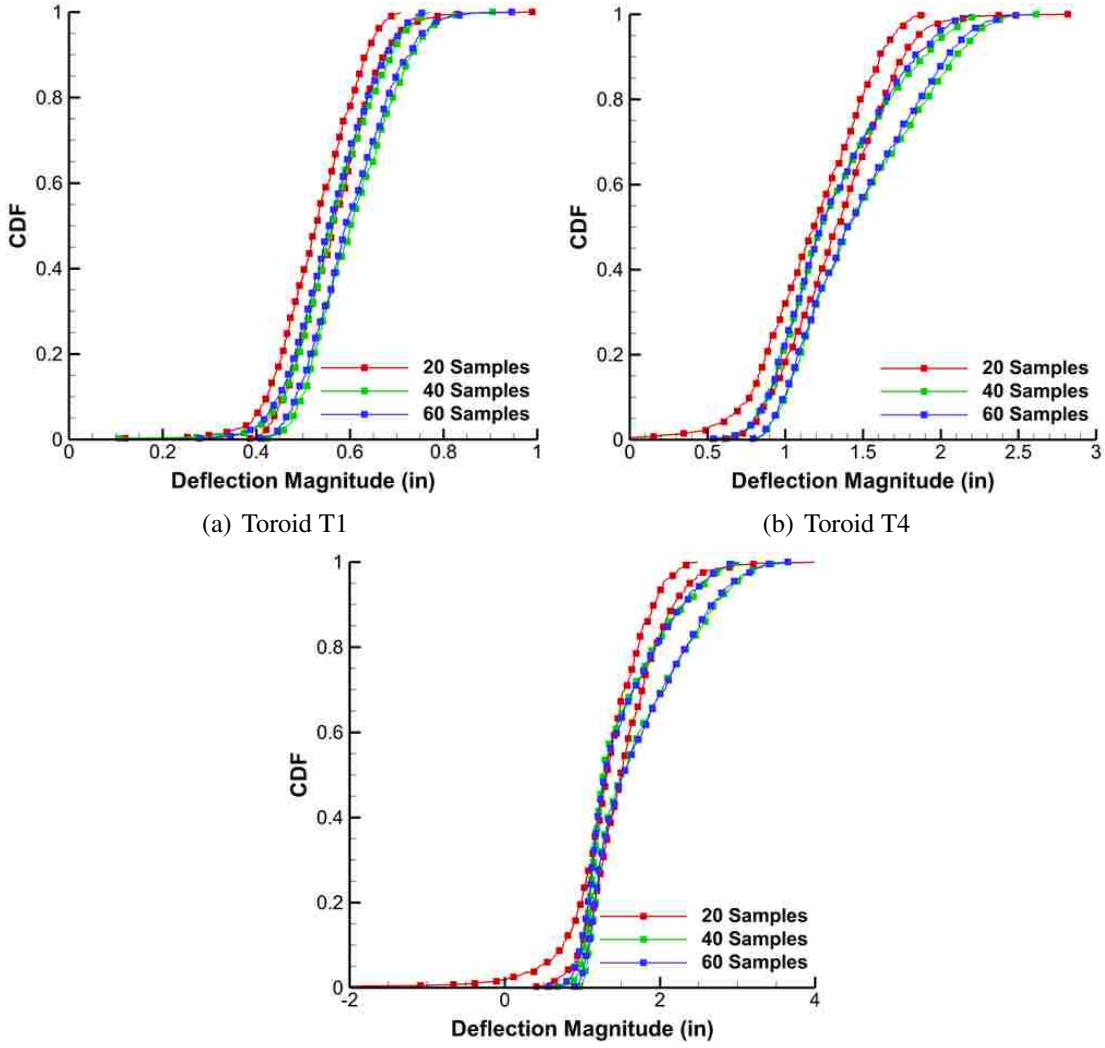

(a) Toroid T1

(b) Toroid T4

(c) Toroid T8

Figure 3.21. P-Box convergence for deflection at selected HIAD surface locations (leeward)

[32]. However, the surface pressures for all cases in this hypersonic study are up to four times the surface pressures observed for the NFAC wind tunnel test. As a result, the deflection results of the 95% confidence interval are shifted to higher values (due to hypersonic conditions) beyond the experimental deflection angles at subsonic conditions.

In Tables 3.8 and 3.9, the uncertain parameters that represent 90% contribution to the deflection uncertainty are listed based on global nonlinear variance-based sensitivity analysis (i.e., Sobol indices). The top three main contributors are highlighted in red (first), green (second), and blue (third). The tensile stiffness of the Technora axial cord (E_c) is the most significant contributor to the deflection uncertainty over the entire deformable surface. This top contributor has the largest uncertainty range compared to other tensile stiffnesses of the torus and straps. The asymmetric uncertainty range of E_c is proportionally reflected in the deflection uncertainty for both the lifting and ballistic entries. The uncertainty in the axial cord stiffness explains the skewness behavior of the deflection uncertainty (Figure 3.21). The torus tensile stiffnesses (E_L and E_T), Poisson ratio (ν_{LT}), and the inflation pressure (P_0) are important towards at nose cap conjunction while the 4-K strap tensile stiffness (E_{4K}) is important for the entire deformable region, especially towards the shoulder. This location-dependent behavior is primarily due to the fact that the 4-K straps carry/distribute loads from the shoulder to the nose cap centerbody while the inflation pressure and torus structure carry significant load near the nose cap. These observations were also made for the ballistic entry uncertainty analysis [18].

There is an additional uncertain parameter that becomes mroe significant for lifting entry. Because of the asymmetric loading of the HIAD for lifting entry, the torsional stiffness of the torus contributes up to 10% of the deflection uncertainty throughout the pitch plane. Furthermore, the asymmetric loading, and hence small deflection magnitudes on the leeward region compared to the windward side, show that some of the uncertain parameters are significant on the windward side, specifically the inflation pressure and one of the torus stiffnesses, and some uncertain parameters are insignificant on the leeward side.

Another point to emphasize is that the structural stiffnesses dominate the uncertainty in the deflection, which may be due to the large level of uncertainty combined with

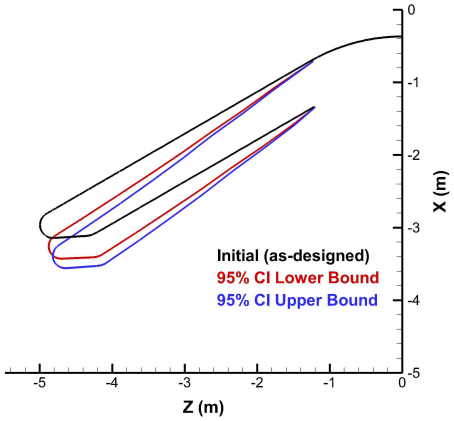

Figure 3.22. 95% confidence limits of the HIAD deflected surface (windward)

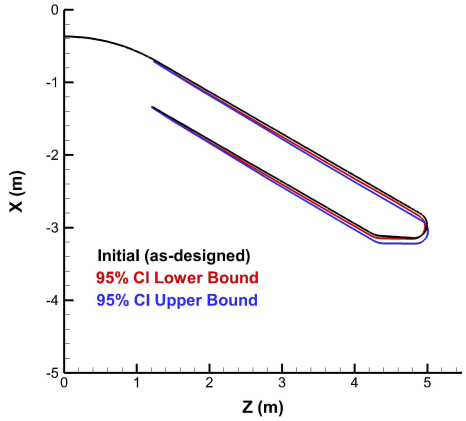

Figure 3.23. 95% confidence limits of the HIAD deflected surface (leeward)

the sensitivity of the deflection to these variables, compared to the surface pressure and shear stress (surface force) uncertainties. Therefore, the deflection uncertainty can be interpreted to be primarily dependent on structural input uncertainty. The flowfield and freestream uncertainties, however, are expected to be significant contributers to the uncertainty in the surface conditions in the presence of deflections. The question that now requires attention is how the deflection uncertainty (or the uncertainty in the shape deformation) affects the resulting surface conditions (i.e., surface heat flux, pressure, and shear stress) and aerodynamic performance.

3.5.2. Uncertainty Analyses of HIAD Surface Quantities and Aerodynamic Performance. With two FSI cycles already completed with converged surface conditions, the sparse approximation UQ approach was implemented to generate the response surfaces for heat flux, pressure, and shear stress at the same sixteen HIAD surface locations (T1-T8 on both windward and leeward sides). Additional points (T9-T14) were added around the shoulder torus to capture the pressure, shear stress, and heat flux behavior on both

Table 3.8. Uncertain parameter contributions to the HIAD deflection uncertainty (windward)

Uncertain Param.	T1	T2	T3	T4	T5	T6	T7	T8
E_c	35.2%	49.4%	63.5%	70.8%	73.0%	73.3%	74.3%	73.3%
E_{4K}	24.0%	16.4%	11.9%	9.3%	10.6%	11.5%	12.1%	13.5%
G_{LT}	6.9%	9.4%	9.5%	8.3%	7.6%	6.9%	6.8%	6.6%
E_T	6.0%	3.5%	2.2%	1.3%				
P_0	5.8%	4.9%	1.6%	1.2%	1.1%	1.1%		
ν_{LT}	5.8%	3.8%	2.2%	1.3%				
E_L	3.8%	2.1%	1.4%	1.1%	1.2%	1.0%		

Table 3.9. Uncertain parameter contributions to the HIAD deflection uncertainty (leeward)

Uncertain Param.	T1	T2	T3	T4	T5	T6	T7	T8
E_c	65.6%	77.6%	86.1%	87.8%	88.9%	89.5%	89.5%	89.7%
E_{4K}	8.8%	6.5%	4.0%	3.1%	2.8%	2.5%	2.6%	2.6%
G_{LT}	6.7%	5.0%	4.8%	5.3%	5.3%	5.5%	5.9%	5.8%
ν_{LT}	6.0%	4.4%	2.4%					
E_T	5.8%	1.3%						

sides of the pitch plane. Convergence of the polynomial expansion coefficients again was obtained by 60 samples for all surface locations at approximately 0.01-0.02 mean Sobol errors. 400,000 samples were used to construct the probability box plots from the response surfaces generated at each surface location. Global nonlinear sensitivity analysis of the surface conditions are reported for three selected locations in Figure 3.24.

Figure 3.25 presents the 95% confidence levels of the surface pressure, shear stress, and heat flux in the leeward and windward deformable regions of the HIAD pitch plane. The undeformed forebody surface of the HIAD is plotted for reference (not to scale). The baseline reference surface pressure, shear stress, and heat flux are also plotted in comparison with the confidence levels. The surface pressure in the deformable region (Fig-

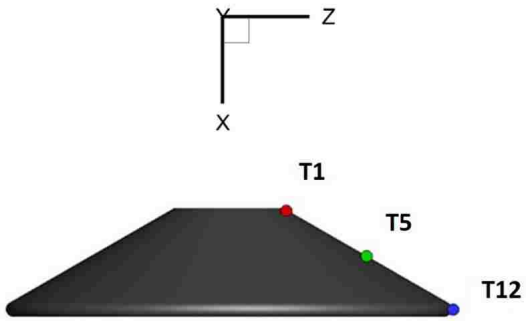

Figure 3.24. HIAD surface locations for reporting contributions to pressure, shear stress, and convective heating

ure 3.25(a)) is fairly uniform until the expansion around the shoulder torus. The windward side, however, experiences much higher pressures (about 30% more) compared to the leeward side. The uncertainty in the pressure indicates as much as 30% deviation from the baseline reference pressure due to the uncertainty in the flowfield and deflection uncertainties. Figures 3.25(b) and 3.25(c) show augmented levels of shear stress and heat flux, signaling turbulent boundary layer behavior past the sphere-cone juncture in the leeward deformable region. Because of the uncertainty in the flowfield and deflection of the HIAD, the shear stress and heat flux exhibit significant uncertainty from the baseline reference level (as much as 25-30%).

Figures 3.26-3.27 summarize the contributions of the flowfield and deflection (δ) uncertainty to the surface pressure, shear stress, and heat flux uncertainty at three selected locations of the HIAD surface in Figure 3.24. Tables 3.8 and 3.9 showed that the deflection uncertainty was strongly dependent on only structural parameter uncertainties (i.e., stiffnesses of the cords, torus, and straps, and inflation pressure). The deflection uncertainty contributions (δ) reported in Figures 3.26-3.27 can, therefore, be thought as a summation of the Sobol indices of the structural parameters in Tables 3.8 and 3.9. The freestream den-

sity is the most significant contributor (over 90%) to the surface pressure uncertainty in the flank region of the HIAD while the deflection uncertainty accounts for approximately 5% (Figure 3.26(a)). Because there is little deflection in the leeward deformable region (Figure 3.27(a)), the deflection uncertainty contribution to the pressure uncertainty diminishes to less than 1% with only the freestream density as the sole contributor, which is a similar finding to the rigid HIAD uncertainty results obtained in a previous study [17].

In Figures 3.26(b) and 3.27(b), the freestream density and CO_2-CO_2 interaction are the main contributors to the shear stress uncertainty, accounting for 95% of the uncertainty. For turbulent boundary layer flows, these two flowfield uncertain parameters were shown to be significant in the flank and shoulder region in a previous study by the authors [17], as the CO_2-CO_2 binary interaction affects the transport properties and the density influences the Reynolds number and the turbulent (eddy) viscosity. The freestream velocity and deflection contribute slightly to the shear stress uncertainty.

For the heat flux uncertainty in Figures 3.26(c) and 3.27(c), the freestream density, again, is the top contributor by a significant amount. Shape deformation (or deflection) uncertainty accounts for approximately 10% of the uncertainty in the heat flux in the windward deformable region and diminishes in contribution in the leeward deformable region. Slight contributions to the heat flux uncertainty arise due to the CO_2-CO_2 interaction and freestream velocity. Again, similar results were concluded in a previous study by the authors [17] with the addition of deflection uncertainty in this work.

The pressure uncertainty is further reflected in the aerodynamic performance uncertainty of the HIAD. Table 3.10 presents the nominal and 95% confidence interval for C_D and L/D for lifting entry. The C_D uncertainty varies as much as 30 drag counts, and L/D has as much as 4% uncertainty from the respective nominal values. Because the surface pressure primarily affects the aerodynamics, the main contributors to the pressure uncertainty

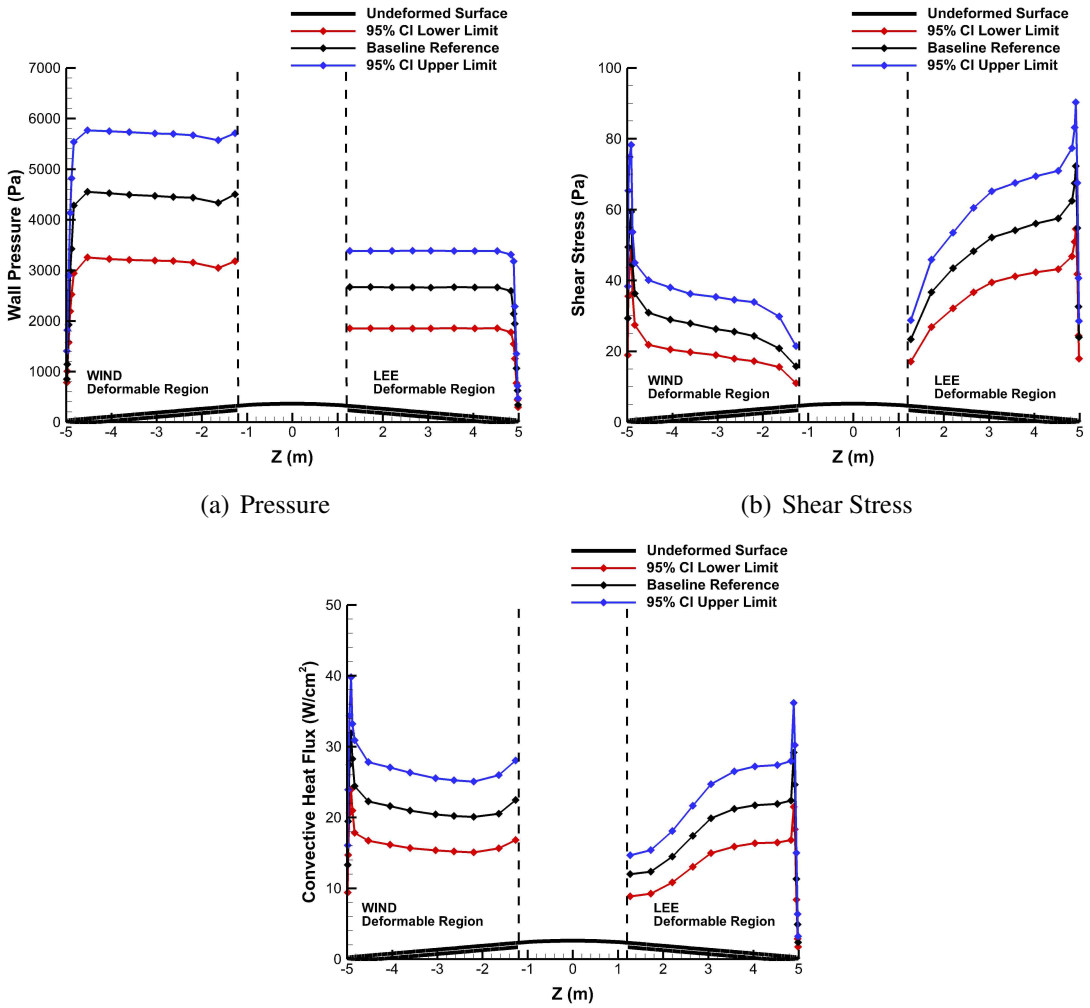

(a) Pressure

(b) Shear Stress

(c) Heating Rate

Figure 3.25. 95% confidence interval and baseline reference distributions for the surface conditions along the HIAD pitch plane

(i.e., freestream density and deflection uncertainty) are proportionally reflected in the C_D and L/D uncertainties.

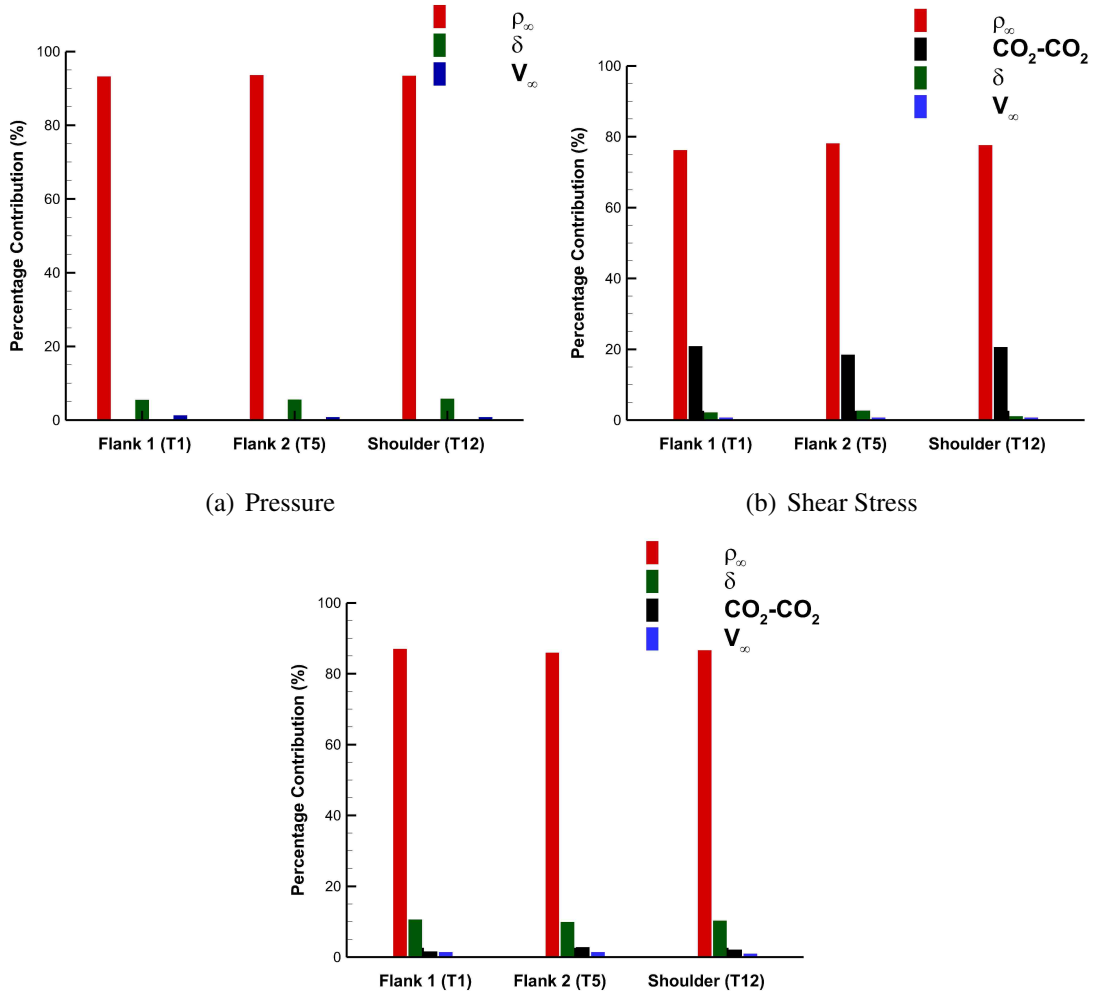

(a) Pressure

(b) Shear Stress

(c) Heating Rate

Figure 3.26. Uncertain parameter contributions to the surface condition uncertainty (windward region)

Table 3.10. Uncertainty in the aerodynamic performance of the HIAD for lifting entry

Parameter	Nominal	95% Confidence Interval
C_D	1.394	[1.367, 1.411]
L/D	0.150	[0.145, 0.156]

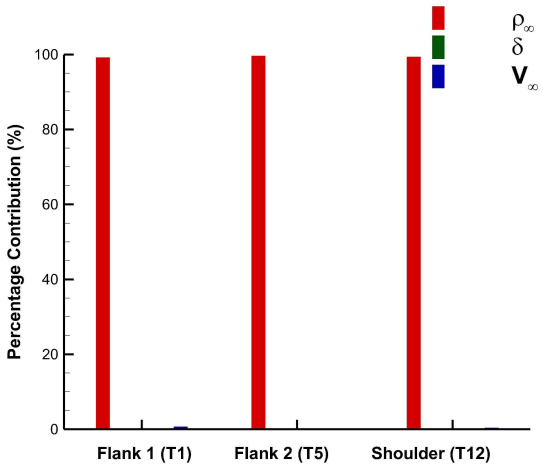

(a) Pressure

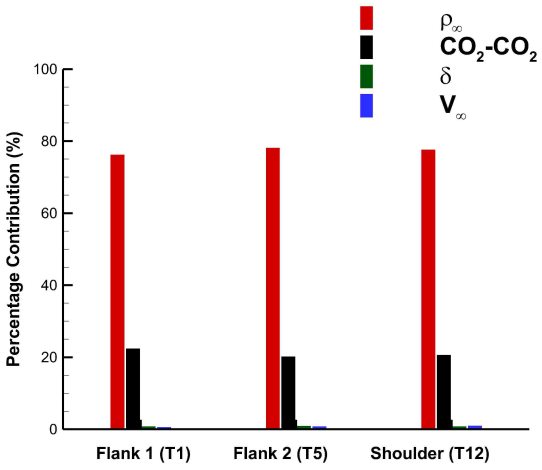

(b) Shear Stress

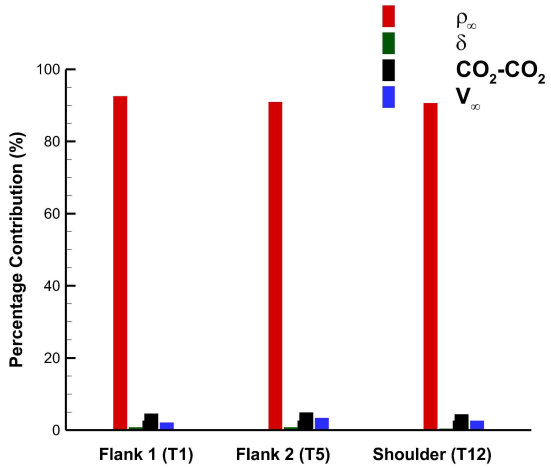

(c) Heating Rate

Figure 3.27. Uncertain parameter contributions to the surface condition uncertainty (leeward region)

4. CONCLUDING REMARKS

The primary focus of this paper is to present a detailed uncertainty analysis for prediction of the deformation and the resulting surface conditions of a Hypersonic Inflatable Aerodynamic Decelerator configuration due to freestream variations and uncertainties in structural and flowfield physical modeling parameters. The decelerator is defined to be a stack of eight tori that form a 60-deg half angle cone. The innermost torus is attached to a rigid nose cap. A high-fidelity, loosely-coupled approach was presented for static fluid-structure interaction simulations using the FUN3D flow solver and the NASTRAN structural solver. A sparse approximation approach for nonintrusive polynomial chaos was applied to quantify the uncertainty of the inflatable decelerator deformation and surface conditions in the presence of the aforementioned uncertain parameters at peak heating conditions for a reference lifting Mars entry trajectory. Results were compared to those obtained in a previous study for ballistic Mars entry.

Uncertainties in the deflection of the inflatable decelerator were first quantified using 16 uncertain parameters associated with the structural and flowfield modeling. Uncertainty analysis showed that the deflection angle can vary by as much as 2.2 degrees with a 95% confidence interval of [4.74, 6.94] deg. on the windward side of the pitch plane and approximately 1 deg. 95% confidence interval of [0.34, 1.25] deg. on the leeward side of the pitch plane. Global nonlinear sensitivity analysis was used to identify and rank the important parameters that contribute most to the uncertainty in the deflection. The tensile stiffness of the axial cords was the top contributor for the entire deformable surface. The inflation pressure and torus tensile stiffnesses were important near the nose cap juncture while the 4000-lb radial strap tensile stiffnesses were significant throughout the deformable re-

gion (both leeward and windward), especially towards the shoulder torus. These main contributors to the deflection uncertainty were also found for uncertainty analysis for ballistic Mars entry at peak heating. However, for lifting Mars entry at peak heating, the torsional stiffness of the torus was shown to be significant because of the asymmetric loading experienced externally by the inflatable decelerator. Most of the deflection uncertainty was concluded as dependent on only the structural parameters. Therefore, the deflection uncertainty can be interpreted as the summation of the top contributing structural uncertainties when analyzing the uncertainty in the surface conditions.

The deflection uncertainty was applied to the uncertainty analysis of the resulting surface conditions (i.e., surface pressure, shear stress, and heat flux). Uncertainty analysis showed that the pressure, shear stress, and heat flux vary significantly in the deformable region under the uncertainty sources considered. Slight importance of the deflection uncertainty was observed for the shear stress uncertainties with increased significance for the surface pressure and heat flux uncertainty (as much as 10%) on the windward side of the pitch plane. On the leeward side, the effect of deflection uncertainty is reduced to less than 1% due to small deflections in this region. The freestream density was the top contributor for surface pressure, shear stress, and heat flux for the entire deformable region. The CO_2-CO_2 binary collision interaction was also significant contributor to the shear stress and heat flux uncertainty due to its influence in the transport properties of the flow near the surface. The relative ranking of the uncertainty sources are similar to ballistic Mars entry at peak heating. The main contributors to the deflection and surface condition uncertainties that were identified in this work are expected to help narrow the focus on future work to improve the reliability and robustness of the inflatable decelerator design.

ACKNOWLEDGMENTS

This work was supported by a NASA Space Technology Research Fellowship under training project grant no. NNX13AL58H (Serhat Hosder, principal investigator and Karl Edquist, research collaborator). The authors would like to thank Mike Lindell and Robert Biedron from NASA Langley Research Center for providing guidance and technical support for the coupled fluid-structure modeling process and providing necessary data to make this work possible.

BIBLIOGRAPHY

[1] Zang, T. A., Dwyer-Ciancolo, A. M., Kinney, D. J., R.Howard, A., Chen, G. T., Ivanov, M. C., Sostaric, R. R., and Westhelle, M. C., "Overview of the NASA Entry, Descent, and Landing Systems Analysis Studies for Large Robotic-class Missions, AIAA 2010-8649," *AIAA SPACE 2010 Conference and Exhibition*, Anaheim, CA, Aug. 2010.

[2] Dwyer-Ciancolo, A. M., Davis, J. L., Shidner, J. D., and Powell, R. W., "Entry, Descent, and Landing Systems Analysis: Exploration Class Simulation Overview and Results," *AIAA/AAS Astrodynamics Specialist Conference*, Toronto, Ontario Canada, Aug. 2010.

[3] Dwyer-Ciancolo, A. M., Davis, J. L., Engelund, W. C., Komar, D. R., Queen, E. M., Samareh, J. A., Way, D. W., and Zang, T. A., "Entry, Descent, and Landing Systems Analysis Study: Phase 2 Report on Exploration Feed-Forward Systems," Tech. rep., NASA/TM-217055, Feb. 2011.

[4] Drake, B. G., "Human Exploration of Mars Design Reference Architecture 5.0," Tech. rep., NASA-SP-2009-566, 2009.

[5] Tanner, C. L., *Aeroelastic Analysis and Testing of Supersonic Inflatable Aerodyamics Decelerators*, Ph.D. thesis, Georgia Institute of Technology, May 2012.

[6] Swanson, G., Cassell, A. M., Johnson, R. K., Hughes, S. J., Calomino, A. M., and Cheatwood, F. M., "Structural Strap Tension Measurements of a 6-meter Hypersonic Inflatable Aerodynamic Decelerator under Static and Dynamic Loading, AIAA 2013-1287," March 2013.

[7] Cassell, A. M., Swanson, G. T., Quach, B. T., Kushner, L. K., Brown, J. D., Kazemba, C. D., Kruger, C. E., Li, L., Johnson, R. K., Hughes, S. J., Calomino, A. M., and Cheatwood, F. M., "Design and Execution of the Hypersonic Inflatable Aerodynamic Decelerator Large-Article Wind Tunnel Experiment, AIAA 2013-1304," *AIAA Aerodynamic Decelerator Systems Conference*, Daytona Beach, FL, March 2013.

[8] Hughes, S. J., Cheatwood, F. M., Dillman, R. A., Wright, H. S., et al., "Hypersonic Inflatable Aerodynamic Decelerator (HIAD) Technology Development Overview, AIAA 2011-2524," *AIAA Aerodynamic Decelerator Systems Technology Conference and Seminar*, Dublin, Ireland, May 2011.

[9] Hosder, S. and Bettis, B., "Uncertainty and Sensitivity Analysis for Reentry Flows with Inherent and Model-Form Uncertainties," *Journal of Spacecraft and Rockets*, Vol. 49, No. 2, 2012, pp. 193–206.

[10] Bettis, B., Hosder, S., and Winter, T., "Efficient Uncertainty Quantification in Multi-disciplinary Analysis of a Reusable Launch Vehicle, AIAA 2011-2393," *17th AIAA International Space Planes and Hypersonic Systems and Technologies Conference*, San Francisco, CA, 2011.

[11] Hosder, S., Walters, R. W., and Balch, M., "Efficient Sampling for Non-Intrusive Polynomial Chaos Applications with Multiple Uncertain Input Variables, AIAA 2007-1939," *48th AIAA/ASME/ASCE/AHS/ASC Structures, Structural Dynamics, and Materials Conference*, Honolulu, HI, April 2007.

[12] Hosder, S., Walters, R. W., and Balch, M., "Point-Collocation Nonintrusive Polynomial Chaos Method for Stochastic Computational Fluid Dynamics," *AIAA Journal*, Vol. 48, No. 12, 2010, pp. 2721–2730.

[13] Walters, R. W. and Huyse, L., "Uncertainty Analysis for Fluid Mechanics with Applications," Tech. rep., ICASE 2002-1, NASA/CR-2002-211449, NASA Langley Research Center, Hampton, VA, 2002.

[14] Eldred, M. S., "Recent Advances in Non-Intrusive Polynomial Chaos and Stochastic Collocation Methods for Uncertainty Analysis and Design, AIAA 2009-2274," 50^{th} *AIAA/ASME/ASCE/AHS/ASC Structures*, Palm Springs, CA, May 2009.

[15] West IV, T. K., Hosder, S., and Johnston, C. O., "A Multi-Step Uncertainty Quantification Approach Applied to Hypersonic Reentry Flows, AIAA 2011-2524," 51^{st} *AIAA Aerospace Sciences Meeting*, Grapevine, TX, Jan. 2013.

[16] West IV, T. K., Hosder, S., and Johnston, C. O., "Uncertainty Quantification of Hypersonic Reentry Flows using Sparse Sample and Stochastic Expansions," *AIAA Journal of Spacecraft and Rockets*, Vol. 52, No. 1, Jan. 2015, pp. 120–133.

[17] Brune, A. J., West, T., Hosder, S., and Edquist, K. T., "Uncertainty Analysis of Mars Entry Flows over Hypersonic Inflatable Aerodynamic Decelerators," *AIAA Journal of Spacecraft and Rockets*, Vol. 52, No. 3, 2015, pp. 776–788.

[18] Brune, A. J., Hosder, S., and Edquist, K. T., "Uncertainty Analysis of Fluid-Structure Interaction of a Deformable Hypersonic Inflatable Aerodynamic Decelerator, AIAA 2015-3581," *20th AIAA International Space Planes and Hypersonic Systems and Technologies Conference*, Glasgow, Scotland, 2015.

[19] Witteveen, J. A. S. and Bijl, H., "Efficient Quantification of the Effect of Uncertainties in Advection Diffusion Problems Using Polynomial Chaos," *Numerical Heat Transfer*, Vol. 53, No. 5, 2008, pp. 437–465.

[20] Han, D. and Hosder, S., "Inherent and Model-Form Uncertainty Analysis for CFD Simulation of Synthetic Jet Actuators, AIAA 2012-0082," 48^{th} *AIAA Aerospace Sciences Meeting*, Nashville, TN, Jan. 2012.

[21] Asif, M. S. and Romberg, J., "Fast and Accurate Algorithms for Re-Weighted l1-Norm Minimization," *IEEE Transactions on Signal Processing*, Vol. 61, No. 23, 2013, pp. 4905–4916.

[22] Doostan, A. and Owhadi, H., "A non-adapted sparse approximation of PDEs with stochastic inputs," *Journal of Computational Physics*, Vol. 230, No. 8, 2011, pp. 3015–3034.

[23] Yang, A., Ganesh, A., Sastry, S., and Ma, Y., "Fast L1-Minimization Algorithms and An Application in Robust Face Recognition: A Review," Tech. rep., Tech. Rep. UCB/EECS-2010-13, Feb. 2010.

[24] Sudret, B., "Global sensitivity analysis using polynomial chaos expansion," *Reliability Engineering and System Safety*, Vol. 93, No. 7, 2008, pp. 964–979.

[25] Crestaux, T., Maitre, O. L., and Martinez, J.-M., "Polynomial chaos expansion for sensitivity analysis," *Reliability Engineering and System Safety*, 2009.

[26] Biedron, R. T., Derlaga, J. M., Gnoffo, P. A., Hammond, D. P., et al., "FUN3D Manual: 12.4," Tech. rep., NASA/TM-2014-218179, March 2014.

[27] "Turbulence Modeling Resource," http://turbmodels.larc.nasa.gov/spalart.html, Accessed: 2016-2-23.

[28] Catris, S. and Aupoix, B., "Density Corrections for Turbulence Models," *Aerospace Science and Technology*, Vol. 4, 2000, pp. 1–11.

[29] Yee, H., Sandham, N., and Djomehri, M., "Low Dissipative High Order Shock-Capturing Methods Using Characteristic-Based Filters," *Journal of Computational Physics*, Vol. 150, No. 1, 1999, pp. 199–238.

[30] MSC, "MSC Nastran 2013.1.1 Release Guide," Tech. rep., MSC/DOC-10524, March 2014.

[31] Samareh, J. A., "Discrete Data Transfer Technique for Fluid-Structure Interaction, AIAA 2007-4309," *18th AIAA Computational fluid Dynamics Conference*, Miami, FL, 2007.

[32] Li, L., Braun, R. D., and Cassell, A. M., "Photogrammetry Analysis of a Hypersonic Inflatable Aerodynamic Decelerator Structural Test Article, AIAA 2014-0353," Jan. 2014.

[33] Lichodziejewski, L., Tutt, B., Jurewicz, J., Dillman, R., Johnson, K., and Cassell, A. M., "Ground and Flight Testing of a Stacked Tori Hypersonic Inflatable Aerodynamic Decelerator Configuration, AIAA 2013-1864," April 2013.

[34] Cruz, J. R. and Munk., M. M., "Introduction to Trajectories," Presented at the 10th International Planetary Probe Workshop, San Jose, CA, 2013.

[35] Wright, M. J., Hwang, H. H., and Schwenke, D. W., "Recommended Collision Integrals for Transport Property Computations Part II: Mars and Venus Entries," *AIAA Journal*, Vol. 45, No. 1, 2007, pp. 281–288.

[36] Bettis, B. and Hosder, S., "Uncertainty Quantification in Hypersonic Reentry Flows Due to Aleatory and Epistemic Uncertainties, AIAA 2011-252," *49th AIAA Aerospace Sciences Meeting including New Horizons Forum and Aerospace Exposition*, Orlando, FL, Jan. 2011.

[37] Bose, D. and Wright, M., "Uncertainty Analysis of Laminar Aeroheating Predictions for Mars Entries," *AIAA/AAS Astrodynamics Specialist Conference*, Toronto, Ontario Canada, Aug. 2010.

[38] Gupta, R. N., Yos, J. M., Thompson, R. A., and Lee, K. P., "A Review of Reaction Rates and Thermodynamic and Transport Properties for an 11-Species Air Model for Chemical and Thermal Nonequilibrium Calculations to 30000 K," Tech. rep., NASA/RP-1232, Aug. 1990.

[39] Wright, M., Tang, C. Y., Edquist, K. T., Hollis, B. R., Krasa, P., and Campbell, C. A., "A Review of Aerothermal Modeling for Mars Entry Missions, AIAA 2010-0443," 48^{th} *AIAA Aerospace Sciences Meeting*, Orlando, FL, Jan. 2010.

III. THERMAL PROTECTION SYSTEM RESPONSE UNCERTAINTY OF A HYPERSONIC INFLATABLE AERODYNAMIC DECELERATOR

Andrew J. Brune **Serhat Hosder**

Missouri University of Science and Technology, Rolla, MO, 65409

Karl T. Edquist **Steven A. Tobin**

NASA Langley Research Center, Hampton, Virginia 23681

ABSTRACT

The objective of this paper is to investigate the uncertainty in the bondline temperature response of a flexible thermal protection system subject to uncertain parameters in the hypersonic flowfield and thermal response modeling of a Hypersonic Inflatable Aerodynamic Decelerator configuration for ballistic Mars entry. A global nonlinear sensitivity analysis study for the bondline temperature uncertainty shows that the dimension of uncertain parameters can reduced from 22 to eight. Uncertainty analysis of the bondline temperature in the reduced dimensions indicates that the bondline temperature varies by as much as 125% above the nominal prediction and exceeds the temperature limit of 400 ^{o}C. The largest uncertainty occurs at 70 seconds in the trajectory prior to separation of the inflatable decelerator for transition to a secondary descent technology. The main contributors to the bondline temperature uncertainty are the insulator and outer fabric thermal conductivities and the freestream density. The thickness and initial density of the insulator layer, closest to the gas barrier layer, are also shown to be a significant contributor to the bondline temperature uncertainty, especially earlier in the trajectory.

NOMENCLATURE

CoV	Coefficient of Variation	T	Temperature (K or ^{o}C)
C_H	Heat Transfer Coefficient based on Enthalpy Difference (kg/m^2-s)	v_{gx}	Porous Gas Velocity (m/s)
		q	Surface Heat Flux (W/m^2)
C_{ps}	Specific Heat of the Solid Material (J/kg-K)	u_e	Boundary Layer Edge Velocity (m/s)
		w	Wall Condition
C_{pg}	Specific Heat of the Gas Mixture (J/kg-K)	α	Deterministic Coefficient in the Polynomial Chaos Expansion
f_1, f_2	Temperature-Dependent Curve Fits	α^*	Generic Uncertain Response Function
H_{0e}	Total Enthalpy at the Boundary Layer Edge (J/kg)	δ	Truncation Error
		ε	Emissivity of the Outer Fabric Material
H_d	Bulk Heat of Reaction (J/kg)	μ_e	Mean Error
k	Effective Material Conductivity (W/m-K)	μ_g	Viscosity of the Gas Mixture (Pa-s)
		ξ	Standard Input Random Variable
k_x	Solid Material Permeability (m^2)	ρ_e	Boundary Layer Edge Density (kg/m^3)
n	Number of Random Dimensions	ρ_g	Gas Density (kg/m^3)
N_s	Number of Samples	ρ_s	Solid Density (kg/m^3)
N_t	Number of Terms in a Total-Order Polynomial Chaos Expansion	σ	Stefan-Boltzmann Constant (5.6703 x 10^{-8} J/m^2-s-K^4)
p	Order of Polynomial Expansion	ϕ	Porosity
S_e	Percent Absolute Error	Ψ	Random Basis Function
S_T	Total Sobol Index	$\Omega^{1,1}$	Diffusion Collision Integral
S_t	Stanton Number based on Boundary Layer Edge Conditions	$\Omega^{2,2}$	Viscosity Collision Integral
		∞	Freestream Condition

1. INTRODUCTION

NASA continues to bridge the gap between current metric-ton class robotic missions and large robotic and human explorations missions with 20-50 metric-ton payloads. In an effort to identify the most viable investment path beyond the Mars Design Reference Architecture [1] study, recent work, such as the Entry, Descent, and Landing System Analysis [2, 3, 4] (EDL-SA), have been tasked to evaluate vehicle concepts and technological investments required to enable human and large-scale payload missions to Mars. Architecture-level assessments of these studies have shown that it is impossible to safely land systems with heritage EDL systems that have been used to date. Multiple deceleration concepts were identified to meet enhanced payload capability. A Hypersonic Inflatable Aerodynamic Decelerator (HIAD) has been considered to be a viable candidate to replace the traditional rigid aeroshell [5]. The inflatable heatshield is packed and stowed to fit within the current launch vehicle sizes and deployed prior to atmospheric entry, resulting in a heatshield size much larger than the stowed diameter. Therefore, the HIAD provides the advantage of increased payload capability or high-altitude deceleration for pinpoint landing. Due to the high heat loads encountered in atmospheric entry environments, the inflatable aeroshell system relies on a flexible TPS to prevent the underlying inflatable structure (i.e., stacked toroids bonded with a network of straps) from exceeding its thermal limits.

The HIAD technology development project at NASA has undergone extensive aerothermal arc jet testing of candidate flexible TPS materials and layups at stagnation conditions to evaluate thermal performance and provide boundary condition and in-depth measurement data for thermal model correlation and validation [6, 7]. Accurate prediction of the thermal

response of the flexible TPS exposed to high aerothermal and mechanical loads presents a challenge in the presence of uncertainties associated with the high-fidelity models used. Therefore, it is important to identify the key factors that impact the thermal response of the TPS, specifically the bond line temperature, to ensure that it is maintained at or below the maximum allowable temperature of the gas barrier and/or underlying inflatable structure.

Efficient uncertainty quantification (UQ) methods have become the preferred approach over traditional sampling techniques, such as Monte Carlo. Traditional methods may be infeasible because of the significant computational cost of high-fidelity numerical simulations for large-scale problems in planetary entry flows and TPS response. Previous works, such as Bettis and Hosder [8, 9] and Hosder et al. [10, 11], have investigated the practical use of stochastic expansions based on non-intrusive polynomial chaos (NIPC) for efficient UQ, which include propagation of both aleatory (inherent) and model-form (epistemic) uncertainties. The theory behind the NIPC is well-defined in the literature [12, 13] and provides a reliable method for UQ in complex aerospace simulations. West and Hosder [14] extended this work by demonstrating a multi-step NIPC UQ approach for quantifying the top contributing uncertainties to shock-layer radiation. Furthermore, West and Hosder [15] developed a sparse approximation NIPC technique to reduce the computational cost for UQ by utilizing a reduced set of samples to achieve accurate uncertainty results compared to the original NIPC technique. This work will use these approaches to minimize the number of computationally expensive model evaluations needed for an accurate UQ analysis.

In previous work by the authors [16], uncertainty analysis was performed over a rigid HIAD-like shape subject to a large number of mixed uncertainties, which included aleatory (inherent) uncertainties in the operating (freestream) conditions and epistemic uncertainties in the binary collision interaction and chemical reaction rate modeling of the

chemically-reacting flowfield. The uncertainties in the surface conditions (heat flux, pressure, and shear stress) were quantified, and the most significant uncertain parameters were identified based on global nonlinear sensitivity analysis to relatively rank the uncertainty sources. The information obtained from this previous study is used in the current work.

The primary objective of this work is to investigate the uncertainty in the high-fidelity flexible TPS (F-TPS) thermal response predictions, specifically the bond line temperature near the gas barrier layer, of a HIAD geometry for ballistic Mars entry defined by the EFF4 architecture in the EDL-SA study [4]. Efficient uncertainty quantification for various output quantities of interest is performed with the stochastic response methods, which were also used in previous studies involving hypersonic chemically reacting flows [15, 16, 17]. A high-fidelity computational fluid dynamics solver (CFD) is used to model thermochemical non-equilibrium flow. The surface pressure and aerodynamic heating information are applied as boundary condition input for the F-TPS in-depth thermal response solver. Significant flowfield uncertainty sources (binary collision interactions and freestream conditions) that contribute to the surface pressure and aerodynamic heating uncertainties identified in a previous work [16] are used in this study. Uncertainty sources in the TPS thermal model introduced in this study include material properties, thicknesses, and decomposition phenomena. A global non-linear sensitivity analysis is first performed to identify the important uncertain variables. Uncertainty quantification is then performed in the reduced dimensions with important uncertain variables.

The following section briefly outlines the response surface modeling approach used in the uncertainty analysis. Section 3 describes the baseline model for the HIAD EFF4 Mars entry scenario. Details regarding the CFD model, F-TPS response model, and nominal trajectory are given in this section. Section 4 presents the results for the baseline solution, uncertainty in the aerodynamic heating and pressure conditions for input to the F-TPS thermal model, and uncertainty in the F-TPS bond line temperature. Section 5 gives the important conclusions of this study.

2. UNCERTAINTY QUANTIFICATION METHODOLOGY

This section provides the details of the polynomial chaos techniques used in this study. The general non-intrusive polynomial chaos formulation with the point-collocation approach and sparse approximation approach are briefly discussed. A brief summary of dimension reduction based on sensitivity analysis is also provided.

2.1. POLYNOMIAL CHAOS THEORY

In recent studies [8, 9, 11, 18, 19], the polynomial chaos method has been used as a means of UQ over traditional methods, such as Monte Carlo, for computational efficiency. Polynomial chaos is a surrogate modeling technique based on a spectral representation of the uncertainty. An important aspect of spectral representation of uncertainty is that a response value or random function α^* (such as surface heat flux or TPS in-depth temperature at a particular surface location and given time instant) can be approximated as a series with each term decomposed into separable deterministic and stochastic components, as shown in Eq. (2.1).

$$\alpha^*(\mathbf{x},\xi) \approx \sum_{i=0}^{P} \alpha_i(\mathbf{x})\Psi_i(\xi) \tag{2.1}$$

Here, α_i is the deterministic component and Ψ_i are the random variable basis functions corresponding to the i^{th} mode. α^* is assumed to be a function of the deterministic variable vector $\mathbf{x}$ and the n-dimensional standard random variable vector ξ. By definition, this series is infinite; however, it can be truncated with a discrete sum over a number of output modes [13]. To form a complete basis or a total order expansion, the truncated series

can be represented with N_t number of terms, which will depend on the polynomial chaos expansion (PCE) of order p and the number of random variables, n:

$$N_t = P + 1 = \frac{(n+p)!}{n!p!} \tag{2.2}$$

Further details on polynomial chaos theory are given by Walters and Huyse [12] as well as Eldred [13].

To determine the expansion coefficients, α_i, without any modifications to the deterministic code (i.e., CFD code), several non-intrusive polynomial chaos (NIPC) methods have been developed. Of these, the point-collocation NIPC method has been used extensively in many aerospace simulations and CFD problems [9, 11, 19, 14]. The point-collocation method starts with replacing a stochastic response or random function with its PCE using Eq. (2.1). Then, N_t vectors are chosen in random space, and the deterministic code is then evaluated at these points to represent the left hand side of Eq. (2.1). Following this, a linear system of N_t equations can be formulated and solved for the spectral modes of the random variables, shown in Eq. (2.3).

$$\begin{pmatrix} \alpha^*(\mathbf{x},\xi_0) \\ \alpha^*(\mathbf{x},\xi_1) \\ \vdots \\ \alpha^*(\mathbf{x},\xi_P) \end{pmatrix} = \begin{pmatrix} \Psi_0(\xi_0) & \Psi_1(\xi_0) & \cdots & \Psi_P(\xi_0) \\ \Psi_0(\xi_1) & \Psi_1(\xi_1) & \cdots & \Psi_P(\xi_1) \\ \vdots & \vdots & \ddots & \vdots \\ \Psi_0(\xi_P) & \Psi_1(\xi_P) & \cdots & \Psi_P(\xi_P) \end{pmatrix} \begin{pmatrix} \alpha_0 \\ \alpha_1 \\ \vdots \\ \alpha_P \end{pmatrix} \tag{2.3}$$

Note that for this linear system, N_t is the minimum number of deterministic samples (N_s) required to obtain a solution of the determined system (i.e., the coefficient vector). If more samples are available (N_s>N_t) and linearly independent, the system is considered overdetermined and can be solved using a least squares approach. Polynomial chaos techniques, however, suffer from a "curse of dimensionality" in the sense that the number of determin-

istic model evaluations required to create an accurate surrogate model grows exponentially with the number of random dimensions. For many large-scale, complex problems, such as those found in modeling hypersonic reentry flows, it may be impractical to obtain the minimum required number of deterministic model samples. The most desirable approach is to obtain an accurate surrogate model with as few deterministic samples as possible to limit the computational cost, even if the minimum number of samples required for a total order expansion is not achievable.

If a case which has the number of deterministic model samples less than the minimum required for the solution to the determined system (N_s<N_t) is considered, then a system of linear equations is obtained that has fewer linearly independent equations than unknowns and possesses an infinite number of solutions. In a recent study by West and Hosder [15], it was shown that a small fraction of the PCE coefficients carry significant weight in the surrogate model. With the assumption that the expansion coefficient vector is sparse, the linear system can be regularized allowing for a well-posed solution. West and Hosder [15] presented a solution technique used by Asif [20] with the L_1-minimization problem using convex relaxation, where the objective is to seek a solution to the linear system with the fewest number of non-zero coefficients.

$$\min \left\| \alpha \right\|_1 \text{ subject to } \left\| \Psi\alpha - \alpha^* \right\|_2 \leq \delta \tag{2.4}$$

Here, δ is the error associated with the truncation of the series in Eq. (2.1). For the problems considered in this study, δ is assumed to be equal to zero, as it can be shown that the solution to Eq. (2.4) is unique with this assumption. In the above formulation, the dimensions of Ψ are N_s x N_t and the vector α^* is of length N_s. The vector α is of length N_t. Doostan and Owhadi [21] discuss, in great detail, the theory and formulation of the above method.

The optimization problem in Eq. (2.4) is commonly referred to as Basis Pursuit Denoising (BPDN) [21, 22, 20]. In the current study, the least absolute shrinkage and selection operator (LASSO) homotopy optimization routine [20] was selected to find the optimal solution of Eq. (2.4) and is shown to be efficient due to its convergence being weakly dependent on the dimension of the problem [22].

With this optimization and sparse-collocation approach, a procedure is followed for determining an acceptable sample size to achieve convergence and accuracy of the polynomial chaos expansion. The first step in this process is to generate an initial sample set of the uncertain variables. The size of this initial sample set, generated using Latin Hypercube sampling, is taken as the size, N_t, given by Eq. (2.2) as this would be the minimum number of samples required to obtain a total order expansion. Note that generating large sample sets of the uncertain parameters is not computationally expensive compared to the cost of evaluating the deterministic model. A small subset of the initial sample structure is selected, and the deterministic model is evaluated at these points. Then, a first set of PCE coefficients can be obtained using the minimization routine in Eq. (2.4). This process is then repeated by iteratively adding more samples to the solution procedure (i.e., addition of new subsets of the full sample structure) until the convergence of the expansion coefficients is achieved. Each subset of the full sample structure added at each iteration is restricted to not contain any repeated sample vectors from the previous iterations so that new information is provided in recovering a new solution at each iteration.

Convergence of the expansion coefficients is checked at each iteration. West and Hosder [15] presents methods used to track the convergence of the expansion coefficients and the resulting polynomial expansion. In this work, a method for variance-based global sensitivity analysis measures, Sobol indices [23, 24], is used to measure the convergence of the expansion coefficient vector as the Sobol indices highly depend on the coefficients

of the PCE. Further detail on this dependence and the derivation of total Sobol indices is given by West and Hosder [15]. The total Sobol index for each uncertain variable j ($S_{T,j}$) provides a sensitivity measure in terms of its total contribution to the total variance of the output quantity of interest. To monitor the convergence of the total Sobol indices with the addition of more samples at each iteration, an absolute error, $S_{e_{i,j}}$ can be defined for the j^{th} total Sobol index at iteration i using Eq. (2.5).

$$S_{e_{i,j}} = \left\| S_{T,i,j} - S_{T,i-1,j} \right\| \tag{2.5}$$

Note that measuring the convergence based on this absolute error puts emphasis on the variables that contribute to the output uncertainty more significantly. The errors of each total Sobol index, at each iteration, can then be averaged giving a single value for monitoring, which is shown in Eq. (2.6).

$$\mu_{e,i} = \frac{1}{n} \sum_{j=1}^{n} S_{e_{i,j}} \tag{2.6}$$

Plotting this average error at each iteration would then illustrate the convergence of the PCE coefficients. The objective is to seek out nearly asymptotic convergence, as zero error would likely not be achievable simply due to the randomness of the samples added at each iteration and any numerical noise that may occur during the analysis of complex models.

In this work, the stochastic problem contains both aleatory and epistemic types of uncertainty. For mixed uncertainty for which contributions of both types of uncertainty are considered, a procedure known as second-order probability [13] is used to propagate the mixed uncertainty through the stochastic model. Details on the uncertainty classification and second-order probability approach can be found in previous work which have been used to validate the UQ approaches and methodologies presented in this section [16, 14, 15].

2.2. DIMENSION REDUCTION

A significant number of uncertain parameters will be considered in the present study. Many of these parameters are expected to weakly contribute to the overall output uncertainty and may introduce noise to the response surface (and, likely the accuracy of the response surface). Therefore, in this study, the approach will be to reduce the number of uncertain variables with a small number of deterministic model evaluations by using the sparse approximation, point-collocation method. The ranking information for the uncertain parameters can be used to systematically reduce the number of random dimensions, which only includes significant uncertain parameters, and improve the accuracy of the response surface. An accurate uncertainty analysis for the problem with the reduced dimensions will be performed by using the point-collocation NIPC method. Note that there may be multiple levels of dimension reduction in order to ensure accurate relative ranking of the uncertain parameters as the number of parameters is reduced. In this study, only one level of dimension reduction was sufficient, which is shown in Section 4.

3. COMPUTATIONAL MODELS AND UNCERTAINTY SOURCES

This section presents an overview of the baseline computational models used in the modeling of F-TPS thermal response in the presence of external pressure and aerodynamic heating loads for Mars entry flow. The details of the flow and F-TPS thermal response solvers (Section 3.1), the HIAD geometry (Section 3.2) and nominal trajectory (Section 3.3), which includes the selection of the freestream conditions for CFD analysis, are given. In Section 3.4, uncertainty sources in the computational models are discussed and identified.

3.1. FLOW SOLVER AND F-TPS THERMAL MODEL

A one-dimensional physics-based TPS thermal model using COMSOL software is used to obtain the thermal response of the F-TPS in the presence of external pressure and aerodynamic heating loads [25, 26]. COMSOL is a finite element analysis solver and simulation package, developed by COMSOL, Inc., which is used for various multiphysics and engineering applications. Heat transfer is modeled within the F-TPS layers to predict the time dependent in-depth temperatures with given surface pressure and heat flux boundary conditions at the hot wall, relevant to test or flight conditions. The flexible TPS layup consists of two outer fabric layers, four layers of insulation material, and a gas barrier layer. The materials that make up the outer fabric and insulation are, in general, porous materials. Therefore, there are four major heat transfer modes to consider within the layers of the porous F-TPS materials: solid conduction, radiation, gas conduction, and advection (i.e., convection within porous material). Figure 3.1 depicts the one-dimensional F-TPS thermal model geometry with all the materials through which heat transfer is numerically modeled.

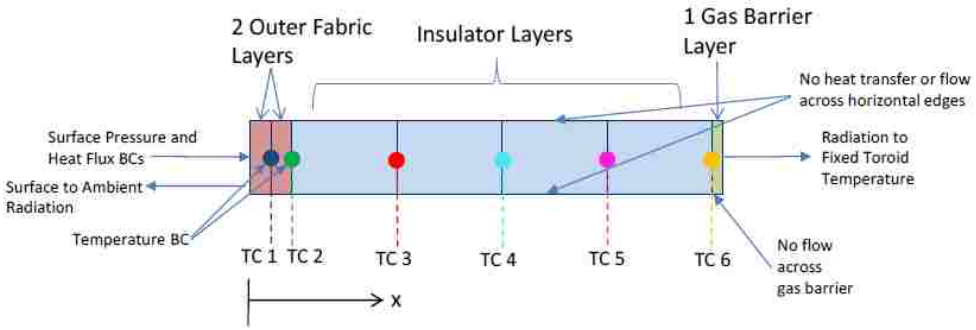

Figure 3.1. Flexible TPS thermal model

The amount of heat and mass that is transferred through the F-TPS layers is calculated from the solution of the local energy and gas mass conservation equations which are obtained from the theory of the flow of gases through a porous solid [6, 26]. The local energy conservation and the local gas conservation equations can be written as Eq. 3.1 and Eq. 3.2, respectively, where T is the temperature and t is time. All terms in Eq. 3.1 and Eq. 3.2 are written as per unit volume of the TPS.

$$\rho_s C_{ps} \frac{\partial T}{\partial t} - \frac{\partial}{\partial x}(k \frac{\partial T}{\partial x}) + \rho_g C_{pg} v_{gx} \frac{\partial T}{\partial x} + H_d \frac{\partial \rho_s}{\partial t} = 0 \tag{3.1}$$

$$\phi \frac{\partial \rho_g}{\partial t} + \frac{\partial}{\partial x}(\rho_g v_{gx}) = -\frac{\partial \rho_s}{\partial t} \tag{3.2}$$

$$v_{gx} = -\frac{k_x}{\mu_g} \frac{\partial p}{\partial x} \tag{3.3}$$

The modeling of the thermal response of a porous F-TPS is well-documented by Tobin and Dec [6]. The first term in Eq. 3.1 is the rate of energy storage in the control

volume, which depends on the solid density, ρ_s, and specific heat, C_{ps}. The second and third terms, combined, are the rate of change of energy due to net flux of heat transfer. The second term is the conduction heat flux through the F-TPS, which depends on the effective material conductivity, k. Note that the effective material thermal conductivity, k, in the second term inherently includes heat transfer by radiation and gas conduction. Therefore, any reference to conductivity refers to the sum of the solid, gas, and radiative conductivity. The third term is the heat flux by advection, which depends on the specific heat, C_{pg}, the density, ρ_g, and the velocity, v_{gx}, of the gas in the pores (assumed to be CO_2/N_2 based on super-catalytic conditions at the hot wall). The fourth term is the rate of energy consumed or generated as a result of the insulator decomposition reactions with associated heat of reaction, H_d. The first term on the left hand side of Eq. 3.2 is the rate of gas mass storage, and the second term is the rate of change of mass due to the net flux of gas crossing the control volume boundaries. The term on the right hand side is the rate of solid mass density depletion and accounts for the rate of pyrolysis gas generated due to the insulator decomposition reactions. The thermal properties of each material layer and gas (i.e., specific heat, thermal conductivity) are derived from experimental measurements of the TPS materials and individual gas species. Finally, gas pressure gradient is highly affected by the oxidation and outgassing of the insulation material, also known as pyrolysis. However, for super-catalytic hot wall boundary conditions, the O_2 specimen is not present for Mars entry. Therefore, any latent heat associated with the insulator oxidation reactions is neglected. Outgassing of the insulation material can occur at elevated temperatures above the critical temperature of charring and decomposition of highly porous materials.The thermal model also accounts for these outgassing effects. However, the effects of outgassing are insignificant in this study. Because pressure is normal to the surface, all gas flow is assumed to be along the x-direction based on Darcy's law in Eq. 3.3.

In this problem, the Langley Aerothermodynamic Upwind Relaxation Algorithm (LAURA) Navier-Stokes solver [27] from NASA Langley Research Center is used for the high-fidelity numerical solution of the hypersonic flowfield and boundary layer over a HIAD. LAURA is a three-dimensional, structured code, which uses a finite-volume, shock-capturing approach to solve high-speed flows with frozen, equilibrium, or nonequilibrium thermo-chemistry. The algorithm incorporates point-implicit or line-implicit relaxation schemes to efficiently obtain solutions on advanced computers and perform expensive computations for problems on a complex scale. An important feature of the code is the ability to perform one-dimensional grid adaptation to resolve high gradients in the boundary layer and across a shock wave. The flowfield for the current study is modeled in multi-species, two-temperature, thermo-chemical nonequilibrium for a Mars 8-species composition: CO_2, CO, N_2, O_2, NO, C, N, and O. This analysis focuses on modeling the flowfield with a fully turbulent boundary layer assumption using the Cebeci-Smith turbulence model [28]. For the nominal trajectory in Section 3.3, the computed Reynolds number based on major diameter of the HIAD becomes fairly large (above 1 million) during deceleration. The fully turbulent boundary layer assumption provides a conservative, worst-case measure of the heat fluxes applied to the F-TPS at the hot wall. For all results presented in this work, Yee's symmetric total variation diminishing inviscid flux scheme [29] is used with second order spatial accuracy construction of the inviscid flux terms. In addition, the viscous flux terms are calculated with second order spatial accuracy.

The boundary condition locations are also shown in Figure 3.1. Boundary conditions are applied as input with the time-dependent surface pressures and heat fluxes for the gas mass conservation and energy conservation equations, respectively. The boundary conditions are applied at x = 0 with the provided convective heating parameter and pressure predictions from LAURA. Note that the LAURA heat fluxes will not be directly coupled to

COMSOL. Instead, LAURA predictions are obtained at the cold wall temperature, which will be used as input to COMSOL for thermal response analysis. A correction in the heat flux is performed at each time instant based on an update of the wall enthalpy. For modeling the thermal response of the TPS in a Mars flight-relevant environment, the surface heat flux is input as a boundary condition in the form of Eq. 3.4.

$$q_w = C_H(H_{0e} - H_w) + \varepsilon\sigma(T_\infty^4 - T_w^4) \tag{3.4}$$

In Eq. 3.4, the first term is the input heat flux due to convection where C_H is the convective heat transfer coefficient based on enthalpy difference, H_{0e} is the total enthalpy at the boundary layer edge, and H_w is the wall enthalpy. The convective heat transfer coefficient based on enthalpy difference is also equal to $\rho_e u_e S_t$, where ρ_e and u_e are the density and velocity at the boundary layer edge, respectively, and S_t is the Stanton number based on boundary layer edge conditions. The second term is the heat transfer rejected at the surface by radiation, where ε is the emissivity of the outer fabric material, σ is the Stefan-Boltzmann constant, and T_∞ and T_w are temperatures of the freestream and HIAD surface, respectively. The heat transfer coefficient by convection, C_H, and total enthalpy, H_{0e}, are provided by LAURA and can be used as boundary condition input at the cold wall temperature. In addition, the remaining variables in Eq. 3.4 are user-supplied as input to the COMSOL solver, with the exception of the wall enthalpy. The surface energy balance for computing the surface temperature, and hence, wall enthalpy and hot-wall heat flux occurs within COMSOL. The approach for correcting the observed heat flux at elevated temperatures above the cold wall condition is presented in Section 3.3.

3.2. BASELINE REFERENCE GEOMETRY

The forebody of a 10m HIAD configuration is used for all CFD/TPS calculations. The dimensions of the HIAD forebody were scaled from the 6m article that was tested in the 40 x 80 foot test section of the NASA Ames National Full-Scale Aerodynamics Complex (NFAC) facility. The inflatable structure of the HIAD (shown in Figure 3.2) has a 60-deg sphere cone stacked torus design that consists of seven major tori and an eighth torus at the shoulder [30, 31]. A webbing of straps are attached to the tori, extending from the centerbody attachment, to sustain the stacked torus design shape. The inflatable structure is covered by the flexible TPS from the sphere-cone juncture and outward around the shoulder. The TPS thermal response analysis, therefore, considers the flank aerodynamic heating and surface pressures obtained from CFD analysis. Note that the 1-D thermal response analysis will be the most accurate for the flank region.

At each LAURA-computed surface location, a one-dimensional general F-TPS material layup is used for F-TPS thermal response calculations in Figure 3.3 with thermocouple locations between each material layer. In general, the layup consists of two outer fabric layers of silicon carbide, four layers of insulation material in combination of carbon felt and aerogel, and a gas barrier impermeable film material. The outer fabric protects the underlying insulation layers from direct exposure to the convective heat flux and the aerodynamic shear forces and from the abrasion and mechanical forces associated with small-volume packaging and deployment. The insulator layers reduce thermal soak back, and the gas barrier prevents hot gas impingement on to the inflatable structure. Of particular interest is the maximum bondline temperature at thermocouple 6 (TC-6) within the flexible TPS, which should not exceed the temperature limit of 400 degrees Celsius (^{o}C). Accurately predicting the bondline temperature ensures a safe and reliable TPS design, given that the most interior layer does not fail. Therefore, this work focuses on predicting the uncertainty

Figure 3.2. 6m test article at NFAC test facility

Figure 3.3. General TPS layup

in the bondline temperature of the flexible TPS subject to uncertainties in the convective heating and surface pressure at the hot wall and TPS material properties.

3.3. NOMINAL TRAJECTORY

An Exploration Feed Forward (EFF) study [4] investigated an EFF4 architecture with a 5.8 km/sec direct entry. Figure 3.4 shows the nominal trajectory corresponding to the EFF4 architecture, derived from a six degree-of-freedom (6-DOF) reentry dynamics simulations, with selected points for CFD analysis with LAURA. In Figure 3.5, the cold-wall stagnation-point heating rates, using engineering correlations by Sutton and Graves

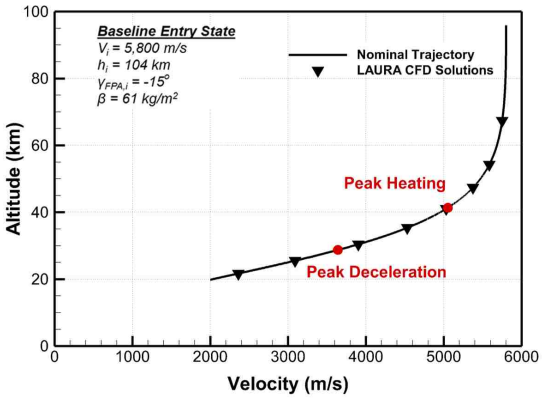

Figure 3.4. Ballistic entry profile for EFF-4 reference mission

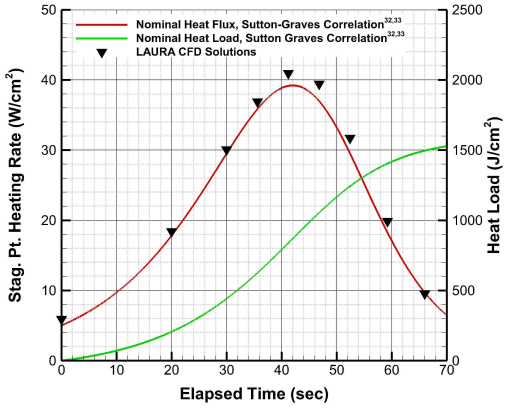

Figure 3.5. Cold-wall stagnation-point heating pulse and total head load of the nominal trajectory

[32, 33], are provided for the time duration of 70 sec within the continuum flow regime. As shown in Figure 3.5, the elapsed time is determined to be sufficient in obtaining a total heat load, based on cold-wall heat rates, of about 1500 J/cm^2. At 70 seconds, the HIAD is assumed to separate for transition to a secondary descent technology (i.e., supersonic retro-propulsion). The trajectory points, which will be used for CFD analysis, are selected to sufficiently capture the total heat load. Figure 3.6 shows that the Knudsen number is small enough (on the order of 10^{-3} or less) for this segment of the nominal trajectory to perform CFD calculations with continuum flow assumption. Furthermore, the Reynolds number based on major diameter begins to substantially increase (over 1 million) near peak heating of the nominal trajectory. Therefore, a fully turbulent boundary layer is assumed in this study.

Uncertainty analysis is performed throughout the trajectory with nominal freestream conditions listed in Table 3.1. The freestream composition is assumed to be 96% CO_2 and 4% N_2 by mole. The wall of the HIAD was modeled as super-catalytic (species composi-

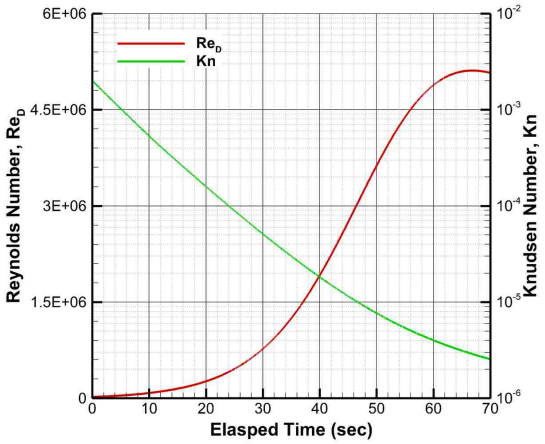

Figure 3.6. Knudsen and Reynolds numbers of the nominal trajectory

tion set to freestream values) for conservative measure of the surface convective heat flux [16]. The convective heating parameters and surface pressure, computed from LAURA at the trajectory points in the Table 3.1, were applied as input for the F-TPS thermal model in COMSOL at the cold wall temperature condition of 139 K. The TPS thermal model is simulated for the time duration of 70 seconds with cubic spline interpolation of the boundary condition input (convective heating parameter values and surface pressure values).

Preliminary calculations with LAURA are performed at several wall temperatures to study the effects of the convective heating input parameters for surface heat flux correction at elevated surface temperatures from the cold wall condition. All nine points from the nominal trajectory, shown in Figure 3.4, are used for LAURA computations. Figures 3.7 and 3.8 present the nominal total enthalpy (H_{0e}) and heat transfer coefficient (C_H) values at the nine trajectory points for wall temperatures of 139, 300, 1000, and 1500 K. As shown, the total enthalpy is unaffected by the wall temperature. In addition, the heat transfer coefficient is weakly dependent on the wall temperature with less than 3% variation. Therefore, at each time instant, the hot wall convective heat flux at elevated temperatures above the

Table 3.1. Trajectory points and corresponding baseline reference conditions for LAURA CFD analysis

Traj. Point	Time (sec)	*AoA* (deg)	Yaw (deg)	V_∞ (m/s)	ρ_∞ (kg/m^3)	T_∞ (K)
1	0.0	0.0	0.0	5800.0	2.591e-6	139.0
2	20.0	0.0	0.0	5749.3	3.440e-5	141.9
3	30.0	0.0	0.0	5584.2	1.123e-4	150.3
4	35.6	0.0	0.0	5375.4	2.081e-4	156.2
5	41.2	0.0	0.0	5031.6	3.686e-4	161.1
6	46.8	0.0	0.0	4531.2	6.163e-4	166.9
7	52.4	0.0	0.0	3903.3	9.621e-4	174.6
8	59.2	0.0	0.0	3088.9	1.285e-3	180.7
9	66.0	0.0	0.0	2361.2	2.117e-3	186.9

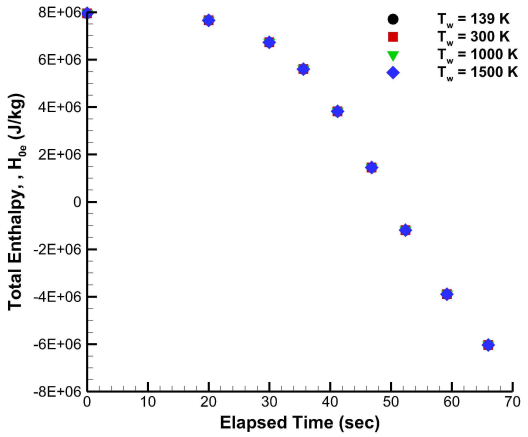

Figure 3.7. Boundary layer edge total enthalpy at Z=3.0 m surface location (flank)

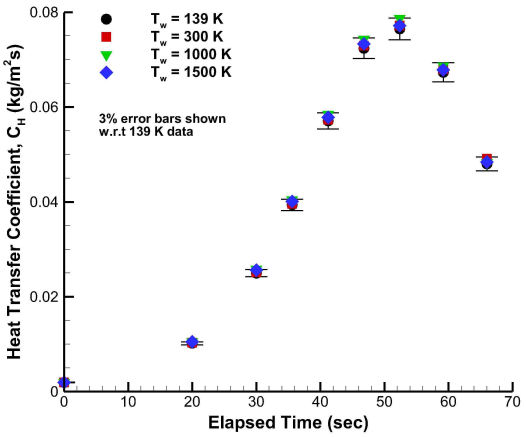

Figure 3.8. Heat transfer coefficient at Z=3.0 m surface location (flank)

cold wall temperature can be predicted by an update of the wall enthalpy, H_w, in Eq. 3.4, and using the provided cold-wall convective heating parameters (H_{0e} and C_H). The wall enthalpy is computed from the predicted surface temperature in COMSOL at each time instant.

3.4. UNCERTAINTY SOURCES

For this study, 22 uncertain input parameters related to flowfield and TPS thermal modeling of the HIAD, described in Section 3.1, are considered in the uncertainty analysis. Table 3.2 presents the various uncertainty source categories and assigned uncertainty ranges for the CFD and F-TPS thermal response modeling, which will be used in the UQ analysis for prediction of the in-depth temperatures of the F-TPS in Section 4. The first four uncertainties in Table 3.2 were identified as main contributors to convective heating uncertainty from a detailed uncertainty analysis of the flowfield modeling parameters and freestream conditions in a previous work at peak heating conditions [16]. In addition, these four uncertainties are confirmed to contribute approximately 95% of the total uncertainty in the convective heating at peak deceleration of the nominal trajectory, which is presented in Section 4.2. Only the freestream density was shown to affect the uncertainty in the wall pressure [16]. The uncertainties in the pressure and aerodynamic heating at the HIAD surface can strongly affect the F-TPS thermal response.

For this analysis, the freestream velocity and density are described through probabilistic measures due to its inherent nature. The freestream velocity input to the CFD simulation is treated as an aleatory uncertain variable with a normal distribution with a coefficient of variance (CoV) of 0.5% and mean values based on the nominal trajectory input to LAURA (Table 3.1). The freestream density is also treated as aleatory uncertain variable with uniform distribution and interval of $\pm$30% from the baseline reference values of the nominal trajectory (Table 3.1). The uncertainty ranges (CoV and uncertainty range assignments) are based on the uncertainty information obtained from a previous study [16].

Binary collision integrals have been shown to be important modeling parameters in high temperature flows to accurately model the transport quantities that govern the shear stress and heat flux at the HIAD surface. A study by Wright et al. [35] indicates that

Table 3.2. Summary of uncertain parameters for the HIAD TPS thermal response simulations

Uncertain Comp.	Uncertain Param.	Description	Classification	Uncertainty	Ref.
Convective heating surface pressure	ρ_∞	Freestream Density	Uniform	±30%	
	V_∞	Freestream Velocity	Normal	0.5% CoV	[17]
	$A_{CO2\text{-}CO2}$	CO_2-CO_2 Collision	Epistemic	±30%	[16]
	$A_{CO2\text{-}O}$	CO_2-O Collision	Epistemic	±30%	
Outer Fabric Layers (2)	$K_{s,OF}$	OF Thermal Cond.	Epistemic	±30%	
	$k_{x,OF}$	OF Permeability	Epistemic	±30%	Same as IN1
	ε	OF Emissivity	Epistemic	±10%	uncertainties
	$C_{ps,OF}$	OF Specific Heat	Epistemic	±20%	
Insulator 1 Layers (3)	$K_{s,IN1}$	IN1 Thermal Cond.	Epistemic	±30%	Expert Opinion
	$k_{x,IN1}$	IN1 Permeability	Epistemic	±30%	Expert Opinion
	$C_{ps,IN1}$	IN1 Specific Heat	Epistemic	±20%	Expert Opinion
	$h_{1,IN1}$	IN1 Layer 1 Thickness	Normal	3% CoV	Expert Opinion
	$h_{2,IN1}$	IN1 Layer 2 Thickness	Normal	3% CoV	Expert Opinion
	$h_{3,IN1}$	IN1 Layer 3 Thickness	Normal	3% CoV	Expert Opinion
Insulator 2 Layers (1)	$K_{s,IN2}$	IN2 Thermal Cond.	Epistemic	±30%	Expert Opinion
	$k_{x,IN2}$	IN2 Permeability	Epistemic	±30%	Expert Opinion
	$C_{ps,IN2}$	IN2 Specific Heat	Epistemic	±20%	Expert Opinion
	h_{IN2}	IN2 Layer Thickness	Normal	10% CoV	Expert Opinion
	$\rho_{0,IN2}$	IN2 Virgin Density	Normal	10% CoV	Expert Opinion
	$E_{a,IN2}$	IN2 Activation Energy	Epistemic	±20%	[34]
Gas Barrier (GB) Layer	$K_{s,GB}$	GB Thermal Cond.	Epistemic	±15%	Expert Opinion
	$C_{ps,GB}$	GB Specific Heat	Epistemic	±5%	Expert Opinion
TOTAL	**22**				

there can be as much as 30% uncertainty associated with binary collision integrals. The uncertainty in the CO_2-CO_2 and CO_2-O interactions were modeled as epistemic due to lack of knowledge in the CFD physical model. The uncertainty in the binary collision integrals are implemented through the use of a single parameter, A, similar to the studies by Bettis et al. [36] and Bose et al. [37]:

$$\Omega^{1,1} = A f_1(T) \tag{3.5}$$

$$\Omega^{2,2} = A f_2(T) \tag{3.6}$$

The functions f_1 and f_2 are expressions with temperature dependence, and the form of the curve fits are presented by Gupta et al. [38] The A parameter (multiplier) in Eq. 3.5-3.6 is treated as the uncertain parameter with lower bound of 0.7 and upper bound of

1.3, which corresponds to a $\pm 30\%$ uncertainty [37]. In Eq. 3.5, $\Omega^{1,1}$ is used to calculate the diffusion coefficients. Likewise, in Eq. 3.6, $\Omega^{2,2}$ is used to calculate the viscosity coefficients. Furthermore, as noted by Wright et al. [39], both of these collision integrals are used to compute the thermal conductivity.

The remaining uncertainty sources listed in Table 3.2 represent the final category of uncertainty in the TPS thermal model. The uncertainties due to most parameters are determined by surveillance of material property data from experimental testing and expert opinion from subject matter experts (Steven Tobin and John Dec from NASA Langley Research Center) involved with F-TPS modeling of the HIAD. Rossman [34] determined the uncertainty in the activation energy to characterize decomposition of the insulator layer using thermogravimetric analysis. Due to the lack of sufficient data to assign a probabilistic distribution, most of these parameters are modeled as epistemic uncertain variables with intervals. If sufficient data is available, a probabilistic distribution is assigned.

4. RESULTS AND DISCUSSION

4.1. BASELINE RESULTS FOR THE NOMINAL TRAJECTORY

Prior to constructing the response surface and performing the uncertainty analysis, a baseline solution is first obtained with the nominal values of the uncertain modeling parameters considered in this study. Baseline flowfield solutions are obtained with LAURA at the trajectory points in Table 3.1 using the 139 K cold wall temperature condition. Figure 4.1 presents the baseline computational grid for the 10m HIAD geometry, which consists of 128x48 normal-by-streamwise grid cells, with translational temperature contours at trajectory point 7 near peak deceleration. Grid clustering near the shock is essential to fully capture the shock and thermodynamic nonequilibrium region near the shock [40]. As mentioned previously in Section 3.1, LAURA utilizes a gradient-based shock capturing approach with a grid clustering feature in the flow direction to resolve gradients near the shock. As shown in Figure 4.2, the flow is in nonequilibrium just behind the shock. Therefore, capturing the spike in the nonequilibrium region and the smoothness of the shock standoff distance (Figure 4.3) is important in accurate modeling of the flowfield.

Baseline fully turbulent convective heating and pressure solutions are presented in Figure 4.4. For fully turbulent flow, the convective heating in the flank region ($Z \geq 1.0$m) of the HIAD is much higher (by as much as a factor of two) than the heating predicted at the stagnation point. This emphasizes the conservative aspect of the heating exposed to the surface in the flank and shoulder regions, where the flexible TPS is used to protect the inflatable structure of the HIAD. The expectation is that the region of maximum convective heating plays a major role in identifying the critical surface location of maximum in-depth temperature response of the F-TPS.

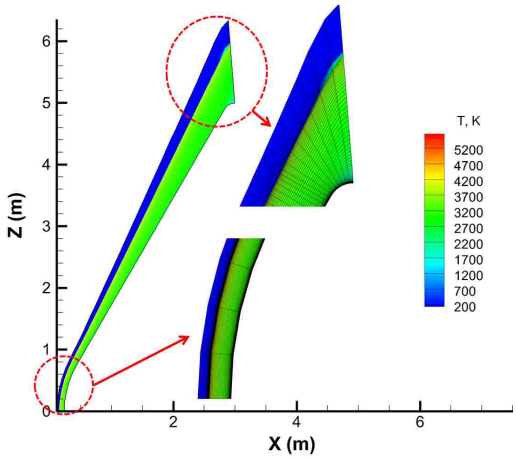

Figure 4.1. Computational grid with baseline solution contours of translational temperature

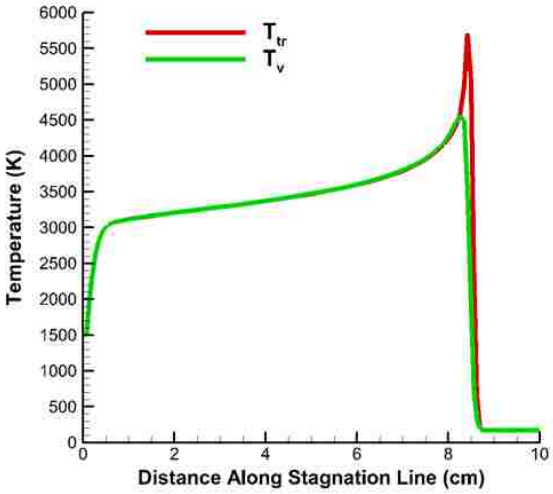

Figure 4.2. Stagnation line temperatures for the baseline solution

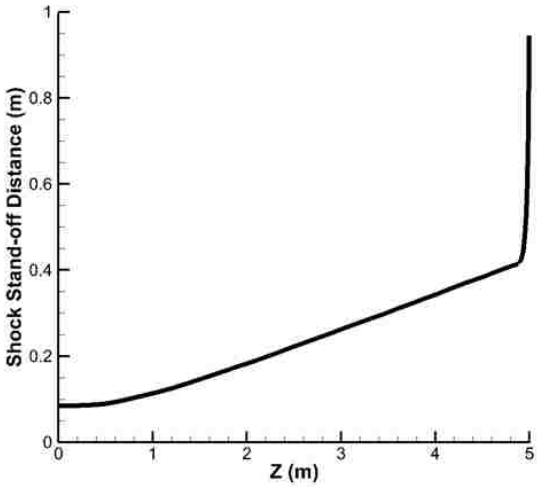

Figure 4.3. Shock standoff distance for the baseline solution

The convective heating parameters (C_H and H_{0e}) and surface pressures are further extracted from LAURA for input as boundary conditions in COMSOL at each LAURA-computed trajectory point. Figure 4.5 presents the cold-wall convective heat flux boundary condition input, denoted by the blue gradient symbols. The values in between the provided data are obtained by cubic spline interpolation. At each time instant, the hot-wall

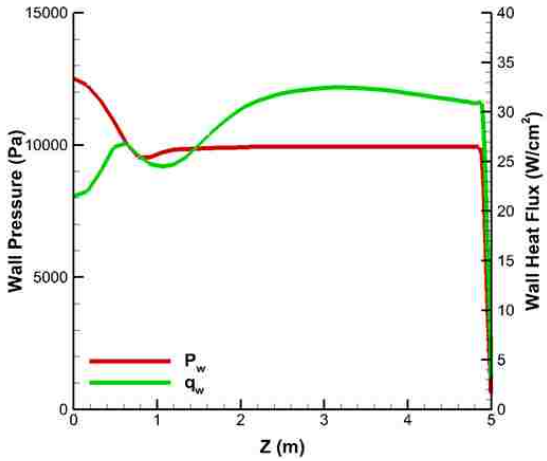

Figure 4.4. Baseline convective heating and surface pressure solutions near peak deceleration (flank region Z$\geq$1.0m)

convective heat flux is calculated based on an update of the wall enthalpy and the provided cold-wall C_H and H_{0e} convective heating parameters. As the surface temperature increases beyond the initial time, the difference between hot-wall convective heat flux (blue solid line) and cold-wall convective heat flux (blue gradient symbols) becomes distinguishable. Furthermore, the surface-to-ambient radiation rejected at the surface is calculated at each time instant; as a result, the net heat flux experienced by the F-TPS at the hot wall is the net summation of the radiative and hot-wall convective heat fluxes. Note that the net heat flux is not zero and affects the surface conduction within the first layer of the F-TPS.

F-TPS in-depth temperature calculations with COMSOL are performed at three surface points of the HIAD along the flank where the TPS is used to protect the underlying inflatable structure (Figure 4.6). Figure 4.7 presents the nominal in-depth temperatures between the layers of the F-TPS (TC-1 through TC-6) at surface point P2. The thermal response analysis is terminated once the bondline temperature (TC-6) reaches a peak value of about 400 ^{o}C at about 85 seconds to provide insight for the scenario if the HIAD is used throughout the trajectory instead of a secondary descent technology (i.e., supersonic

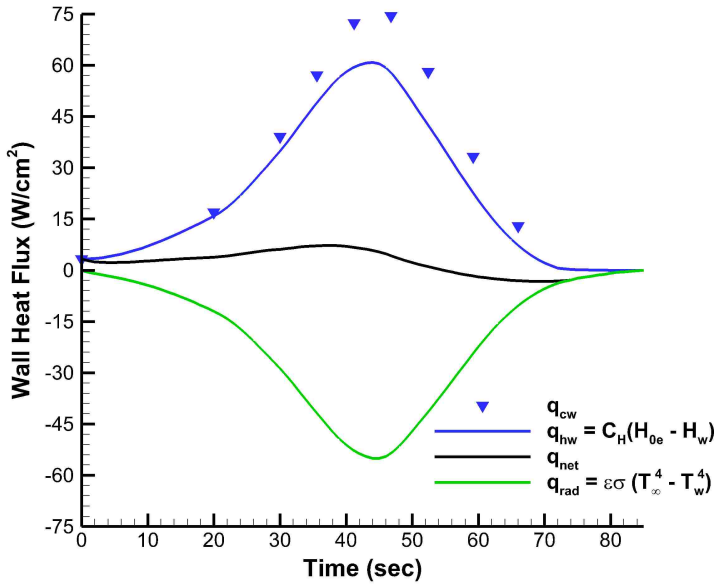

Figure 4.5. Heat flux profiles for the cold-wall and hot-wall convective heat flux and surface-to-ambient radiative heat flux

retro-propulsion) in the supersonic range. However, for uncertainty analysis, the thermal response calculations terminate at 70 seconds, which is based on the assumption that the HIAD will separate for transition to a secondary descent technology. In Figure 4.8, the time-dependent bondline temperature profiles are presented for the three surface points in Figure 1. As shown, the critical bondline temperature is observed at the P2 location in the flank region of the HIAD. In general, the P2 location experiences the highest bondline temperature throughout the trajectory compared to P1 and P3 surface points. At surface point P2, the F-TPS is exposed to maximum external heat flux due to fully turbulent flow assumption with augmented heating values (as much as factor two) along the flank surface, compared to the stagnation point. This work focuses on uncertainty analysis of the bondline temperature at surface point P2 (Sections 4.3-4.4).

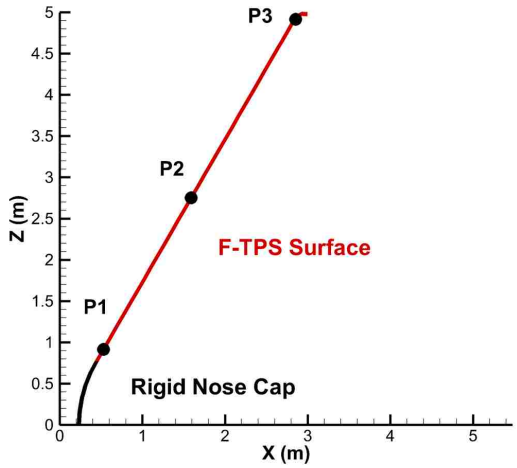

Figure 4.6. Surface points for F-TPS response analysis for the nominal trajectory

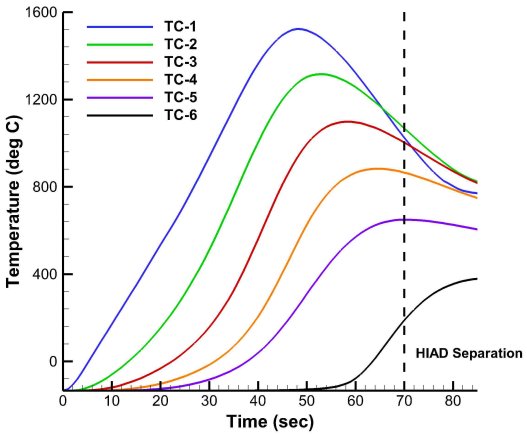

Figure 4.7. Time-dependent temperature profiles for in-depth TPS locations at surface point P2

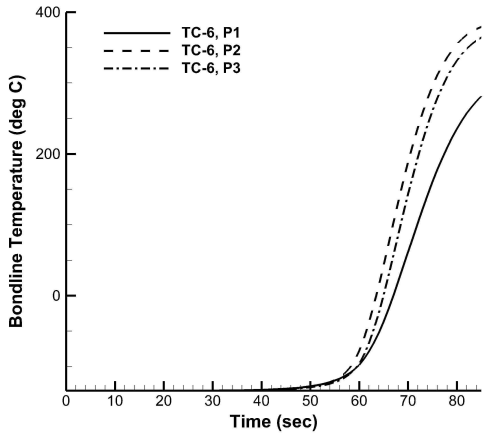

Figure 4.8. Time-dependent bondline temperature profiles for three HIAD surface points

For the baseline solution, Table 4.1 presents the computational time requirements for CFD calculations of a single trajectory point and F-TPS calculations of the full 70-second trajectory time frame. Two processors (Dual socket 12-core Dell PowerEdge R710) with four gigabytes access memory each from the Numerical Intensive Cluster (NIC) at Missouri University of Science and Technology are used for CFD analysis. Four proces-

Table 4.1. Computing time (hours) for the baseline solution

Analysis Segment	Computing Time (hours)
LAURA (CFD)	36
COMSOL (F-TPS)	0.5

sors (Quad-core Dell Optimplex 780) from the local computer are used to complete the F-TPS response analysis with external boundary condition input (convective heating parameters and surface pressure) from LAURA. As shown, the CFD analysis accounts for 98% of the required computing time to complete both analyses. The approach is to restart a converged, baseline CFD solution at each trajectory point for performing the uncertainty and sensitivity analyses. This can reduce the computational time required by as much as half for a converged solution when only small changes to input parameters are made for CFD analysis.

4.2. VERIFICATION OF THE SENSITIVITY OF CONVECTIVE HEATING UNCERTAINTY

In previous work [16], global nonlinear sensitivity analysis showed that the freestream density and velocity, and the CO_2-CO_2/CO_2-O binary interactions were the main contributors to 95% of the aerodynamic heating uncertainty at peak heating. Because the current work aims to perform an uncertainty analysis of the F-TPS response throughout the nominal trajectory, this section presents the sensitivity results at peak deceleration to confirm that the main contributors are unchanged for the 70 second duration. A total of 65 uncertain parameters are considered for this analysis at peak deceleration. Details regarding these uncertain parameters and assigned uncertainties are given by Brune et al. [16]

With a total of 65 uncertain parameters considered as input to the CFD deterministic model, the PCEs require a minimum of 2211 CFD evaluations for a second order polynomial expansion using Eq. 2.2. Traditional Monte Carlo methods are infeasible with the time demand and complexity of the evaluations. In practice, a minimum number of CFD evaluations would be ideal to construct an accurate surrogate model. Therefore, the efficient UQ approach with sparse approximation, described in Section 2, is used.

Using the procedures outlined in Section 2.1 for the stochastic sparse expansion approach, an initial sample set is generated with 2211 samples using Latin hypercube sampling. A subset of 10 samples are randomly selected at the first iteration to construct the response surface for convective heating, and 10 samples are added to the analysis at each iteration until convergence. Figure 4.9 presents the convergence of the mean total Sobol error, normalized by the maximum, for the response surfaces of the convective heat flux that span all 49 surface grid locations on the HIAD. Significant variation of the error is shown for small sample sizes. As the sample size increases, the error drops rapidly to errors approximately or less than 0.02 at 400 samples. Compared to the 2211 samples required for a second order expansion using point-collocation, the stochastic expansion approach with sparse approximation is able to recover convergence of the polynomial chaos expansion coefficients (and hence, Sobol indices) using at most 400 CFD evaluations (80% reduction in the computational cost).

Figure 4.10 presents the main contributors to approximately 95% of the uncertainty in the aerodynamic (convective) heating for the entire HIAD surface. Overall, the four main contributors identified to contribute approximately 95% of the convective heating uncertainty are confirmed to be unchanged at peak deceleration. As expected, the freestream density dominates the convective heating towards the flank and shoulder regions due to its effect on Reynolds number and turbulent (eddy) viscosity. The Reynolds number based on

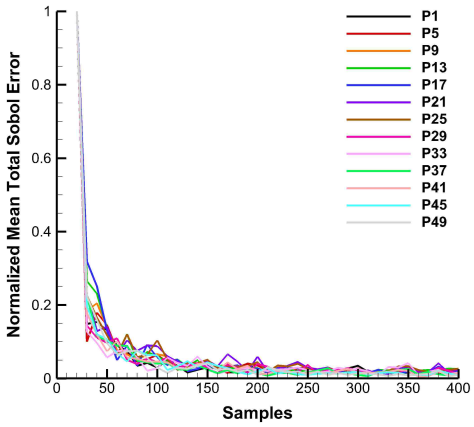

Figure 4.9. Convergence of the response surfaces for all LAURA-computed surface points

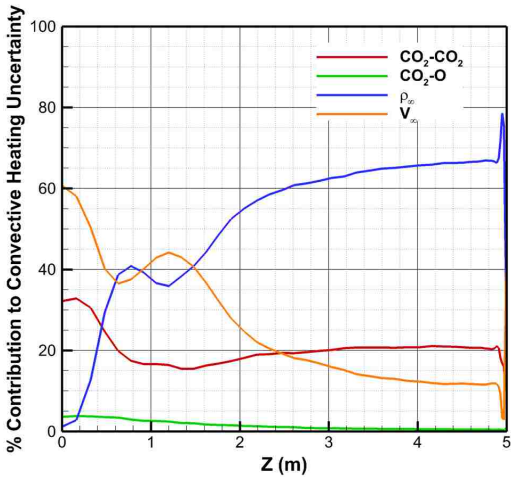

Figure 4.10. Sensitivity contributions to the convective heating uncertainty for the entire HIAD surface

momentum thickness plays a significant role on turbulent heating augmentation. Velocity contribution, however, decreases downstream of the sphere-cone juncture. The CO_2-CO_2 collision partner also shows significance to the convective heat transfer uncertainty with small contribution from the CO_2-O collision partner. The binary collision interactions play a major role in the transport properties (i.e., thermal conductivity). Overall, this study verifies the selection of the important hypersonic flowfield uncertainty sources that contribute to the uncertainty in convective heating throughout the entire trajectory.

4.3. STOCHASTIC RESPONSE SURFACE CONSTRUCTION FOR WALL CONVECTIVE HEATING AND PRESSURE PREDICTION

In Section 3.3, the heat flux correction approach was presented and showed that the CFD analysis can be performed separately from the F-TPS response analysis. In Section 4.1, CFD evaluations were reported to account for a majority (approximately 98%) of the computational cost compared to the F-TPS thermal model evaluations. Therefore,

the goal is to minimize the number of high-fidelity CFD model evaluations while retaining the desired accuracy in the output quantities of interest. The number of evaluations, of course, depends on the number of random dimensions considered to create a response surface. Considering all 22 uncertainty sources, 276 CFD evaluations are needed to create a 2^{nd} order response surface at each trajectory point for uncertainty analysis of the F-TPS in-depth temperatures using the convective heating and surface pressure information from LAURA. However, one can replace the actual CFD model with a separate response surface for the convective heating parameters and surface pressures, considering only the first four uncertainty sources. The second approach only requires 30 CFD evaluations with just four uncertain variables to create a 2^{nd} order response surface at each trajectory point.

Figure 4.11 illustrates the framework for obtaining the F-TPS bondline temperatures with the actual F-TPS thermal model and response surface prediction of the CFD-supplied parameters. The first four uncertainty sources are considered to construct response surfaces for the wall pressure and convective heating parameter uncertainties, which can be propagated as input for the F-TPS thermal model in COMSOL. The remaining sources are uncertain model parameters (material properties, thicknesses, and decomposition modeling of the F-TPS), which are directly applied to the F-TPS thermal model for UQ analysis of the in-depth temperatures in Sections 4.4 and 4.5. Point-collocation NIPC, instead of the sparse approximation approach, is implemented because there are only four flowfield uncertain variables to construct the responses surfaces with a second order expansion (30 CFD simulations required at each trajectory point).

The dispersions predicted by the response surfaces can be extracted at a particular surface location of interest and can be propagated through the F-TPS thermal model as boundary conditions using the samples generated of the uncertain input variables. For the critical location P2, where the F-TPS experiences maximum convective heating due to fully

Figure 4.11. F-TPS thermal model framework for obtaining bondline temperature

turbulent flow assumption and maximum F-TPS bondline temperature, the uncertainties (95% confidence intervals (CI)) for the LAURA-computed trajectory points are shown in Figures 4.12(a)-4.12(c) for the wall pressure, total enthalpy, and heat transfer coefficient, respectively. In general, the surface pressure and convective heating parameters experience the largest uncertainty between 60 and 70 seconds, prior to separation of the HIAD for transition to a secondary descent technology.

4.4. SENSITIVITY ANALYSIS OF F-TPS BONDLINE TEMPERATURE UNCERTAINTY

Recall from Section 3.3 that there are a total of 22 uncertain parameters considered in this study. As a result, propagating the uncertainty with a second order PCE would require a minimum of 276 evaluations of the F-TPS thermal model to construct a total order expansion using Eq. (2). The objective is to reduce this number to a reasonable size by constructing the surrogate model with only those parameters that significantly contribute to

the uncertainty in the bondline temperature. As shown in the previous subsection, response surfaces as a function of the first four uncertain parameters in Table 3.2 are used for prediction of the convective heating parameters (C_H and H_{0e}) and surface pressure as boundary condition input for the F-TPS thermal model. The remaining uncertain parameters are used as input for the F-TPS thermal model in COMSOL.

Following the approach outlined in Section 2.1, an initial Latin hypercube structure of 100 samples is generated using all 22 uncertain variables. A sparse approximation of the PCE are then constructed with Eq. 2.4 and the total Sobol indices are calculated iteratively, using the PCE expansion coefficients, for an increasing sample size from 10 to 100 by 10 samples. This approach allows for tracking of the convergence of the Sobol indices (Eqs. 2.5 and 2.6).

The convergence of the Sobol indices is illustrated in Figure 4.13. Figure 4.13(a) shows a plot of the convergence of the maximum relative change among all of the uncertain parameters at surface point P2 for the bondline temperature at 70 seconds. At 50 samples, there was a change of about 10%, but increasing the sample size to 100 reduced the maximum change to only 1%. Figure 4.13(b) shows the convergence of total Sobol indices for the top eight uncertain parameters that contribute significantly to the bondline temperature uncertainty. These eight parameters are responsible for 95% of the bondline temperature uncertainty. Convergence in the sensitivities is determined to be sufficient at 100 samples with small variations in the individual Sobol indices and the maximum relative error reaching a threshold of 1%.

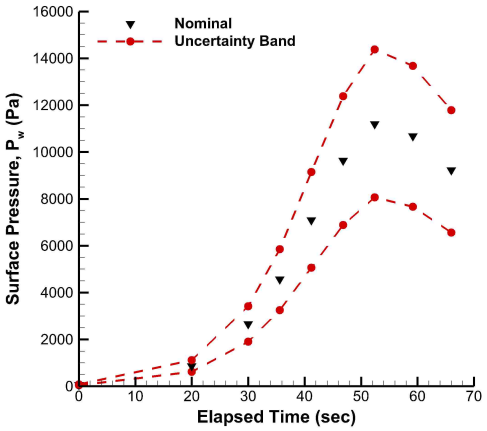

(a) Surface Pressure

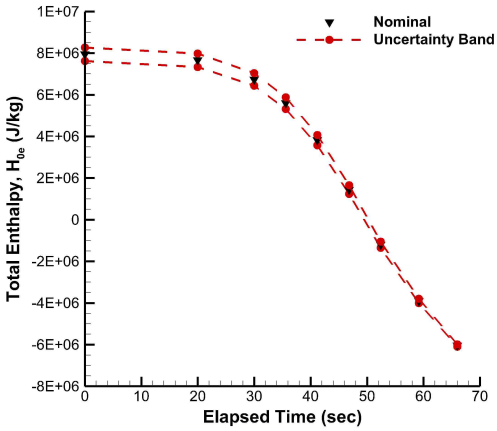

(b) Boundary layer edge total enthalpy

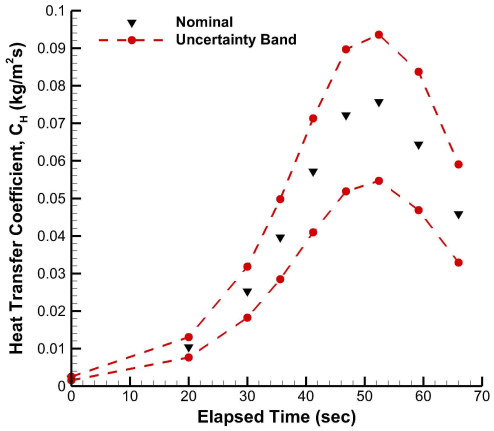

(c) Heat transfer coefficient based on enthalpy difference

Figure 4.12. 95% CI uncertainty bands and nominal values for the convective heating parameters and surface pressure

4.5. UNCERTAINTY ANALYSIS OF F-TPS BONDLINE TEMPERATURE IN THE REDUCED DIMENSION

With the 22 uncertain variables reduced to only eight (Figure 4.13(b)), an estimate of the uncertainty can be quickly and accurately calculated. A second order PCE surro-

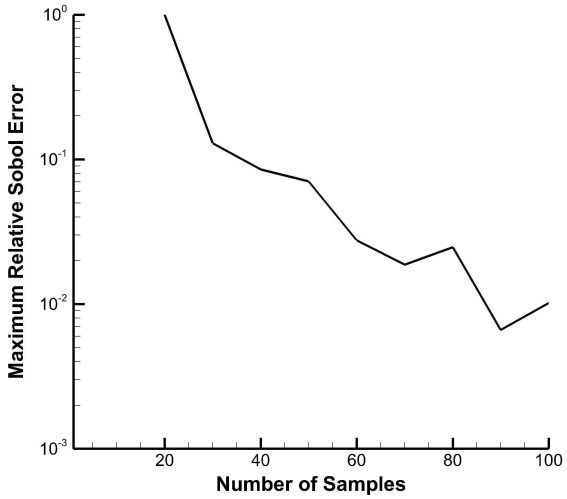

(a) Maximum relative change

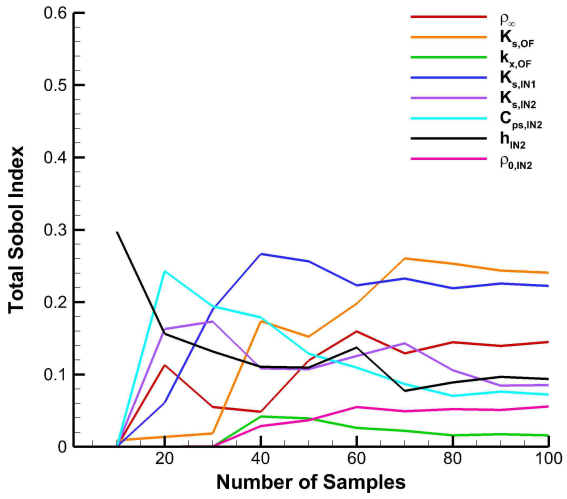

(b) Top 8 variables

Figure 4.13. Convergence of the total Sobol indices for the bondline temperature uncertainty at 70 seconds

gate model for the bondline temperature is constructed using 90 evaluations of the F-TPS thermal model, which is twice the minimum number required for a total order expansion

(OSR = 2). Note that the response surfaces for prediction of the convective heating and surface pressure parameters are again used for boundary condition input for the F-TPS thermal model. As shown in the previous subsection, the freestream density was identified as one of the top eight main contributors to the bondline temperature uncertainty. Therefore, the freestream density is only dispersed while the remaining three uncertain flowfield parameters are fixed at their nominal values.

Once the surrogate model is constructed for the bondline temperature at one-second intervals for the 70-second time frame, the uncertainty is then propagated through the surrogate model via Monte Carlo sampling with 10^6 samples. The uncertainty band of the bondline temperature (95% confidence interval), along with the total Sobol index values for each parameter, for the 70-second time frame are shown in Figure 4.14. The uncertainty band is, at a maximum, 125% above and about -50% below the nominal prediction. The greatest uncertainty occurs at 70 seconds, just prior to HIAD separation for transition to a secondary descent technology. Clearly, the uncertainty in the eight key parameters produces a significant amount of uncertainty in the bondline temperature prediction. At 65 seconds, the upper bound of the uncertainty band exceeds the 400 ^{o}C temperature limit of the bondline temeprature. As a result, additional work is needed to determine the thickness requirement, and hence thickness margin, of the F-TPS to ensure the upper bound of the uncertainty band does not exceed the limit state of the bondline temperature. A target reliability level of the bondline temperature is needed to size the F-TPS, which will be investigated in a future study. For the current F-TPS design, the target reliability of the bondline temperature can also be met by reducing the uncertainty in the atmospheric model (i.e., freestream density) and other F-TPS physical parameters with more experiments, measurements, and data. Furthermore, the uncertainty in the bondline temperature exceeding the 400 ^{o}C temperature limit provides an implication of the HIAD to be sepa-

rated prior to supersonic retropropulsion to reduce the overall system risk. Allowing the HIAD to continue throughout the trajectory can increase the risk of the system with further increase in the bondline temperature than what is presented in this work.

The Sobol indices in Figure 4.14(b) are shown to identify the trends in the sensitivities as a function of time. At approximately 25 seconds, the bondline temperature begins to vary from the initial temperature condition of 139 K. Initially, the thickness and thermal conductivity of the insulator 2 layer, near the gas barrier, are the main contributors to the bondline temperature uncertainty prior to an abrupt increase in the temperatures at 50 seconds. At 50 seconds, the importance of the insulator 2 layer parameters decrease, and the thermal conductivity of the outer fabric and insulator 1 layer, and the freestream density, become significant. The abrupt increases in the bondline temperature are dictated by the thermal gradients in the outer fabric and insulator 1 layer. In addition, the freestream density uncertainty becomes a major factor further along the trajectory as the HIAD passes through higher densities near peak deceleration.

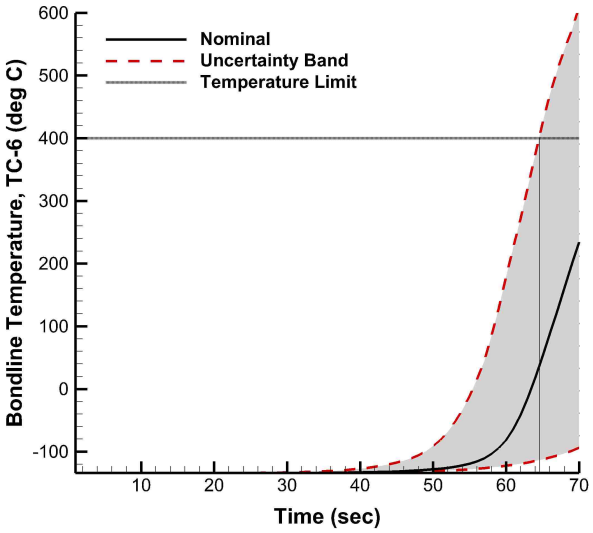

(a) Uncertainty band

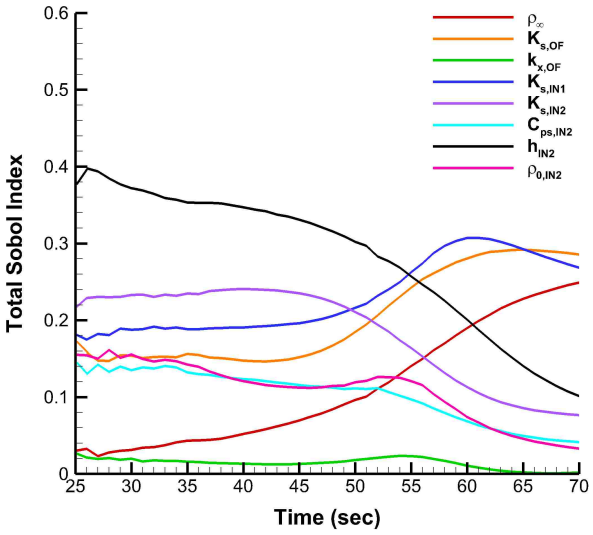

(b) Total Sobol indices

Figure 4.14. Sensitivities and uncertainty band of bondline temperature with reduced dimension of uncertain variables

5. CONCLUDING REMARKS

The primary objective of this paper is to present a detailed uncertainty analysis for prediction of the in-depth temperatures of the thermal protection system (TPS) of a HIAD due to uncertain flowfield and TPS thermal modeling parameters. The HIAD forebody considered has a 60-deg sphere-cone shape with a 10 meter major diameter. A sparse stochastic expansion approach was used to conduct a global senstivity analysis for dimension reduction of the uncertain parameters. The reduced dimension of uncertain parameters were applied with a point-collocation stochastic expansion approach for uncertainty analysis of the flexible TPS thermal response. The sensitivity analysis is crucial to identify the key parameters that contribute most to the uncertainty in the bondline temperature near the gas barrier layer of the flexible TPS. Additionally, the uncertainty analysis is expected to provide useful information for future work in TPS margin prediction and thickness sizing requirements.

In this work, the high-fidelity baseline model was presented with discussion on the LAURA flow solver and the COMSOL multi-physics code for TPS thermal modeling of porous materials subject to convective heat transfer and pressure loads. A reference nominal trajectory was also presented based on the Exploration Feed Forward study with 5.8 km/s direct entry with selected trajectory points for analysis with the LAURA flow solver, which is used for external convective heating parameters and surface pressure input to the COMSOL solver. The baseline solution showed that the critical surface point for maximum bondline temperature occurred in the flank region with fully turbulent flow assumption. At this surface point, response surfaces were constructed for the convective heating parameters and surface pressure to replace the CFD model at each trajectory point. This approach

reduced the number of high-fidelity CFD evaluations required in the creation of a stochastic response surface by considering only four flow field uncertain variables (freestream velocity, freestream density, and CO_2-CO_2/CO_2-O binary interactions). These stochastic response surfaces for the convective heating parameters and surface pressures at each trajectory point were used as input for F-TPS response analysis.

A global nonlinear sensitivity analysis was performed and showed that eight of the 22 uncertain parameters contributed to 95% of the bondline temperature uncertainty. An uncertainty analysis of the bondline temperature was performed with the reduced dimension of eight uncertain parameters, which included the freestream density, thermal conductivities of the insulator and outer fabric layers, and thickness and initial density of the insulator layer 2 near the gas barrier layer. Uncertainty analysis showed that the bondline temperature varies by as much as 125% above the nominal prediction, and the upper bound of the uncertainty band exceeds the limit state of the bondline temperature at 65 seconds, prior to HIAD separation at 70 seconds. As a result, additional work is recommended to determine the thickness requirement, and hence thickness margin, of the flexible TPS to ensure the upper bound of the uncertainty band does not exceed the 400 ^{o}C limit of the bondline temperature in the presence of uncertainty sources considered for the hypersonic flowfield and the flexible TPS thermal model.

ACKNOWLEDGMENTS

This work was supported by a NASA Space Technology Research Fellowship under training project grant no. NNX13AL58H (Serhat Hosder, principal investigator and Karl Edquist, research collaborator). The authors would like to thank John Dec from NASA Langley Research Center for providing guidance and technical support for the TPS thermal response modeling process and providing information to make this work possible.

BIBLIOGRAPHY

[1] Drake, B. G., "Human Exploration of Mars Design Reference Architecture 5.0," Tech. rep., NASA-SP-2009-566, 2009.

[2] Zang, T. A., Dwyer-Ciancolo, A. M., Kinney, D. J., R.Howard, A., Chen, G. T., Ivanov, M. C., Sostaric, R. R., and Westhelle, M. C., "Overview of the NASA Entry, Descent, and Landing Systems Analysis Studies for Large Robotic-class Missions, AIAA 2010-8649," *AIAA SPACE 2010 Conference and Exhibition*, Anaheim, CA, Aug. 2010.

[3] Dwyer-Ciancolo, A. M., Davis, J. L., Shidner, J. D., and Powell, R. W., "Entry, Descent, and Landing Systems Analysis: Exploration Class Simulation Overview and Results," *AIAA/AAS Astrodynamics Specialist Conference*, Toronto, Ontario Canada, Aug. 2010.

[4] Dwyer-Ciancolo, A. M., Davis, J. L., Engelund, W. C., Komar, D. R., Queen, E. M., Samareh, J. A., Way, D. W., and Zang, T. A., "Entry, Descent, and Landing Systems Analysis Study: Phase 2 Report on Exploration Feed-Forward Systems," Tech. rep., NASA/TM-217055, Feb. 2011.

[5] "NASA What's Next?" http://www.nasa.gov/hiad, Accessed: 2014-10-09.

[6] Tobin, S. A. and Dec, J. A., "A Probabilistic Sizing Demonstration of a Flexible Thermal Protection System for a Hypersonic Inflatable Aerodynamic Decelerator, AIAA 2015-1895," *AIAA SciTech Conference*, Kissimmee, FL, Jan. 2015.

[7] Bruce III, W. E., J., M. N., Furlemann, P. G., Siemers III, P. M., Del Corso, J. A., Hughes, S. J., Tobin, S. A., and Kardell, M. P., "Aerothermal Ground Testing of Flexible Thermal Protection Systems for Hypersonic Inflatable Aerodynamic Decelerators," *9th International Planetary Probe Workshop*, Toulouse, France, 2012.

[8] Hosder, S. and Bettis, B., "Uncertainty and Sensitivity Analysis for Reentry Flows with Inherent and Model-Form Uncertainties," *Journal of Spacecraft and Rockets*, Vol. 49, No. 2, 2012, pp. 193–206.

[9] Bettis, B., Hosder, S., and Winter, T., "Efficient Uncertainty Quantification in Multidisciplinary Analysis of a Reusable Launch Vehicle, AIAA 2011-2393," *17th AIAA International Space Planes and Hypersonic Systems and Technologies Conference*, San Francisco, CA, 2011.

[10] Hosder, S., Walters, R. W., and Balch, M., "Efficient Sampling for Non-Intrusive Polynomial Chaos Applications with Multiple Uncertain Input Variables, AIAA 2007-1939," *48th AIAA/ASME/ASCE/AHS/ASC Structures, Structural Dynamics, and Materials Conference*, Honolulu, HI, April 2007.

[11] Hosder, S., Walters, R. W., and Balch, M., "Point-Collocation Nonintrusive Polynomial Chaos Method for Stochastic Computational Fluid Dynamics," *AIAA Journal*, Vol. 48, No. 12, 2010, pp. 2721–2730.

[12] Walters, R. W. and Huyse, L., "Uncertainty Analysis for Fluid Mechanics with Applications," Tech. rep., ICASE 2002-1, NASA/CR-2002-211449, NASA Langley Research Center, Hampton, VA, 2002.

[13] Eldred, M. S., "Recent Advances in Non-Intrusive Polynomial Chaos and Stochastic Collocation Methods for Uncertainty Analysis and Design, AIAA 2009-2274," 50^{th} *AIAA/ASME/ASCE/AHS/ASC Structures*, Palm Springs, CA, May 2009.

[14] West IV, T. K., Hosder, S., and Johnston, C. O., "A Multi-Step Uncertainty Quantification Approach Applied to Hypersonic Reentry Flows, AIAA 2011-2524," 51^{st} *AIAA Aerospace Sciences Meeting*, Grapevine, TX, Jan. 2013.

[15] West IV, T. K., Hosder, S., and Johnston, C. O., "Uncertainty Quantification of Hypersonic Reentry Flows using Sparse Sample and Stochastic Expansions," *16th AIAA Non-Deterministic Approaches Conference*, National Harbor, MD, Jan. 2014.

[16] Brune, A. J., West, T., Hosder, S., and Edquist, K. T., "Uncertainty Analysis of Mars Entry Flows over Hypersonic Inflatable Aerodynamic Decelerators," *AIAA Journal of Spacecraft and Rockets*, Vol. 52, No. 3, 2015, pp. 776–788.

[17] Brune, A. J., Hosder, S., and Edquist, K. T., "Uncertainty Analysis of Fluid-Structure Interaction of a Deformable Hypersonic Inflatable Aerodynamic Decelerator, AIAA 2015-3581," *20th AIAA International Space Planes and Hypersonic Systems and Technologies Conference, International Space Planes and Hypersonic Systems and Technologies Conferences*, Glasgow, Scotland, 2015.

[18] Witteveen, J. A. S. and Bijl, H., "Efficient Quantification of the Effect of Uncertainties in AdvectionâĂŞDiffusion Problems Using Polynomial Chaos," *Numerical Heat Transfer*, Vol. 53, No. 5, 2008, pp. 437–465.

[19] Han, D. and Hosder, S., "Inherent and Model-Form Uncertainty Analysis for CFD Simulation of Synthetic Jet Actuators, AIAA 2012-0082," 48^{th} *AIAA Aerospace Sciences Meeting*, Nashville, TN, Jan. 2012.

[20] Asif, M. S. and Romberg, J., "Fast and Accurate Algorithms for Re-Weighted l1-Norm Minimization," *IEEE Transactions on Signal Processing*, Vol. 61, No. 23, 2013, pp. 4905–4916.

[21] Doostan, A. and Owhadi, H., "A non-adapted sparse approximation of PDEs with stochastic inputs," *Journal of Computational Physics*, Vol. 230, No. 8, 2011, pp. 3015–3034.

[22] Yang, A., Ganesh, A., Sastry, S., and Ma, Y., "Fast L1-Minimization Algorithms and An Application in Robust Face Recognition: A Review," Tech. rep., Tech. Rep. UCB/EECS-2010-13, Feb. 2010.

[23] Sudret, B., "Global sensitivity analysis using polynomial chaos expansion," *Reliability Engineering and System Safety*, Vol. 93, No. 7, 2008, pp. 964–979.

[24] Crestaux, T., Maitre, O. L., and Martinez, J.-M., "Polynomial chaos expansion for sensitivity analysis," *Reliability Engineering and System Safety*, 2009.

[25] Inc., C., "COMSOL Multiphysics User's Guide, v5.0," Tech. rep., COMSOL/CM-010004, Oct. 2014.

[26] Sullivan, R. M., B. E. H. and Dec, J. A., "Analysis Methods for Heat Transfer in Flexible Thermal Protection Systems for Hypersonic Inflatable Aerodynamic Decelerators," Tech. rep., NASA/TM-2014-218311, April 2014.

[27] Mazaheri, A., Gnoffo, P. A., Johnston, C. O., and Kleb, B., "LAURA Users Manual: 5.5-65135," Tech. rep., NASA/TM-2011-217800, Feb. 2012.

[28] Smith, A. M. and Cebeci, T., "Numerical solution of the turbulent boundary layer equations," Tech. rep., Tech. Rep. Douglas Aircraft Division DAC-33735, 1967.

[29] Yee, H., Sandham, N., and Djomehri, M., "Low Dissipative High Order Shock-Capturing Methods Using Characteristic-Based Filters," *Journal of Computational Physics*, Vol. 150, No. 1, 1999, pp. 199–238.

[30] Swanson, G., Cassell, A. M., Johnson, R. K., Hughes, S. J., Calomino, A. M., and Cheatwood, F. M., "Structural Strap Tension Measurements of a 6-meter Hypersonic Inflatable Aerodynamic Secelerator under Static and Dynamic Loading, AIAA 2013-1287," *22nd AIAA Aerodynamic Decelerator Systems Technology Conference*, Daytona Beach, FL, March 2013.

[31] Cassell, A. M., Swanson, G. T., Quach, B. T., Kushner, L. K., et al., "Design and Execution of the Hypersonic Inflatable Aerodynamic Decelerator Large-Article Wind Tunnel Experiment, AIAA 2013-1304," *AIAA Aerodynamic Decelerator Systems Conference*, Daytona Beach, FL, March 2013.

[32] Sutton, K. and Graves, R. A., "A General Stagnation-Point Convective-Heating Equation for Arbitrary Gas Mixtures," Tech. rep., NASA/TR R-376, 1971.

[33] Dec, J. A. and Braun, R. D., "An Approximate Ablative Thermal Protection System Sizing Tool for Entry System Design," *AIAA Aerospace Sciences Conference*, Reno, NV, Jan. 2006.

[34] Rossman, G. A. and Braun, R. D., "Thermogravimetric Analysis of Flexible Thermal Protection Systems for Thermal Response Modeling, AIAA 2016-1513," *54th AIAA Aerospace Sciences Meeting*, San Diego, CA, Jan. 2016.

[35] Wright, M. J., Hwang, H. H., and Schwenke, D. W., "Recommended Collision Integrals for Transport Property Computations Part II: Mars and Venus Entries," *AIAA Journal*, Vol. 45, No. 1, 2007, pp. 281–288.

[36] Bettis, B. and Hosder, S., "Uncertainty Quantification in Hypersonic Reentry Flows Due to Aleatory and Epistemic Uncertainties, AIAA 2011-252," *49th AIAA Aerospace Sciences Meeting including New Horizons Forum and Aerospace Exposition*, Orlando, FL, Jan. 2011.

[37] Bose, D. and Wright, M., "Uncertainty Analysis of Laminar Aeroheating Predictions for Mars Entries," *AIAA/AAS Astrodynamics Specialist Conference*, Toronto, Ontario Canada, Aug. 2010.

[38] Gupta, R. N., Yos, J. M., Thompson, R. A., and Lee, K. P., "A Review of Reaction Rates and Thermodynamic and Transport Properties for an 11-Species Air Model for Chemical and Thermal Nonequilibrium Calculations to 30000 K," Tech. rep., NASA/RP-1232, Aug. 1990.

[39] Wright, M., Tang, C. Y., Edquist, K. T., Hollis, B. R., Krasa, P., and Campbell, C. A., "A Review of Aerothermal Modeling for Mars Entry Missions, AIAA 2010-0443," 48^{th} *AIAA Aerospace Sciences Meeting*, Orlando, FL, Jan. 2010.

[40] Johnston, C. O., Brandis, A. M., , and Sutton, K., "Shock Layer Radiation Modeling and Uncertainty for Mars Entry, AIAA 2012-2866," 43^{rd} *AIAA Thermophysics Conference*, New Orleans, LA, June 2012.

SECTION

2. CONCLUSIONS AND FUTURE WORK

2.1. CONCLUSIONS

The uncertainty in the hypersonic flowfield, fluid-structure interaction, and flexible thermal protection system was investigated with an efficient stochastic expansion uncertainty quantification approach. The presented analysis was applied to the Hypersonic Inflatable Aerodynamic Decelerator vehicle for a given Mars entry trajectory. Based on a series of global nonlinear sensitivity analyses, the important uncertain variables were identified, which significantly contributed to the output performance metric uncertainties of interest. These important variables can be used for further inverse parameter estimation analyses when comparing to experimental test data. The uncertainty in the performance metrics of interest were quantified, which can be used for the reliability and robustness assessments of the HIAD design.

The uncertainty was first investigated for the high-fidelity numerical modeling of hypersonic flow over a HIAD during Mars entry for both fully laminar and fully turbulent flows. In particular, a fixed aeroshell of HIAD scale was considered for quantification of uncertainty in the shock-layer flowfield at peak stagnation-point heating conditions of a ballistic Mars entry trajectory. Uncertainty results were presented for convective heating, radiative heating, and shear stress distributions on the HIAD surface, which were subject to a large number of epistemic and aleatory uncertainties in freestream conditions (i.e., velocity density, and temperature) and physical modeling parameters associated with flowfield

chemistry, binary collision interactions, and radiative heat transfer. Only a small fraction of the 65 uncertain parameters revealed significant contribution to the uncertainty in the aerodynamic heating and shear stresses at the wall. Boundary layer type (laminar and turbulent) affected only the convective heating and shear stresses, as the radiative heating and wall pressures showed remarkable similarities for both boundary layer flows. For the convective heat flux uncertainty, the CO_2-CO_2, CO_2-O, and CO-O interactions were significant contributors for both laminar and turbulent flows. The freestream quantities (density and velocity) were also significant for both boundary layer flows. The Reynolds number variation affected the turbulent heating augmentation in the flank region, which explains the high dependence of convective heating on the freestream density and velocity. The non-Boltzmann rate involving the radiating states of the CO 4th Positive band was the main contributor to the radiative flux at the nose and flank regions. The reactions that involved production of the CO also consistently showed significant contributions to the uncertainty of the radiative flux for both boundary layer flows. These observations are primarily due to the strong emission of the CO 4th Positive molecular band system in the nonequilibrium region of the shock layer. For the shear stress uncertainties, the CO_2-CO_2, freestream density, and freestream velocity were shown to be important for both boundary layer flows with significant importance of the freestream density for turbulent boundary layers.

The uncertainty was then investigated for the deflection and the resulting surface conditions of a deformable Hypersonic Inflatable Aerodynamic Decelerator configuration due to freestream variations and uncertainties in structural and flowfield physical modeling parameters. The decelerator was defined to be a stack of eight tori that form a 60-deg half angle cone with innermost torus attached to a rigid nose cap. A high-fidelity, loosely-coupled approach was presented for static fluid-structure interaction simulations using the FUN3D flow solver and the NASTRAN structural solver. A sparse approximation approach

for nonintrusive polynomial chaos was applied to quantify the uncertainty of the inflatable decelerator deformation and surface conditions in the presence of the aforementioned uncertain parameters at peak heating conditions for a reference lifting Mars entry trajectory. Results were compared to those obtained in a previous study for ballistic Mars entry. Uncertainty analysis showed that the deflection angle can vary by as much as 2.2 degrees with a 95% confidence interval of [4.74, 6.94] deg. on the windward side of the pitch plane and approximately 1 deg. 95% confidence interval of [0.34, 1.25] deg. on the leeward side of the pitch plane. For both lifting and ballistic entry trajectories, the tensile stiffness of the axial cords was the top contributor to the deflection uncertainty for the entire deformable surface. The inflation pressure and torus tensile stiffnesses were important near the nose cap juncture while the 4000-lb radial strap tensile stiffnesses were significant throughout the deformable region (both leeward and windward), especially towards the shoulder torus. For lifting Mars entry at peak heating, the torsional stiffness of the torus was shown to be significant because of the asymmetric loading experienced externally by the inflatable decelerator.

The deflection uncertainty was applied to the uncertainty analysis of the resulting surface conditions (i.e., surface pressure, shear stress, and heat flux). For both lifting and ballistic Mars entry, uncertainty analysis showed that the pressure, shear stress, and heat flux vary significantly in the deformable region under the uncertainty sources considered. Slight importance of the deflection uncertainty was observed for the shear stress uncertainties with increased significance for the surface pressure and heat flux uncertainty (as much as 5%) on the windward side of the pitch plane. On the leeward side, the effect of deflection uncertainty is reduced to less than 1% due to small deflections in this region. The freestream density was the top contributor for surface pressure, shear stress, and heat flux for the entire deformable region. The CO_2-CO_2 binary collision interaction was also

significant contributor to the shear stress and heat flux uncertainty due to its influence in the transport properties of the flow near the surface. Deflection uncertainty was determined to be an insignificant contributor to the surface condition uncertainty, relative to the flowfield uncertainty sources (frestream density and velocity, binary collision interactions).

After identifying the significant uncertainty sources for both hypersonic flow and FSI analyses, the uncertainty in the F-TPS in-depth thermal response, specifically the bondline temperature near the gas barrier layer, was investigated for a ballistic Mars entry trajectory. The HIAD forebody considered has a 60-deg sphere-cone shape with a 10 meter major diameter. A sparse stochastic expansion approach was used to conduct a global senstivity analysis for dimension reduction of the uncertain parameters. The reduced dimension of uncertain parameters were included in the uncertainty analysis of the flexible TPS thermal response with a point-collocation stochastic expansion approach. The high-fidelity baseline model was presented with discussion on the LAURA flow solver and the COMSOL multi-physics code for TPS thermal modeling of porous materials subject to convective heat transfer and pressure loads. A reference nominal trajectory was also presented based on the Exploration Feed Forward study with 5.8 km/s direct entry with selected trajectory points for analysis with the LAURA flow solver, which is used for external convective heating parameters and surface pressure input to the COMSOL solver. The baseline solution showed that the critical surface point for maximum bondline temperature occurred in the flank region with fully turbulent flow assumption. At this surface point, response surfaces were constructed for the convective heating parameters and surface pressure to replace the CFD model at each trajectory point. This approach reduced the number of high-fidelity CFD evaluations required in the creation of a stochastic response surface by considering only four flow field uncertain variables (freestream velocity, freestream density, and CO_2-CO_2/CO_2-O binary interactions). These stochastic response surfaces for the convective

heating parameters and surface pressures at each trajectory point were used as input for F-TPS response analysis.

A global nonlinear sensitivity analysis was performed and showed that eight of the 22 uncertain parameters contributed to 95% of the bondline temperature uncertainty. An uncertainty analysis of the bondline temperature was performed with the reduced dimension of eight uncertain parameters, which included the freestream density, thermal conductivities of the insulator and outer fabric layers, and thickness and initial density of the insulator layer 2 near the gas barrier layer. Uncertainty analysis showed that the bondline temperature varies by as much as 125% above the nominal prediction, and the upper bound of the uncertainty band exceeds the limit state of the bondline temperature at 65 seconds, prior to HIAD separation at 70 seconds. As a result, additional work is planned to determine the thickness requirement, and hence thickness margin, of the flexible TPS to ensure the upper bound of the uncertainty band does not exceed the 400 ^{o}C limit of the bondline temperature in the presence of uncertainty sources considered for the hypersonic flowfield and the flexible TPS thermal model.

2.2. FUTURE WORK

Although significant work has been achieved for application of an efficient uncertainty quantification approach to the HIAD analysis and design, there are certain areas of interest for future work. Some of these areas are relative to key components that have not been covered in the current study.

First, the radiative heat flux due to shock-layer radiation should be explored for the fluid-structure interaction and flexible thermal protection system analyses. The current study explored this aspect for only the hypersonic flowfield analysis. It was determined that at lower velocities with a decreased direct entry velocity for the trajectory, the radiation

due to the shocklayer would be insignificant with reduced production of the CO molecules. However, subject matter experts recently have expressed the concern for significant emissions from the CO_2 ultraviolet band at lower velocities. The author recommends that an investigation be done with the HIAD geometry at velocities lower than 6 km/sec. Because the geometry has a small nose-to-base diameter ratio, the shock distance from the surface may suggest that there is a small enough optical path for emissions to produce insignificant radiative heat flux compared to the convective heat flux.

Second, the flexible thermal protection system uncertainty analysis can be integrated to a thickness margin study for updating the design of the thermal protection system. In the current study, the uncertainty results showed that the upper bound of the bondline temperature uncertainty exceeded the 400^oC temperature limit. The thickness requirements and margin can be updated for the insulator layers to improve the thermal protection system design to meet reliability standards.

Finally, the significant uncertainty sources can be investigated further with more ground testing, flight experiments, and theoretical approaches to improve the state of knowledge in these parameters (i.e. regarding the atmospheric model, material thermal properties of the thermal protection system, and the binary collision interaction processes for estimating the transport properties of the hypersonic flowfield). With additional knowledge gained, this approach can effectively decrease the uncertainty in the prediction of surface heat flux and pressure, and hence, the bondline temperature of the thermal protection system. Reduction of these uncertainties may, in turn, improve the reliability of the thermal protection system.

BIBLIOGRAPHY

[1] Zang, T. A., Dwyer-Ciancolo, A. M., Kinney, D. J., R.Howard, A., Chen, G. T., Ivanov, M. C., Sostaric, R. R., and Westhelle, M. C., "Overview of the NASA Entry,Descent, and Landing Systems Analysis Studies for Large Robotic-class Missions, AIAA 2010-8649," AIAA SPACE 2010 Conference and Exhibition, Anaheim, CA, Aug. 2010.

[2] Dwyer-Ciancolo, A. M., Davis, J. L., Shidner, J. D., and Powell, R. W., "Entry, Descent, and Landing Systems Analysis: Exploration Class Simulation Overview and Results," AIAA/AAS Astrodynamics Specialist Conference, Toronto, Ontario Canada, Aug. 2010.

[3] Dwyer-Ciancolo, A. M., Davis, J. L., Engelund, W. C., Komar, D. R., Queen, E. M., Samareh, J. A., Way, D. W., and Zang, T. A., "Entry, Descent, and Landing Systems Analysis Study: Phase 2 Report on Exploration Feed-Forward Systems," Tech. rep., NASA/TM-217055, Feb. 2011.

[4] Bose D. M., Shidner, J., Winski, R., Zumwalt, C., Cheatwood, F. M., and Hughes, S. J., "The Hypersonic Inflatable Aerodynamic Decelerator (HIAD) Mission Applications Study, AIAA 2013-1389", AIAA Aerodynamic Decelerator Systems (ADS) Conference, Daytona Beach, FL, March 2013.

[5] Hollis, B. R. and Prabhu, D. K., "Assessment of Laminar, Convective Aeroheating Prediction Uncertainties for Mars Entry Vehicles," AIAA Journal of Spacecraft and Rockets, Vol. 50, No. 1, 2013, pp. 56âĂŞ68.

[6] Johnson, C. O., Hollis, B. R., and Sutton, K., "Shock Layer Radiation Modeling and Uncertainty for Mars Entry," 43rd AIAA Thermophysics Conference, New Orleans, LA, 2012.

[7] Bose, D. and Wright, M., "Uncertainty Analysis of Laminar Aeroheating Predictions for Mars Entries," AIAA/AAS Astrodynamics Specialist Conference, Toronto, Ontario Canada, Aug. 2010.

[8] West IV, T. K., Hosder, S., and Johnston, C. O., "A Multi-Step Uncertainty Quantification Approach Applied to Hypersonic Reentry Flows, AIAA 2011-2524," 51st AIAA Aerospace Sciences Meeting, Grapevine, TX, Jan. 2013.

[9] West IV, T. K., Hosder, S., and Johnston, C. O., "Uncertainty Quantification of Hypersonic Reentry Flows using Sparse Sample and Stochastic Expansions," 16th AIAA Non-Deterministic Approaches Conference, National Harbor, MD, Jan. 2014.

[10] Tanner, C. L., "Aeroeleastic Analysis and Testing of Supersonic Inflatable Aerodynamic Decelerators," Ph.D. Dissertation, Georgia Inst. of Technology, Atlanta, GA, May 2012.

[11] Swanson, G., Cassell, A. M., Johnson, R. K., Hughes, S. J., Calomino, A. M., and Cheatwood, F. M., "Structural Strap Tension Measurements of a 6-Meter Hypersonic Inflatable Aerodynamic Decelerator Under Static and Dynamic Loading," AIAA Paper 2013-1287, March 2013.

[12] Cassell, A. M., Swanson, G. T., Quach, B. T., Kushner, L. K., Brown, J. D., Kazemba, C.D., Kruger, C. E., Li, L., Johnson, R. K., Hughes, S. J., Calomino, A. M., and Cheatwood, F. M., "Design and Execution of the Hypersonic Inflatable Aerodynamic Decelerator Large-Article Wind Tunnel Experiment," AIAA Aerodynamic Decelerator Systems Conference, AIAA Paper 2013-1304, March 2013.

[13] Hughes, S. J., Cheatwood, F. M., Dillman, R. A., Wright, H. S., Del Corso, J. A., and Calomino, A. M., "Hypersonic Inflatable Aerodynamic Decelerator Technology Development Overview," AIAA Aerodynamic Decelerator Systems Conference and Seminar, AIAA Paper 2011-2524, May 2011.

[14] Bruce, W. E., III, Mesick, N. J., Ferlemann, P. G., Siemens, P. M., III, Del Corso, J. A., Hughes, S. J., Tobin, S. A., and Kardell, M. P., "Aerothermal Ground Testing of Flexible Thermal Protection Systems for Hypersonic Inflatable Aerodynamic Decelerators," 9th International Planetary Probe Workshop, Toulouse, France, June 2012.

[15] Del Corso, J. A., Bruce, W. E., III, Hughes, S. J., Dec, J. A., Rezin, M. D., Meador, M. B., Hiaquan, G., Fletcher, D. G., Calomino, A. M., and Cheatwood, F. M., "Flexible Thermal Protection System Development for Hypersonic Inflatable Aerodynamic Decelerators," 9th International Planetary Probe Workshop, Toulouse, France, June 2012.

[16] Del Corso, J. A., Cheatwood, F. M.,Bruce, W. E., III, Hughes, S. J. and Calomino, A. M., "Advanced High-Temperature Flexible TPS for Inflatable Aerodynamic Decelerators," 21st AIAA Aerodynamic Decelerator Systems Technology Conference and Seminar, AIAA Paper 2011-2510, May 2011.

[17] Tobin, S. A. and Dec, J. A., "A Probabilistic Sizing Demonstration of a Flexible Thermal Protection System for a Hypersonic Inflatable Aerodynamic Decelerator, AIAA 2015-1895," AIAA SciTech Conference, Kissimmee, FL, Jan. 2015.

VITA

Andrew J. Brune was born in Saint Charles, Missouri. After graduating from Saint Charles High School in Saint Charles, Missouri in 2007, he began his undergraduate education at the Missouri University of Science and Technology, formerly known as University of Missouri - Rolla. Over the course of his undergraduate career, he was actively involved in Sigma Gamma Tau Engineering Society and the Blue Key Honor Society and began his research career in September 2010, funded by the NASA-Missouri Space Grant Program to perform a cross-cutting study on hypersonic cruise vehicles in conceptual design. In 2011, Andrew graduated with Summa Cum Laude honors, earning a Bachelor of Science degree in Aerospace Engineering with an undergraduate minor in Applied Mathematics. He continued his education earning a Master of Science degree in Aerospace Engineering from the Missouri University of Science and Technology in May 2013 and performed his thesis research work on investigating efficient transpiration cooling strategies for a representative leading edge of a hypersonic cruise vehicle. Before beginning his PhD career in August of 2013, he was selected as a NASA Langley Aerospace Research Space Scholars (LARSS) Program intern at Langley Research Center in Hampton, Virginia in the summers of 2012 and 2013. In the meantime, he received a NASA Space Technology Research Fellowship award to fund his proposed research in uncertainty quantification applied to the analysis and design of a recently developed technology for future Mars entry missions, called a Hypersonic Inflatable Aerodynamic Decelerator. In December 2016, he earned a Doctor of Philosophy degree in Aerospace Engineering from MIssouri University of Science and Technology. Andrew is now employed by NASA at Langley Research Center in Hampton, Virginia as an Aerospace Technologist in Heat Transfer.